3-23-2018

Near Earth Space Object Detection Utilizing Parallax as Multi-hypothesis Test Criterion

Joseph C. Tompkins

NEAR EARTH SPACE OBJECT DETECTION UTILIZING PARALLAX AS MULTI-HYPOTHESIS TEST CRITERION

Creating a ground-based space-object-detection system using parallax as a multi-hypothesis test criterion will bridge significant gaps in the current Space Situational Awareness of the Air Force better enabling space operations and the warfighter.

Joseph C. Tompkins, Captain, USAF

AFIT-ENG-MS-18-M-064

DEPARTMENT OF THE AIR FORCE
AIR UNIVERSITY

AIR FORCE INSTITUTE OF TECHNOLOGY

Wright-Patterson Air Force Base, Ohio

AFIT-ENG-MS-18-M-064

NEAR EARTH SPACE OBJECT DETECTION UTILIZING PARALLAX AS MULTI-HYPOTHESIS TEST CRITERION

THESIS

Presented to the Faculty

Department of Electrical and Computer Engineering

Graduate School of Engineering and Management

Air Force Institute of Technology

Air University

Air Education and Training Command

In Partial Fulfillment of the Requirements for the

Degree of Master of Science in Electrical Engineering

Joseph C. Tompkins, BS

Captain, USAF

March 2018

AFIT-ENG-MS-18-M-064

NEAR EARTH SPACE OBJECT DETECTION UTILIZING PARALLAX AS MULTI-HYPOTHESIS TEST CRITERION

Joseph C. Tompkins, BS
Capt., USAF

Committee Membership:

Dr. Stephen C. Cain
Chair

Maj. Kevin P. Vitayaudom
Member

Dr. Henry Chen
Member

Abstract

The US Strategic Command (USSTRATCOM) operated Space Surveillance Network (SSN) is tasked with Space Situational Awareness (SSA) for the US military. This system is made up of Electro-Optic sensors such as the Space Surveillance Telescope (SST) and Ground-based Electro-Optical Deep Space Surveillance (GEODSS) as well as RADAR based sensors such as the Space Fence. While Lockheed Martin's Space Fence is very adept at detecting & tracking objects in Low Earth Orbit (LEO) below 3000 Km in height [1], gaps remain in the tracking of Resident Space Objects (RSO's) in Geosynchronous Orbits (GEO) due to limitations associated with the implementation of the SST and GEODSS systems.

This thesis explores a reliable, ground-based technique to quickly determine the altitude of a RSO from a single or limited set of observations; implementation of such sensors into the SSN would mitigate GEO SSA performance gaps. The research entails a method to distinguish between the point spread function (PSF) observed by a star and the PSF observed from an RSO using Multi-Hypothesis Testing with parallax as a test criterion. Parallax is the effect that an observed object will appear to shift when viewed from different positions. This effect is explored by generating PSFs from telescope observations of space objects at different baselines. The research has shown the PSF of an RSO can be distinguished from that of a star using single, simultaneous observations from reference and parallax sensing telescopes. This thesis validates these techniques with both simulations and with experimental data from the SST and Naval Observatory sensors.

Acknowledgments

Some special thanks are due to Dr. Steven Cain for all the exemplary mentorship during the creation of this project. Without his guidance and instruction, the implementation of the simulation would have been significantly more difficult. His lectures and projects on MATLAB implementation were also pivotal in the understanding by the author of these topics.

Joseph C. Tompkins

Table of Contents

List of Figures

List of Tables

List of Acronyms

SSN Space Surveillance Network iv

Refers to space surveillance sensors used by the USAF for SSA

SSA Space Situational Awareness iv

"SSA encompasses intelligence on adversary space operations; surveillance of all space objects and activities; detailed reconnaissance of specific space assets; monitoring space environmental conditions; monitoring cooperative space assets; and conducting integrated command, control, communications, processing, analysis, dissemination, and archiving activities" [2]

SST Space Surveillance Telescope iv

Electro-optic sensor used for SSA purposes by the USAF as a part of the USAF SSN

LEO Low Earth Orbit iv

Region of space below 2,000 km

RSO Resident Space Object iv

Natural or artificial object near the Earth

GEO Geosynchronous Earth Orbit iv

The region of space at 5,678 km

CDO Contested, Degraded and Operationally Limited 1

C3 Command, Control and Communications 1

DOD Department of Defense 1

GAO Government Accountability Office 1

SBSS Space Based Surveillance System 1

MEO Medium Earth Orbit 1

Used to find the probability that a RV will fall within a given range of values

PSD Power Spectral Density.....21

Frequency response of a random signal

PD Point Detector 35

Compares an observed pixel signal strength to a threshold

LRT Likelihood Ratio Test 35

Ratio formed by dividing the PD or CD output under the different positive Hypotheses by the null Hypothesis

SNR Signal to Noise Ratio 38

Compares the signal strength from an object to that of the background

CD Correlator Detector 39

C*orrelates observed data with an expected Hypothesis and then compares the output to a threshold*

MHT Multi-Hypothesis Test 43

Compares LRT outputs under certain Hypotheses to determine which has more likely occurred

CLT Central Limit Theorem 57

States that adding independent RV's results in a Gaussian distribution

ROC Receiver Operating Characteristics.....61

Curve created by plotting the true positive detection probability against the false positive detection probability

RV Random Variable 82

Variable with possible values occurring randomly

List of Symbols

NEAR EARTH SPACE OBJECT DETECTION UTILIZING PARALLAX AS MULTI-HYPOTHESIS TEST CRITERION

I. Introduction

SSA is paramount in any military operation because the warfighter's success is hinged on the space environment being a sanctuary; such is the serious weakness of the US military's current stratagem. The official USAF description of the SSA mission is that "SSA encompasses intelligence on adversary space operations; surveillance of all space objects and activities; detailed reconnaissance of specific space assets; monitoring space environmental conditions; monitoring cooperative space assets; and conducting integrated command, control, communications, processing, analysis, dissemination, and archiving activities" [2]. In reality, the space operational environment of the future will be contested, degraded and operationally limited (CDO) which necessitates that the US maintain a comprehensive situational awareness of it at all times [3]. These challenges necessitate the evolution of SSA techniques to ensure that there are no gaps in the SSN allowing un-predicted collisions or exploitation by adversaries. Protecting our nation's space-based reconnaissance and command, control and communication (C3) assets is paramount for our ability to project power to the warfighter.

Indeed, the US Department of Defense (DOD) is pursuing an aggressive modernization effort of its SSA assets. The Air Force's FY 2017 Research, Development, Test & Evaluation Budget (FY17 RTD&E) shows an allotment of $1.47 billion for SSA efforts thru FY 2021 [2] and the Government Accountability Office (GAO) indicates that the DOD is planning to spend upwards of $6 Billion dollars on SSA efforts thru 2020 [4]. Current efforts to bolster the SSN include the $1.56 billion Space Fence which is under

construction at the Kwajalein Atoll in the Marshall Islands and the classified budget Geosynchronous Space Situational Awareness Program (GSSAP), as part of the Space Based Surveillance System (SBSS), which has 4 operational satellites monitoring the geosynchronous orbit altitude (GEO). The Space Fence will not be able to track objects beyond Low Earth Orbit (LEO) and will only have limited Medium Earth Orbit (MEO) surveillance abilities. It can be assumed that GSSAP has exceptional GEO object tracking and surveillance abilities, but DOT&E reports suggest that it may have shortfalls in the areas of survivability, reliability and ground control [5]. The USAF is also modernizing the Joint Space Operations Center (JSpOC) by investing $1 billion in a program known as the JSpOC Mission System (JMS) so that data from the SSN sensors can be collected, combined and analyzed at one central location to provide for command and control (C2) decisions in the space domain [6]. The effort is vital for the modernization of space surveillance; according to Gen. Hyten, commander USTRATCOM, the JSpOC Mission System "is the key to everything—the key to the kingdom" and it is "the key to the future where [the Air Force] is going" [7]. Gen. Goldfein, U.S. Air Force Chief of Staff, states "space is the ultimate high ground… space superiority is not an American birth right, it is something we will fight for" [8]. SSA is the critical link in the chain of space superiority.

Another realm which needs to be explored to strengthen U.S. SSA capabilities is the realm of sensor fusion. Currently, individual sensors search for NEO's and report any uncorrelated targets (UCT) state vectors to the JSPOC JMS which then keeps track of those objects in its space catalogue. At the AFA Space and Cyberspace Symposium, Gen. Goldfein said that much of his current efforts are preparing the AF to be effective for a FY2030 conflict; he emphasized that current capabilities are the ones established by

predecessors and that the 24th AF Chief of Staff will "go to war with the force that we build today… [t]he future of warfare in the age of cognition is going to be about network and data—does it connect? Good. Can it share? Even better" [8]. He mentioned either connected systems or systems which share data over twenty times in his one-hour long speech and challenged all AF leaders to find ways to make the marbles connect and share. The argument is compelling and it is logical that a system of sensors should operate more effectively as part of a network rather than isolated data collection nodes. Novel ways to leverage the capabilities of a network of ground based electro-optic sensors needs to be explored; a network approach to NEO detection which leverages shared, simultaneous observations would enable a more robust method than just utilizing single sensors independently. Could the AF's SSN be made more perceptive and robust than the sum of its parts if those parts were combined into a network or if the data were shared to create more meaningful datasets? Data from sensors at different geographic locations contains unique information about an observation; can the sensors share their data for a more perceptive detection scheme?

Motivation for Research

Although the DOD has clearly recognized the importance of SSA and is investing accordingly, certain paradigms are prevalent among academia and industry for the characterization of RSO's. SST and GEODS, which are operated by MIT Lincoln Laboratories, are the primary ground-based electro-optic sensors in the SSN and use velocity matched filtering to classify RSO's [9]. This methodology entails monitoring an object over an extended period to see how it's moving to decide whether the object is of

interest. The velocity matched filtering technique would miss objects which are moving with un-hypothesized velocities or orbits. This technique also requires a detection to be registered in five successive frames so that dim objects with wavering brightness could be lost between samples. Objects which aren't bright enough over an extended time could be missed and avenues are opened for adversaries to exploit SSA sensors using maneuverable or dim space assets. If the SSN contained a sensor with the capability to determine a RSO's state vector with single or limited observations, the sensor would produce smaller data sets, detect dimmer objects and close gaps which adversaries could exploit. Even better would be a method to utilize a network of ground based electro-optic sensors and leverage their simultaneous data sets to produce a more perceptive detection scheme for NEO's. Space based assets may be more capable at detecting dimmer objects over extended periods but suffer from cost, reliability and C2 limitations [5]. The need for a cost-effective ground based technique to quickly determine the RSO state vector of an observation from single or limited data sets is apparent. A network of sensors may present itself as the ideal machinery for such a technique.

Research Goals

This paper proposes a method to distinguish between the point spread function (PSF) observed by a star and the PSF observed from an RSO using Multi-Hypothesis Testing with parallax as a test criterion. Parallax is the effect that an object observed stereoscopically will appear different when viewed from different angles; the effect is easily demonstrated by looking at a close by object and observing its apparent change in position when closing one eye or the other. This effect can be explored by generating PSFs

from telescope observations of objects using two telescopes separated by some baseline distance. The parallax effect will primarily manifest itself in tilt aberrations which will cause the PSF to appear in a different location on the CCD of the parallax sensing telescope.

The goal of this research is to validate the use of a system of parabolic telescopes to detect parallax using Fourier Optics and Statistical Optics. Using Fourier Optics, a technique for finding parallax will be explored with a telescope system consisting of a reference and parallax sensing telescope. Statistical Optics will be utilized to characterize the statistical model of the parabolic mirror telescope system so that the jointly distributed data can be run through Likelihood Ratio Testing (LHT) to come up with a meaningful Multi-Hypothesis Test (MHT) criterion. Based on the statistical model for the PSF of NEOs and stellar objects, multi-hypothesis theory will be utilized to filter observed PSFs into different categories using single or limited synchronous observations from two telescopes. Success of these research goals will be measured by demonstrating the parallax sensing technique using simulated and real data in the presence of various real-world noise sources. Performance metrics will be identified to quantify the performance of this technique in meaningful and straightforward ways.

Thesis Summary

The purpose of this research is to demonstrate that a CD MHT detection algorithm can effectively categorize a detected target as either a stellar or NEO observation. Chapter 2 lays out the foundations for modeling the optical system PSF in the paraxial and non-paraxial case, modeling the atmospheric effects on the optical system for long-exposure observations, modeling the effects of background noise from random photon arrivals and

decomposing the optical system phase into distinct aberrations as represented by Zernike polynomials. Chapter 3 discusses the PD and CD algorithms used for space object detection in currently operational ground based optical sensors and the CD MHT algorithm developed by Zingarelli [10], [11]. Chapter 3 also explains the new concept for detecting a target and categorizing that target as either a stellar or NEO observation in a single data frame using the proposed CD MHT algorithm with optical systems designed to detect parallax and laid out the metrics useful for determining the performance of the new algorithm. In Chapter 4, the optical system with identical telescopes separated by varying baselines is simulated in MATLAB using the concepts in Chapter 2 and the CD MHT algorithm defined in Chapter 3 is tested given the simulated data frames as inputs. Chapter 4 also generates the performance metrics derived in Chapter 3 using a Monte Carlo approach by running thousands of randomly generated data frames through the CD MHT algorithm to produce many LRT realizations; these realizations are used to characterize the statistics of the CD MHT algorithm's performance with different target SNR values. In Chapter 5, a real world optical system with different telescopes is utilized to collect synchronous observations of two targets as the targets are eclipsed by the earth; the experimental setup is analyzed to properly register the PSF's required by the CD MHT algorithm and the experimental data is then run through the CD MHT algorithm to evaluate its performance as compared to the PD algorithm used by SSN ground based sensors today.

II. Fourier Optics Methodology

This chapter lays out the foundations for modeling the optical system PSF in the paraxial and non-paraxial case. The effects of a turbulent atmosphere on the incoming wave-front from a distant space observation are analyzed in the long exposure case. The effects of background noise from random photon arrivals is derived so that it might be accurately modeled in later simulations. Because the effects of parallax on an optical system are easily explained in terms of optical aberrations, decomposing the optical phase into distinct aberrations as represented by Zernike polynomials is also discussed.

Fourier Optics

The propagation of light from a source point, S, to an observation point, P, can be modeled by the 2-D Fourier transform with the proper Fourier kernel provided certain conditions are met. The net field from a source plane is propagated to an observation plane some distance, z, away and the distances between the source points and observation points, R_{12}, are described using Pythagorean's theorem.

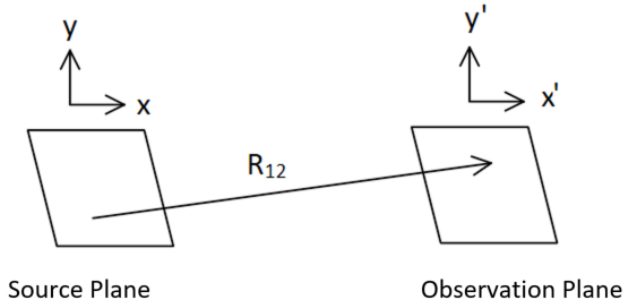

Figure 1: Visual Depiction of R_{12}

The phase and amplitude of the field at the observation plane is found exactly by computing and summing up the individual field values at every grid point in the observation plane. Also known as the Rayleigh-Sommerfeld propagation method, this method is far too

cumbersome and necessary simplifications are made using valid approximations. This propagation involves using the exact distances, R_{12}, from each point in the two planes to determine what the field in the observation plane, U_2, is based on the field in the source plane, U_1, and the propagation distances. Other variables in (2.1) include the wavelength of the light, λ, and the distance between the two planes, z.

$$U_2(x',y') = \frac{z}{j\lambda}\int_{-\infty}^{\infty}\int_{-\infty}^{\infty}\frac{U_1(x,y)e^{\frac{j2\pi R_{12}}{\lambda}}}{{R_{12}}^2}dxdy \tag{2.1}$$

where,

$$R_{12} = \sqrt{z^2 + (x'-x)^2 + (y'-y)^2} \tag{2.2}$$

Using the binomial-expansion on R_{12} as shown in Equation (2.3) and substituting it into the former equation, the Fresnel approximation is obtained in Equation (2.4).

$$R_{12} = 1 + \frac{(x'-x)^2 + (y'-y)^2}{2z^2}) \tag{2.3}$$

$$U_2(x',y') = \frac{e^{j2\pi z/\lambda}e^{\frac{j\pi(x'^2+y'^2)}{\lambda z}}}{j\lambda z}\int_{-\infty}^{\infty}\int_{-\infty}^{\infty}U_1(x,y)e^{\frac{j\pi(x^2+y^2)}{\lambda z}}e^{-j2\pi\frac{(x'\cdot x+y'\cdot y)}{\lambda z}}dxdy \tag{2.4}$$

valid given the following condition on z,

$$z \gg \sqrt[3]{\frac{\pi}{4\lambda}\left[(x'-x)_{\max}{}^2 + (y'-y)_{\max}{}^2\right]^2} \tag{2.5}$$

The Fraunhofer approximation is obtained by making the approximation that the propagation distance is much greater than the other terms in the quadratic phase factor causing the Fresnel term to vanish.

$$z \gg \frac{\pi(x^2{}_{\max} + y^2{}_{\max})}{\lambda} \tag{2.6}$$

$$U_2(x',y') = \frac{e^{j2\pi z/\lambda} e^{\frac{j\pi(x'^2+y'^2)}{\lambda z}}}{j\lambda z} \int_{-\infty}^{\infty}\int_{-\infty}^{\infty} U_1(x,y) e^{-j2\pi(F_x x + F_y y)} dxdy \tag{2.7}$$

where,

$$F_x = \frac{x'}{\lambda z} \text{ and } F_y = \frac{y'}{\lambda z} \tag{2.8}$$

Equation (2.7) is the Fourier transform of the aperture evaluated at the optical frequencies F_x and F_y [12]. The above expressions show the necessary conditions to make either the Fresnel or Fraunhofer approximations and how the propagation of light is modeled adequately by the 2-D Fourier transform. The aperture function can also be introduced into the equation if the source field is being propagated from the plane of an aperture such as a mirror or lens. The extent of the electromagnetic field is confined to the aperture, so the aperture function is defined as ones everywhere where the aperture exists and as zeroes everywhere where the aperture doesn't exist. An example aperture function which contains the obscuration of a reflecting mirror is seen in Figure 2.

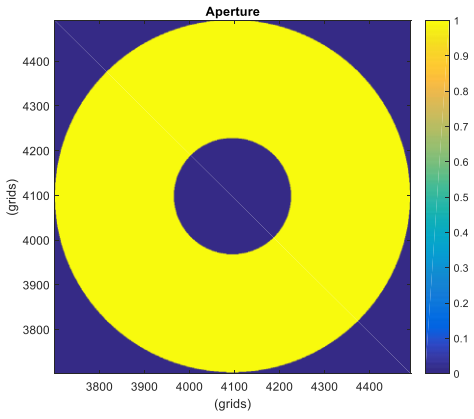

Figure 2: Aperture Function of Parabolic Mirror Telescope

The Fresnel approximation will reduce to a 2-D Fourier Transform when propagating an optical field from the plane of an optical device such as a lens or mirror to the lens or mirror's focal point which is often the setup for close distances such as the distance between a focusing optic and a CCD array. A phase delay term, $\theta(x, y)$, seen in Equation (2.9) is added to the propagating field which perfectly cancels out the Fresnel term at the focal point. Equation (2.10) is the source field on the other side of the optics and U_3 is the field at the focus of the optics as shown in Equations (2.11).

$$\theta(x, y) = -\pi \frac{(x^2 + y^2)}{\lambda f} \tag{2.9}$$

$$U_2(x, y) = U_2(x, y) e^{\frac{-j\pi(x^2+y^2)}{\lambda f}} \tag{2.10}$$

$$U_3(x', y') = \frac{e^{j2\pi z/\lambda} e^{\frac{j\pi(x'^2+y'^2)}{\lambda z}}}{j\lambda z} \int_{-\infty}^{\infty}\int_{-\infty}^{\infty} U_2(x, y) \cancel{e^{\frac{-j\pi(x^2+y^2)}{\lambda f}}} \cancel{e^{\frac{j\pi(x^2+y^2)}{\lambda z}}} e^{-j2\pi(F_x x + F_y y)} dxdy \tag{2.11}$$

The human eye or any manufacturable sensor is incapable of sampling the instantaneous value of an oscillating light field at the Nyquist rate due to the extremely high frequencies on the order of 10^{14} Hz; therefore, the time averaged intensity, denoted as *I*, or time averaged value of the magnitude squared of the optical field, denoted as U, is the most insightful metric.

$$I(x', y') = \frac{1}{T}\int_0^T |U(x', y', t)|^2 dt \tag{2.12}$$

The measure of the spread of energy across the detector is represented by the Point Spread Function (PSF). In an optical system, the PSF is the impulse response, denoted as *h*, of the optical system to a point source located a far distance away. The performance of an optical

system is characterized by the distribution of the PSF and the PSF shape is dependent on the aperture geometry. The PSF, *h*, is normalized such that the total energy within it sums up to unity.

$$h(x',y') = \frac{I(x',y')}{\int_{-\infty}^{\infty}\int_{-\infty}^{\infty} I(x',y')dx'dy'} \tag{2.13}$$

$$\int_{-\infty}^{\infty}\int_{-\infty}^{\infty} h(x',y')dx'dy' = 1 \tag{2.14}$$

Normalizing the PSF is accomplished by the operations shown in (2.13) and (2.14), serves as a sort of conservation of energy and guarantees that the total energy observed in a detected image is equal to the total energy from the object being detected that is collected by the telescope. Using the convolution property from linear systems theory, the field from an object at the detector, denoted as O, can be convolved with the impulse response to show the intensity, *i*, which is observed by the optical system at the CCD detector in the coordinate plane denoted by the x' and y' coordinates.

$$i(x',y') = \int_{-\infty}^{\infty}\int_{-\infty}^{\infty} O(q,w)h(q-x',w-y')dqdw \tag{2.15}$$

As seen below, the total energy from the observed object, E, is found summing up all the energy distributed across the observation plane. This also shows that the OTF and PSF are Fourier transform pairs which comes from the underlying assumption that the optical field from the observed source is a plane wave.

$$E = \int_{-\infty}^{\infty}\int_{-\infty}^{\infty} I(x',y')dx'dy' \tag{2.16}$$

Substituting the convolution of the object with the impulse response (2.15) into the equation for the total energy (2.16) obtains the relationship below (2.17).

$$\mathrm{E} = \int_{-\infty}^{\infty}\int_{-\infty}^{\infty}\int_{-\infty}^{\infty}\int_{-\infty}^{\infty} O(q,w)h(q-x',w-y')dqdwdx'dy' \tag{2.17}$$

rearranging the below integrals into the double integral of the object and the double integral of the shifted and flipped impulse response results in the integral of the object multiplied by 1 as seen in Equation (2.18). This result seen in Equation (2.19) implies that all the measured energy contained within the image formed at the observation plane is equivalent to the total amount of energy from the object.

$$\mathrm{E} = \int_{-\infty}^{\infty}\int_{-\infty}^{\infty} O(q,w)dqdw \int_{-\infty}^{\infty}\int_{-\infty}^{\infty} h(z-x',w-y')dx'dy' \tag{2.18}$$

$$\mathrm{E} = \int_{-\infty}^{\infty}\int_{-\infty}^{\infty} O(q,w)dqdw \tag{2.19}$$

The Optical Transfer Function (OTF), H, describes the spatial frequency response of an optical system and is defined as the auto-correlation of the pupil function with itself normalized by the total area of the pupil function squared. It is a unit-less ratio which describes how certain spatial frequencies are passed by the optical system. In this integral, u and v are spatial frequencies and f is the focal length of the pupil, P.

$$H(u,v) = \frac{\int_{-\infty}^{\infty}\int_{-\infty}^{\infty} P(x,y)P^{*}(x-\overline{\lambda}fu, y-\overline{\lambda}fv)dxdy}{\int_{-\infty}^{\infty} \left|P(x,y)\right|^{2} dxdy} \tag{2.20}$$

where,

$$P(x,y) = A(x,y)e^{\phi(x,y)} \tag{2.21}$$

The pupil function is defined by an aperture transmittance function, A, and phase, ϕ, shown above. The physical meaning of auto-correlation of the pupil is shown pictorially in Figure 3. As the Pupil is shifted farther away, the amount of overlap goes to zero explaining why the OTF goes to zero with larger spatial frequencies.

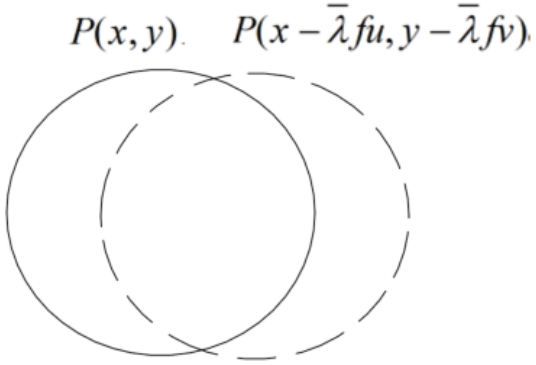

Figure 3: Auto-Correlation of the Pupil Function

One final note is that the OTF and PSF are Fourier transform pairs; the Fourier transform of the PSF is the OTF and the inverse Fourier transform of the OTF is the PSF.

$$H(u,v)=\int_{-\infty}^{\infty}\int_{-\infty}^{\infty}h(x,y)e^{-j2\pi(ux+vy)}dxdy \quad \& \quad h(x,y)=\int_{-\infty}^{\infty}\int_{-\infty}^{\infty}H(u,v)e^{j2\pi(ux+vy)}dudv \qquad (2.22)$$

Non-Paraxial PSF Generation

The goal of this research effort is to be able determine if an object is a NEO or not and it is hypothesized that distant objects such as stars will not have any detectable tilt aberrations by any observation equipment on Earth. This is because the phase-front from a star will be flat across very large distances. Parallax is detected by measuring the tilt aberration in a phase-front that is not flat across the aperture of an observing telescope. Although GEO

objects have a limited amount of phase-front curvature, even massive telescopes would not be able to detect any parallax. An experimental setup to test this hypothesis is to utilize a reference telescope pointed directly at the detected object and secondary telescope pointed straight up to detect any parallax effects in the phase-front as seen in Figure 4. Such a set-up will allow the necessarily large baseline differences to detect parallax from NEO observations.

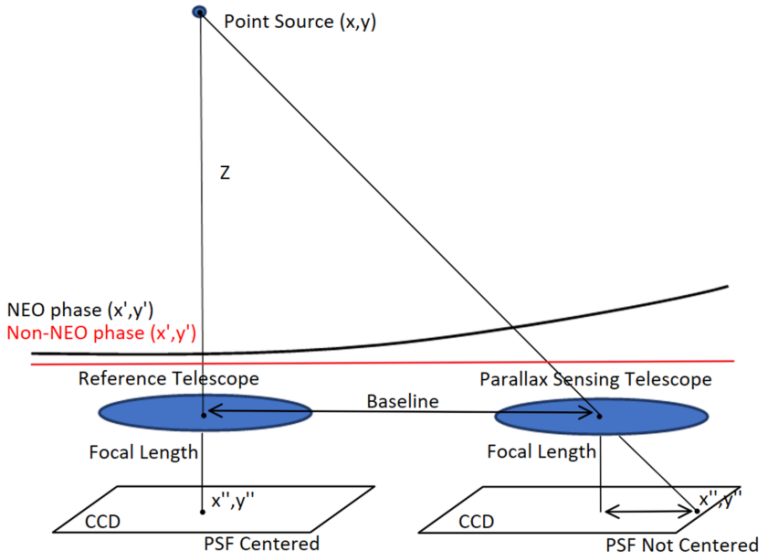

Figure 4: Visual Depiction of Telescope Arrangement for Parallax Detection

Using the Fraunhofer approximation (2.7), this phase from a distant but not infinitely far off object is propagated to a plane which contains both the reference telescope and the parallax sensing telescope. If there is curvature in the phase of an observed object across the telescope aperture, the resulting PSF will not be located at the center of the CCD due to the tilt aberrations in the phase. Because the object is so far away, it can be approximated as a point source and the field in the source plane is an impulse function represented mathematically by the dirac function. The integrand in the Fraunhofer approximation integrates to one and only the term outside the integral remains as seen in (2.23).

$$U_2(x',y') = \frac{e^{j2\pi z/\lambda} e^{j\pi(x'^2+y'^2)}}{j\lambda z} \int_{-\infty}^{\infty}\int_{-\infty}^{\infty} U_1(x,y) e^{-j2\pi(F_x x' + F_y y')} dxdy \text{ and } U_1(x,y) = \delta(x,y)$$
$$U_2(x',y') = \frac{e^{j2\pi z/\lambda} e^{j\pi(x^2+y^2)}}{j\lambda z} \tag{2.23}$$

Now that the field in the plane of the two telescopes has been obtained, the PSF's from each telescope need to be generated. Due to the small distance between the aperture and the CCD planes, the Fresnel approximation will be utilized. For the reference telescope, the PSF is the Fourier Transform of the aperture located at the center of the CCD array behind the telescope. This occurs due to the quadratic term in the integrand for the Fresnel propagator being canceled out by the phase delay of the lens as it is known that the PSF will be at the focal point at the center of the CCD. However, this is not the case for the parallax sensing telescope and special considerations will need to be taken to generate its PSF [13], [14]. A new coordinate system is created centered on where the PSF should be located as predicted by geometric optics as seen in Figure 5.

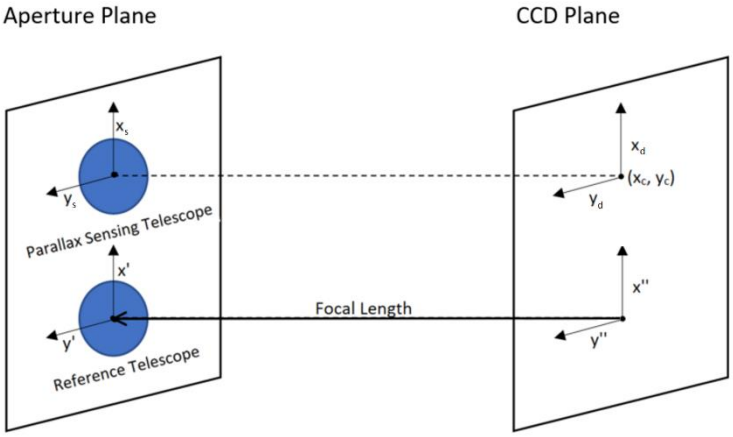

Figure 5: New Coordinate System for Non-Paraxial Propagation [13]

With this change of coordinate system, the Fresnel approximation needs to be modified. The first step is to change the R_{12} term seen in (2.3) needs to be modified. The x and y

coordinates in the CCD plane have been shifted away from the optical axis to a point centered at (x_c, y_c) and R_{12} is changed as seen in (2.24) where x_d and y_d are deviations from the center point.

$$R_{12} = \sqrt{z^2 + (x' - x'')^2 + (y' - y'')^2}$$
$$R_{12} = \sqrt{z^2 + (x' - x_c - x_d)^2 + (y' - y_c - y_d)^2} \tag{2.24}$$

where,

$$x'' \text{ is substituted with } x_c + x_d \text{ and } y'' \text{ is substituted with } y_c + y_d \tag{2.25}$$

Now, the binomial approximation can be made in the new coordinate system which will create a hybrid propagator to create a non-paraxial PSF.

$$R_{12} = \sqrt{z^2 + (x' - x_c - x_d)^2 + (y' - y_c - y_d)^2}$$
$$R_{12} = \sqrt{z^2 + (x_s - x_d)^2 + (y_s - y_d)^2} \tag{2.26}$$

here,

$$x' - x_c \text{ is substituted with } x_s \text{ and } y' - y_c \text{ is substituted with } y_s \tag{2.27}$$

As seen below, R_{12} has been re-written in terms of the new coordinate system and the term inside the square root is expanded to re-arrange the terms simplifying the binomial approximation.

$$R_{12=}\sqrt{z^2 + x_s^2 + x_d^2 - 2x_s x_d + y_s^2 + y_d^2 - 2y_s y_d} \tag{2.28}$$

$$R_{12} = \sqrt{R_0^2(x_s, y_s) + x_d^2 + y_d^2 - 2(x_s x_d + y_s y_d)} \tag{2.29}$$

where,

$$R_0^2(x_s, y_s) = z^2 + x_s^2 + y_s^2 \tag{2.30}$$

Equation (2.29) is re-arranged as seen in Equation (2.31) to get the expression into a form where, as is done for the Fresnel approximation [12], the binomial expansion of the square root term can be taken.

$$R_{12} = \sqrt{R_0^2(x_s, y_s) + \frac{R_0^2(x_s, y_s)\left(x_d^2 + y_d^2\right)}{R_0^2(x_s, y_s)} - \frac{\left(2R_0^2(x_s, y_s)(x_s x_d + y_s y_d)\right)}{R_0^2(x_s, y_s)}} \tag{2.31}$$

To make (2.31) fit the form required to take the binomial expansion, the distance to the point of interest is factored out as seen in Equation (2.32).

$$R_{12} = R_0(x_s, y_s)\sqrt{1 + \frac{\left(x_d^2 + y_d^2\right)}{R_0^2(x_s, y_s)} - \frac{2(x_s x_d + y_s y_d)}{R_0^2(x_s, y_s)}} \tag{2.32}$$

Equation (2.33) is the first two terms of the binomial approximation of R_{12} from (2.32) in the non-paraxial case. This is different than the R_{12} term used in the paraxial Fresnel propagator because the $R_0(x_s, y_s)$, term which replaced z contains information about where in the CCD the PSF is being generated at.

$$R_{12} = R_0(x_s, y_s)\left(1 + \frac{\left(x_d^2 + y_d^2\right)}{2R_0^2(x_s, y_s)} - \frac{(x_s x_d + y_s y_d)}{R_0^2(x_s, y_s)}\right) \tag{2.33}$$

This propagator replaces the z term in the Rayleigh-Sommerfeld propagator (2.1) with R_{12}, shown in Equation (2.34), which has been derived for a non-paraxial position [13].

$$U_2(x_d, y_d) = \frac{1}{j\lambda z}\int_{-\infty}^{\infty}\int_{-\infty}^{\infty} U_1(x_s, y_s) e^{\frac{j2\pi R_0(x_s, y_s)}{\lambda}} e^{\frac{j\pi(x_d^2 + y_d^2)}{\lambda R_0(x_s, y_s)}} e^{-j2\pi\frac{(x_d x_s + y_d y_s)}{\lambda R_0(x_s, y_s)}} dx_s dy_s \tag{2.34}$$

This propagation tool can be simplified if the term resembling the quadratic term can be neglected. As shown below, this term is always less than the quadratic term from the original propagator because $R_0(x_s, y_s)$ is always smaller than z; thus, the Fraunhofer approximation condition must be met for this term to be neglected or a lens must be utilized to cancel this quadratic phase term.

$$U_2(x_d, y_d) = \frac{1}{j\lambda z}\int_{-\infty}^{\infty}\int_{-\infty}^{\infty} U_1(x_s, y_s) e^{\frac{j2\pi R_0(x_2, y_2)}{\lambda}} \cancel{e^{\frac{j\pi(x_d^2 + y_d^2)}{\lambda R_0(x_2, y_2)}}} e^{-j2\pi\frac{(x_d x_2 + y_d y_2)}{\lambda R_0(x_2, y_2)}} dx_2 dy_2 \quad (2.35)$$

if

$$z \gg \frac{\pi({x_d}^2{}_{\max} + {y_d}^2{}_{\max})}{\lambda} \quad (2.36)$$

As mentioned in the previous section, the Fraunhofer propagation can be modeled as a Fourier Transform. The expression above still has $R_0(x_s, y_s)$ which is a function of the differential elements in the integral; $R_0(x_s, y_s)$ can be approximated as z if the radius of the resulting non-paraxial PSF, n_{max}, is smaller than the F# squared in units of Nyquist pixels [13], [14]. For the purposes of this paper, the PSF radius will be taken as the radius which creates a circle bounding 85-90% of the PSF energy. In this case, the expression is in the form of a Fourier Transform and the remaining $R_0(x_s, y_s)$ term contains the phase aberrations to propagate the off-axis PSF within the validity regions.

$$U_2(x_d, y_d) = \frac{1}{j\lambda z}\int_{-\infty}^{\infty}\int_{-\infty}^{\infty} U_1(x_s, y_s) e^{\frac{j2\pi R_0(x_s, y_s)}{\lambda}} e^{-j2\pi\frac{(x_d x_s + y_d y_s)}{\lambda z}} dx_s dy_s \quad (2.37)$$

If

$$n_{\max} < F\#^2 \text{ (in Nyquist Pixels)} \quad (2.38)$$

Effects of the Atmosphere

In the absence of the earth's atmosphere, the wave-fronts arriving from distant space objects such as stars or NEO's appear to be flat and the resulting PSF takes the form an airy disk, for a circular aperture. The performance of such an optical system is severely impacted by the random fluctuations of the atmosphere. This atmospheric turbulence causes random changes to the optical index of refraction which is both a function of space and time shifting the wave-front both spatially and temporally as it passes through the medium. These shifts cause the wave-front to have varying optical delays dependent on the paths taken through the medium resulting in a perturbed wave-front. The apparent twinkling of stars in the night sky result from this physical phenomenon. The resulting image seen at the detector is no longer a clear PSF and its nature depends on the exposure time of the system. Figure 6 demonstrates the effects of a turbulent atmosphere on an incident plane wave.

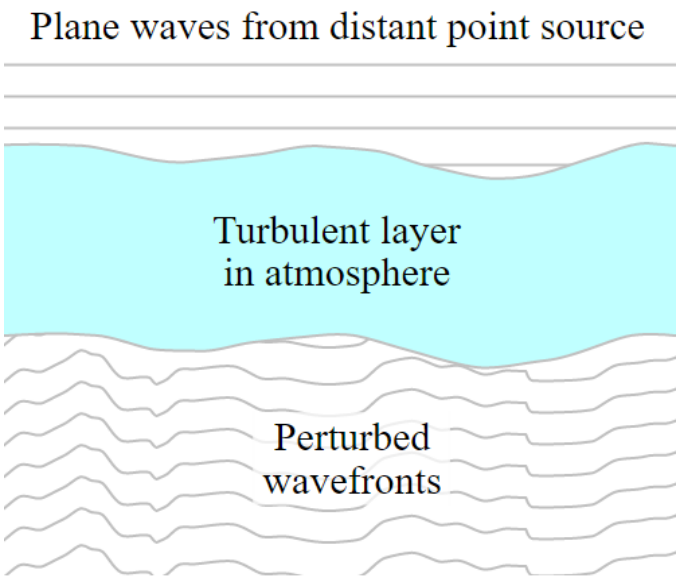

Figure 6: Effects of Atmospheric Turbulence on Plane Waves [15]

Kolmogorov was a Russian mathematician whose studies included modeling the statistics of a turbulent atmosphere. The Kolmogorov turbulence model assumes that perturbations to a wave front by the turbulent atmosphere are caused by fluctuations of the index of refraction of the atmosphere. In this way, the phase structure function is related to the optical delay different rays of light experience on different paths to the aperture through the atmosphere. Multiple rays arrive at different locations in the aperture from multiple paths and there is a correlation relating the optical delay time the different rays experience. Kolmogorov related the statistical model for the density of the atmosphere, as based on random fluctuations in temperature, directly to the index of refraction of the atmosphere. Kolmogorov's theories model temperature as a Wide Sense Stationary (WSS) Random Process. Index of refraction and density have a linear relationship. The statistics from thermal models of the atmosphere give rise to density as some function of temperature which gives rise to some statistical model of the index of refraction of the atmosphere. The phase delay, $\theta(x_1, y_1)$, one ray experiences to a point, (x_1,y_1), in the aperture can be represented by the below equation where Δn is a fluctuation in the index of refraction from some mean value, n_o.

$$\theta(x_1, y_1) = \frac{2\pi}{\lambda} \int_0^z \Delta n(x_1, y_1) dz \tag{2.39}$$

The index of refraction is a random number because there is a random temperature field in the atmosphere; it is modeled as a Gaussian random number that never goes below 1. Because the Gaussian Probability Distribution Function (PDF) has a tail which goes below 1, this model looks at the difference in phase between two points in the aperture separated by a distance, r, from each other. The structure function, Ds, is the expected value of this

phase difference squared and is a function of the difference between the two x and y coordinate locations, $\Delta x \,\&\, \Delta y$.

$$D_s(\Delta x, \Delta y) = E\left[\left(\theta(x_1, y_1) - \theta(x_2, y_2)\right)^2\right] \tag{2.40}$$

$$D_s(\Delta x, \Delta y) = E\left[\left(\theta(x_1, y_1) - \theta(x_2, y_2)\right)\left(\theta(x_1, y_1) - \theta(x_2, y_2)\right)\right] \tag{2.41}$$

After expanding the expression, the expectation can be taken onto each of the terms which results difference of the correlation of the phase at the same point and between two points. Because the correlation, R_θ, is only a function of the separation of the two points, this is said to be spatially WSS.

$$D_s(\Delta x, \Delta y) = E\left[\theta^2\left(x_1, y_1\right)\right] + E\left[\theta^2\left(x_2, y_2\right)\right] - E\left[\theta(x_1, y_1)\theta(x_2, y_2)\right] - E\left[\theta(x_2, y_2)\theta(x_1, y_1)\right] \tag{2.42}$$

$$D_s(\Delta x, \Delta y) = 2\left(R_\theta(0,0) - R_\theta(\Delta x, \Delta y)\right) \tag{2.43}$$

Substituting the expression for the phase delay at a given point in terms of the fluctuations of the atmosphere, Δn, into the above expectation math starts a rigorous mathematical derivation of Kolmogorov's structure function of the atmosphere.

$$E\left[\left(\theta(x_1, y_1) - \theta(x_2, y_2)\right)^2\right] = \frac{2\pi}{\lambda} E\left[\left(\int_0^z \Delta n(x_1, y_1) - \Delta n(x_2, y_2) dz\right)^2\right] \tag{2.44}$$

An expression for the structure function in terms of the auto-correlation of the index of refraction is developed as shown in Equation (2.45) where z' and z'' are two different paths to two points in the aperture, r is the separation between two points in the aperture plane found by computing the hypotenuse between points with a vertical separation of Δx and a horizontal separation of Δy and R_n is the auto-correlation function.

$$D_s(\Delta x,\Delta y)=\left(\frac{2\pi}{\lambda}\right)^2\int_0^z\int_0^z 2R_n(z'-z'')-2R_n\sqrt{(r^2+(z'-z'')^2}\,dz'\,dz'' \tag{2.45}$$

where,

$$r=\sqrt{\Delta x^2+\Delta y^2} \tag{2.46}$$

Kolmogorov only defined the Power Spectral Density (PSD) of the index of refraction. Normally, the auto-correlation function can be determined by taking the inverse Fourier transform of the PSD, but Kolmogorov's PSD has a discontinuity at zero frequency; auto-correlation function cannot be computed due to this. The expression can be put in terms of the structure function by adding and subtracting twice the auto-correlation function with zero shift.

$$D_s(\Delta x,\Delta y)=\left(\frac{2\pi}{\lambda}\right)^2\int_0^z\int_0^z -2R_n(0,0)+2R_n(z'-z'')+2R_n(0,0)-2R_n\sqrt{(r^2+(z'-z'')^2}\,dz'\,dz'' \tag{2.47}$$

$$D_s(\Delta x,\Delta y)=\left(\frac{2\pi}{\lambda}\right)^2\int_0^z\int_0^z -2D_n(z'-z'')+2D_n\sqrt{(r^2+(z'-z'')^2}\,dz'\,dz'' \tag{2.48}$$

$$D_s(\Delta x,\Delta y)=-\left(\frac{2\pi}{\lambda}\right)^2\int_0^z\int_0^z 2D_n(z'-z'')-2D_n\sqrt{(r^2+(z'-z'')^2}\,dz'\,dz'' \tag{2.49}$$

where,

$$D_n(r)=C_n^2(0,0)r^{\frac{2}{3}} \tag{2.50}$$

As defined, $D_n(r)$ is related to the variance of the fluctuation of the index of refraction, n, multiplied by the separation between two points of interest in the aperture to the two thirds power. $C_n(0,0)$ is the variance of the index of refraction and $C_n^2(0,0)$ is the auto-correlation function at zero shift. During the period, this relationship for the structure function of the atmospheric turbulence was developed, computers weren't powerful enough to evaluate

the above integral and further mathematical derivations resulted the numerical expression below. In this expression, r is the separation between two points in the aperture plane (2.46) and r_0 is Fried's seeing parameter.

$$D_s(r) = 6.88\left(\frac{r}{r_0}\right)^{5/3} \tag{2.51}$$

The seeing parameter is an indication of how much the paths to a point in an aperture can be separated. For separations smaller than r_0, the structure function becomes close to zero because a small number squared is a smaller number. For separations larger than r_0, the structure function becomes large. The value which r_0 takes on will determine how much of a factor the turbulence of the atmosphere plays in the performance of the optical system.

Average Optical Transfer Function

From the above description, the source field is assumed to be a plane wave until it is perturbed by the random fluctuations of the atmosphere's index of refraction. The phase term in the pupil function is altered by the atmosphere and this alteration is described mathematically by the Zernike phase screens [16]. The goal is to find an expression for the expected value of the OTF as a function of the of the random Zernike phase screens. Physically speaking, this is a form of long exposure imaging which many surveillance instruments utilize currently [9], [11]. We define the average transfer function, E[H(u,v)], of the system as the expected value of the OTF.

$$E[H(u,v)] = E\left[\frac{\int_{-\infty}^{\infty}\int_{-\infty}^{\infty} P(x,y)P^*(x-\bar{\lambda}fu, y-\bar{\lambda}fv)dxdy}{\int_{-\infty}^{\infty}\int_{-\infty}^{\infty}\left|P(x,y)\right|^2 dxdy}\right] \tag{2.52}$$

In the case being explored, the denominator is assumed to be a number which normalizes the OTF; this is because only the phase is random and the amplitude is not considered to be a random quantity. This allows the expectation to be taken on the numerator only since expectation is a linear operator. If the numerator were also a random quantity, it would undoubtedly have some correlation to the numerator and this step could not be taken. The random phase effects are in the numerator of this expression.

$$E[H(u,v)] = H(u,v) = \frac{E\left[\int_{-\infty}^{\infty}\int_{-\infty}^{\infty} P(x,y)P^{*}(x-\bar{\lambda}fu, y-\bar{\lambda}fv)dxdy\right]}{\int_{-\infty}^{\infty}\int_{-\infty}^{\infty}\left|P(x,y)\right|^{2}dxdy} \tag{2.53}$$

For the next several steps towards finding an expression for the expectation of the OTF, the denominator will be left out while keeping in mind that it needs to be added back later. The numerator is re-written in terms of the amplitude and phase of the pupil function while keeping in mind that the phase, Φ, is represented by the Zernike phase screens.

$$E[H(u,v)] \; \alpha \; E\left[\int_{-\infty}^{\infty}\int_{-\infty}^{\infty} A(x,y)e^{j\Phi(x,y)}A^{*}(x-\bar{\lambda}fu, y-\bar{\lambda}fv)e^{j\Phi(x-\bar{\lambda}fu, y-\bar{\lambda}fv)}dxdy\right] \tag{2.54}$$

Noting that the amplitude is not random, the numerator of the OTF is re-arranged, gathering the amplitude and phase terms together; this is valid when a single phase screen is used to represent the OTF. The expectation is brought past the amplitude expression onto the phase expression. To find the statistical representation of the average transfer function, the expectation of the phase expression must be resolved. Henceforward, the derivation will be geared towards finding this expectation and the result will be put back into the integral later.

$$E[H(u,v)] \alpha \int_{-\infty}^{\infty}\int_{-\infty}^{\infty} A(x,y)A^{*}(x-\bar{\lambda}fu, y-\bar{\lambda}fv)E\left[e^{j\Phi(x,y)}e^{j\Phi(x-\bar{\lambda}fu,y-\bar{\lambda}fv)}\right]dxdy \tag{2.55}$$

$$E[H(u,v)] \alpha \mathrm{E}\left[e^{j[\Phi(x,y)-\Phi(x-\bar{\lambda}fu,y-\bar{\lambda}fv)]}\right] \tag{2.56}$$

A non-random number multiplied by a Gaussian random number becomes a Gaussian random number and the difference of two Gaussian random numbers is also Gaussian random number; thus, $\Phi(x,y)$ is a Gaussian random number and $\Phi(x,y)-\Phi(x-\bar{\lambda}fu, y-\bar{\lambda}fv)$ is a Gaussian random number. Looking specifically at difference between the phase term at a point and the phase term at a shifted point, we define a Gaussian random number, $\Delta(\bar{\lambda}fu, \bar{\lambda}fv)$. Because this Gaussian random number is a function of a spatial difference only, it is Wide Sense Stationary spatially.

$$\Delta(\bar{\lambda}fu, \bar{\lambda}fv) = \Phi(x,y)-\Phi(x-\bar{\lambda}fu, y-\bar{\lambda}fv) \tag{2.57}$$

Taking the expectation of this expression, it is noted that this expectation is in a form very similar to that of the characteristic function, $M_u(w)$, as by Goodman [17].The expectation of this expression can be more easily solved using the characteristic function where $\bar{u}$ is the mean, w is the frequency variable in the Fourier transform, and σ^2 is the variance.

$$E[H(u,v)] \alpha \mathrm{E}\left[e^{j\Delta(\bar{\lambda}fu,\bar{\lambda}fv)}\right] \tag{2.58}$$

$$E[e^{jwu}] = M_u(w) = e^{\left[jw\bar{u}-\frac{w^2\sigma^2}{2}\right]} \tag{2.59}$$

The characteristic function is like the Fourier transform of the Probability Distribution Function (PDF) being evaluated at various w values. In this case, all the values of w are not meaningful and the key to solving this expectation is setting w equal to 1. Remembering

that the Gaussian random numbers were zero mean, $\bar{u}=0$, with w equal to 1, the characteristic function, $M_u(w)$, is shown below.

$$M_u(w) = e^{-\frac{\sigma_\Delta^2}{2}} \tag{2.60}$$

Next, the variance of $\Delta(\bar{\lambda} fu, \bar{\lambda} fv)$, σ_Δ^2, needs to be computed. The variance is just the expected value of delta squared, $E\left[\Delta^2\right]$, due to the mean of the Gaussian random number being zero. This expectation is computed below.

$$\sigma_\Delta^2 = E\left[\Delta^2\right] = E\left[\left(\Phi(x,y) - \Phi(x-\bar{\lambda} fu, y-\bar{\lambda} fv)\right)\left(\Phi(x,y) - \Phi(x-\bar{\lambda} fu, y-\bar{\lambda} fv)\right)\right] \tag{2.61}$$

$$\sigma_\Delta^2 = E\left[\Phi^2(x,y)\right] + E\left[\Phi^2(x-\bar{\lambda} fu, y-\bar{\lambda} fv)\right] - E\left[\Phi(x,y)\Phi(x-\bar{\lambda} fu, y-\bar{\lambda} fv)\right] - E\left[\Phi(x-\bar{\lambda} fu, y-\bar{\lambda} fv)\Phi(x,y)\right] \tag{2.62}$$

These expectations are the correlations of the phase screen with itself where $E\left[\Phi^2(x,y)\right]$ and $E\left[\Phi^2(x-\bar{\lambda} fu, y-\bar{\lambda} fv)\right]$ is the correlation of the phase screen with zero shift, $R_\Phi(0,0)$ and $E\left[\Phi(x,y)\Phi(x-\bar{\lambda} fu, y-\bar{\lambda} fv)\right]$ and $E\left[\Phi(x-\bar{\lambda} fu, y-\bar{\lambda} fv)\Phi(x,y)\right]$ is the correlation of the phase screen with a shift, $R_\Phi(\bar{\lambda} fu, \bar{\lambda} fv)$. The variance can be rearranged in terms of the correlation functions.

$$D_\Phi(\bar{\lambda} fu, \bar{\lambda} fv) = \sigma_\Delta^2(\bar{\lambda} fu, \bar{\lambda} fv) = 2\left(R_\Phi(0,0) - R_\Phi(\bar{\lambda} fu, \bar{\lambda} fv)\right) \tag{2.63}$$

$D_\Phi(\bar{\lambda} fu, \bar{\lambda} fv)$ is the structure function for this random process; the characteristic function can be written in terms of the structure function. It is noted that the form of this random process is the same as that of Kolmogorov's structure function for the atmosphere. This expression can be substituted into the relationship for the average transfer function.

$$M_u(w) = \mathrm{E}\left[e^{j\Delta(\bar{\lambda} fu, \bar{\lambda} fv)} \right]_{w=1} = e^{-\frac{D_\Phi(\bar{\lambda} fu, \bar{\lambda} fv)}{2}} \tag{2.64}$$

$$E[H(u,v)] \; \alpha \int_{-\infty}^{\infty} \int_{-\infty}^{\infty} A(x,y) A^*(x - \bar{\lambda} fu, y - \bar{\lambda} fv) e^{-\frac{D_\Phi(\bar{\lambda} fu, \bar{\lambda} fv)}{2}} dxdy \tag{2.65}$$

The characteristic function of the atmospheric phase term, $\overline{H_s}$, is not a function of the integration variables and can be pulled outside the integral. The average transfer function is re-written with this term factored out and with the normalization factor in the denominator.

$$E[H(u,v)] \; \alpha \; \frac{\int_{-\infty}^{\infty} \int_{-\infty}^{\infty} A(x,y) A^*(x - \bar{\lambda} fu, y - \bar{\lambda} fv) dxdy}{\int_{-\infty}^{\infty} \int_{-\infty}^{\infty} E\left|A(x,y)\right|^2 dxdy} \overline{H_s} \tag{2.66}$$

where,

$$\overline{H_s} = e^{-\frac{D_\Phi(\bar{\lambda} fu, \bar{\lambda} fv)}{2}} \tag{2.67}$$

The term on the left of the average transfer function expression is the transfer function of a perfect pupil with no phase error. This term will be defined as H_o; thus, the average transfer function is the transfer function of the telescope multiplied by the transfer function of the atmosphere. As noted before, the transfer function of the atmosphere is completely dependent on the auto-correlation of the atmospheric phase term. The expectation of the optical transfer function is thus $H_o \overline{H_s}$. The atmosphere has a specific phase structure function, D_s, as defined by Kolmogorov which can be substituted directly with $D_\Phi(\bar{\lambda} fu, \bar{\lambda} fv)$ in the equation for $\overline{H_s}$ [17].

$$\overline{H_s}(u,v) = e^{-\frac{D_s(\bar{\lambda} fr)}{2}} \tag{2.68}$$

$$\overline{H_s}(u,v) = e^{-3.44\left(\bar{\lambda} f \frac{\sqrt{u^2+v^2}}{r_o}\right)^{5/3}} \tag{2.69}$$

The transfer function of the atmosphere is only dependent on the spatial frequencies, the seeing parameter, the focal length of the optical system and the average wavelength. From this expression, when the structure function becomes large, the transfer function goes to zero and when the structure function becomes small, the transfer function is maximized. The structure function depends on the distance between two points in the aperture and the seeing parameter; thus, the size of the telescope as compared to the seeing parameter determines the effect of the atmosphere on the optical system's performance.

Photon Counting Noise

Physical hardware being used in an experiment registers objects by detecting photons from that object. An object may be viewed as an optical source producing N photons which can go anywhere for all time. The individual photon arrivals are assumed to be statistically independent and identically distributed. A binomial distribution may be used to model K photon arrivals at the detector during a finite time given N total photons produced over all time by the source. A binomial distribution is typically used to compute K successes in N trials. The camera will only be integrating during a finite amount of time and P_s is the expected number of photon arrivals at the detector during that finite time divided by the total number of photons, *N*. The expected number of photons is found by integrating the rate function, $\zeta(t)$, in units of photons per second during the time the camera is integrating. P_s can be thought of as the percentage of photons arriving at the detector during the integration time, t_2-t_1.

$$\Pr(K) = \frac{N!}{K!(N-K)!} P_s^K (1-P_s)^{N-K} \tag{2.70}$$

where,

$$P_s = \frac{1}{N} \int_{t_1}^{t_2} \zeta(t) dt \tag{2.71}$$

Due to Heisenberg's uncertainty principle, the arrival time of a photon at a detector cannot be predicted perfectly. This lack of knowledge regarding the photon's arrival statistics creates noise called photon counting noise. The expression for Pr(K) needs to be modified because there is no way to know how many photons, in total, are emitted by the source. The key to determining the expression for Pr(K) comes from Goodman [17]; we take the limit of Pr(K) as the total number of photons, N, goes to infinity.

$$\underset{N\to\infty}{Lim} \Pr(K) = \underset{N\to\infty}{Lim} \left(\frac{N!}{K!(N-K)!} P_s^K (1-P_s)^{N-K} \right) \tag{2.72}$$

Calculus tells us that when taking the limit of a multiplicative expression, that it's limit is the same as the multiplicative factors limits being multiplied together. To make the derivation more straightforward, the expression is broken apart into two separate parts and the limit as N goes to infinity is taken.

$$\underset{N\to\infty}{Lim} \Pr(K) = \underset{N\to\infty}{Lim} \left(\frac{N!}{K!(N-K)!} P_s^K \right) \cdot \underset{N\to\infty}{Lim} \left((1-P_s)^{N-K} \right) \tag{2.73}$$

The factorials in the left expression are expanded and all of the terms in the denominator cancel all of the terms in the numerator with the exception of the first N(N-1)…(N-K+1) terms. This expression can be expanded into a polynomial using algebra.

$$\underset{N\to\infty}{Lim} \left(\frac{N!}{K!(N-K)!} P_s^K \right) = \frac{N(N-1)...(N-K+1)\cancel{(N-K)(N-K-1)...1}}{K!\cancel{(N-K)(N-K-1)...1}} \left(\frac{1}{N} \int_{t_1}^{t_2} \zeta(t) dt \right)^K \tag{2.74}$$

where,

$$N(N-1)...(N-K+1) = N^K + C_1 N^{K-1} + C_2 N^{K-2} ... C_K N^0 \tag{2.75}$$

The N^K term in the denominator comes from P_s and taking the limit of the polynomial in the numerator divided by N^K goes to 1 in the limit where N goes to infinity.

$$\lim_{N\to\infty}\left(\frac{N!}{K!(N-K)!}P_s^K\right) = \lim_{N\to\infty}\frac{N^K + C_1 N^{K-1} + C_2 N^{K-2} ... C_K N^0}{K! N^K}\left(\int_{t_1}^{t_2}\zeta(t)dt\right)^K \tag{2.76}$$

where,

$$\lim_{N\to\infty}\frac{N^K + C_1 N^{K-1} + C_2 N^{K-2} ... C_K N^0}{N^K} = 1 \tag{2.77}$$

$$\lim_{N\to\infty}\left(\frac{N!}{K!(N-K)!}P_s^K\right) = \frac{(1)}{K!}\left(\int_{t_1}^{t_2}\zeta(t)dt\right)^K \tag{2.78}$$

Next, the limit as N goes to infinity of the second expression is taken. Because N is much bigger than K, the K term is dropped from the exponential. An exponent rule, shown below, demonstrates that that this limit becomes an exponential with x being negative the integral of the rate function during the integration time.

$$\lim_{N\to\infty}\left((1-P_s)^{N-K}\right) = \lim_{N\to\infty}\left(1-\frac{1}{N}\int_{t_1}^{t_2}\zeta(t)dt\right)^N \tag{2.79}$$

where,

$$\lim_{N\to\infty}\left(1+\frac{x}{N}\right)^N = e^x \tag{2.80}$$

$$\lim_{N\to\infty}\left((1-P_s)^{N-K}\right) = e^{-\int_{t_1}^{t_2}\zeta(t)dt} \tag{2.81}$$

The two terms can be combined to come up with the resultant form of the expression. The final expression seen below is that of a Poisson distribution. This proof shows that given the assumptions that our source emits a very large number of photons, the expected number of photon arrivals, K, at the detector follows a Poisson distribution.

$$\lim_{N\to\infty} \Pr(K) = \lim_{N\to\infty}\left(\frac{N!}{K!(N-K)!}P_s^K\right)\cdot \lim_{N\to\infty}\left((1-P_s)^{N-K}\right) \tag{2.82}$$

$$\lim_{N\to\infty} \Pr(K) = \frac{\left(\int_{t_1}^{t_2}\zeta(t)dt\right)^K}{K!}e^{-\int_{t_1}^{t_2}\zeta(t)dt} = \frac{\overline{K}^K e^{-\overline{K}}}{K!} \tag{2.83}$$

The number of expected photon arrivals from an observation will be computed using a magnitude scale and the background photons will be selected to achieve desired SNR values. Based on these derivations for photon arrivals, it is assumed that the distribution of the noise for the observations in this experiment will follow a Poisson distribution.

Decomposing Aberrations into Zernike Polynomial Bases

The effect of parallax on an optical system manifests itself in the form of detectable aberrations to the phase which alters the spatial distribution of that system's PSF. In the case being explored, the parallax sensing telescope's PSF will differ from the reference telescope PSF or the parallax sensing telescope's PSF when observing a star due to these aberrations. The changes to the PSF may not be easily distinguishable due to multiple aberrations superimposing effect the total PSF. A useful way to quantify these changes to the PSF's spatial distribution is using Zernike polynomials to decompose the aberrations into an orthogonal bases set.

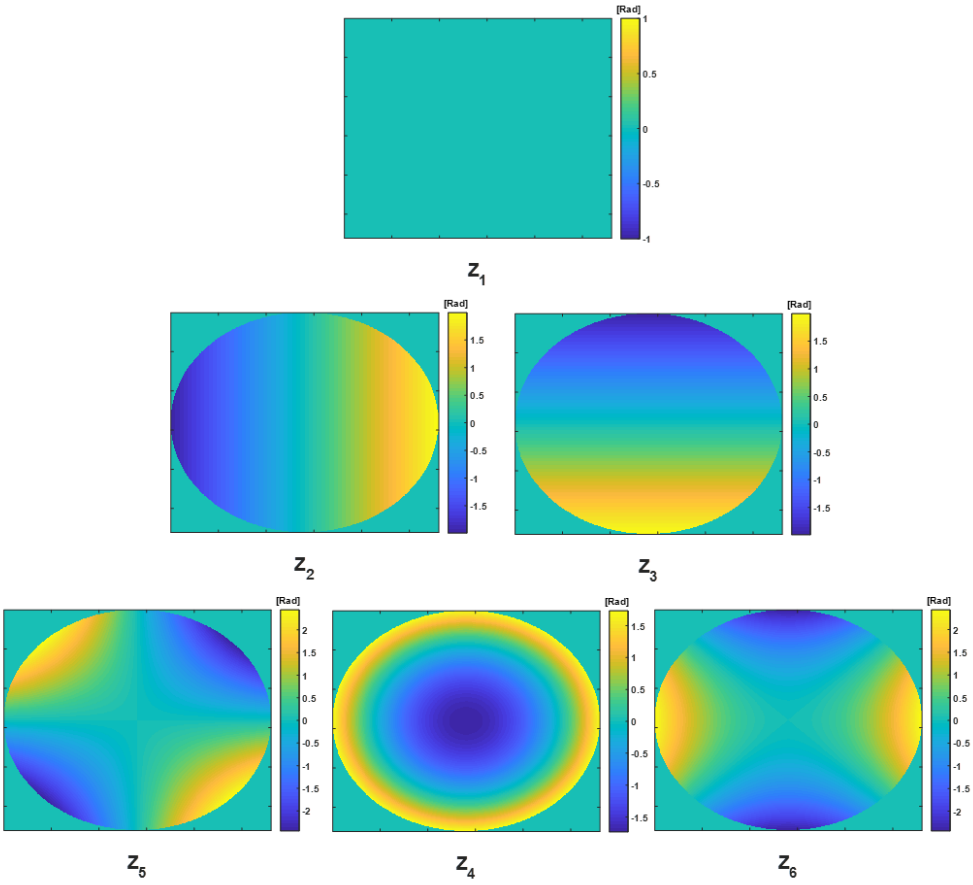

Figure 7: First Six Zernike Polynomials

The use of the Zernike polynomial is convenient because these polynomials form an orthonormal basis set over a unit circle and the telescope aperture is radially symmetric. The phase, $\phi(x,y)$, of the wave-front may be represented by a superposition of these Zernike polynomials, Z_N, multiplied by the corresponding weighting factors, a_N.

$$\phi(x,y) = a_1 \cdot Z_1(x,y) + a_2 \cdot Z_2(x,y) + ... + a_N \cdot Z_N(x,y) \qquad (2.84)$$

The Zernike coefficient weighting factors can be computed by taking area under the inner product between the total phase and the Zernike polynomial of interest and normalizing it

by the area under the aperture function multiplied by the Zernike polynomial squared.

$$a_i = \frac{\iint Z_i(x,y)\cdot\phi(x,y)dxdy}{\iint Z_i^2\cdot A(x,y)dxdy} \tag{2.85}$$

These coefficients will be useful to represent the parallax effect in terms of distinct optical aberrations to the phase at the CCD array. The tilt aberration, which is decomposed into Z_2 and Z_3, will cause the PSF as seen in the parallax sensing telescope to be in a different horizontal and vertical geometric position as compared to the PSF of the reference telescope. The phase at the pupil of the parallax sensing telescope will be used to quantify the magnitude of the parallax effect; the tilt aberration weighting coefficients a_2 or a_3 will be larger in magnitude as the distance between the two telescopes increases. The geometric optics setup to induce tilt into an optical system is seen in Figure 8 and Figure 9 shows the Zernike polynomial representation of tilt.

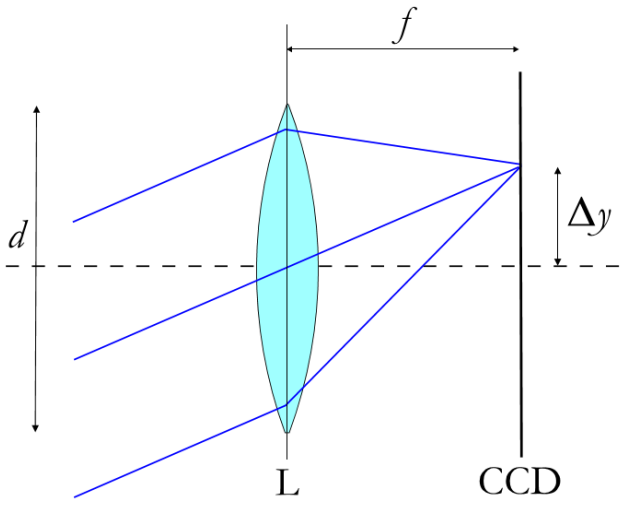

Figure 8: Physical Cause of Tilt Aberration [18]

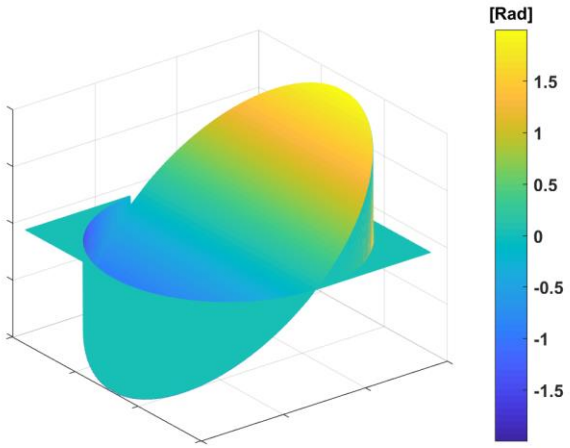

Figure 9: Tilt Aberration as Described by a3 Zernike Polynomial

The pupil function, $P(x, y)$ can also be represented using the superposition of Zernike polynomials as seen below [12], [11] where $A(x, y)$ is the aperture transmittance function and $\phi(x, y)$ is the phase at the aperture as described by a weighted superposition of Zernike polynomials as seen in (2.84).

$$P(x, y) = A(x, y) \cdot e^{j \cdot \phi(x,y)} \tag{2.86}$$

III. Detection Algorithm Methodology

This chapter shows the formulation of the PD and CD algorithms used for space object detection which are currently being used by ground based optical sensors and shows the formulation for the CD MHT algorithm developed by Zingarelli [10], [11] previously. A new CD MHT algorithm for detecting a target and categorizing that target as either a stellar or NEO observation in a single data frame is derived for scenarios where the optical system consists of identical or different telescopes separated by a given baseline. Useful performance metrics are derived to quantify the performance of the new algorithm in terms of statistical probabilities.

Point Detection

Different detection schemes are used by ground based electro-optic sensors to search for space objects. The ideal detection scheme is related to the exposure time of the sensor because moving objects will appear to be streaks if the sensor integration time is longer. If the exposure time is short enough or the telescope mount is moving at a rate consistent with objects in a particular orbit, moving objects or stars will not form streaks on the CCD detector and such observations can be treated as point sources [10], [11]. Because geostationary objects do not move, they can also be treated as point sources. The detection scheme known as a point detector (PD), is utilized to determine whether a given pixel has a detection or background present. For the derivation of this method, two hypotheses are considered; the hypothesis that a pixel contains a detection, H_1, and the hypothesis that a pixel contains background, H_0. These binary hypotheses are divided, former by the latter, to form a ratio called the Likelihood Ratio Test (LRT). A statistical model for the two data

sets must be determined to formulate a mathematical model for this test; in the context of this paper, it is assumed that the data takes on a Gaussian distribution [10], [11]. The Probability Distribution Function (PDF) of which is seen in (3.1) where d is the data, m is the mean of the Gaussian data and σ^2 is the variance of the Gaussian data.

$$P_D(d) = \frac{1}{\sqrt{2\pi\sigma^2}} e^{-(d-m)^2/2\sigma^2} \tag{3.1}$$

The data being observed through a telescope exists in every pixel of a CCD and this data will have a mean and standard deviation which is dependent on a region around that pixel. For H_1, the mean is the signal strength of the object in that pixel, S, plus the background, B, and for H_0, the mean is just the background, B. Shown below is the representation for the mean with an object present (3.2) and with background present (3.3).

$$m_{H_1} = S + B \tag{3.2}$$

$$m_{H_0} = B \tag{3.3}$$

The LRT is set up by making a ratio of the two Gaussian PDF's with different means. The goal is to find a threshold, γ, which can be used to determine if a detection is present in the data being tested. The LRT is seen below (3.4).

$$\Lambda = \frac{P_D(d \mid H_1)}{P_D(d \mid H_0)} = \frac{\frac{1}{\sqrt{2\pi\sigma^2}} e^{-(d-S-B)^2/2\sigma^2}}{\frac{1}{\sqrt{2\pi\sigma^2}} e^{-(d-B)^2/2\sigma^2}} \tag{3.4}$$

The above expression is expanded and simplified to produce a more concise expression (3.5).

$$\Lambda = \frac{P_D(d \mid H_1)}{P_D(d \mid H_0)} = e^{2S(d-B)-S^2/2\sigma^2} \tag{3.5}$$

The ratio is compared to a threshold, γ, of 1 because any result greater than 1 will indicate that the probability of H_1 occurring is greater than the probability of H_0 occurring and vice versa.

$$\text{if } \frac{P_D(d \mid H_1)}{P_D(d \mid H_0)} > 1, \text{ then } H_1 \text{ is true}$$
$$\text{if } \frac{P_D(d \mid H_1)}{P_D(d \mid H_0)} < 1, \text{ then } H_0 \text{ is true} \tag{3.6}$$

The limitation exists that the signal level of some object, S, is not known a-priori so it's presence in the LRT creates a problem. Because the threshold was set equal to 1, the natural log of both sides can be taken to change the exponential function into a ratio.

$$\Lambda = \ln\left(e^{2S(d-B)-S^2/2\sigma^2}\right) = \ln(1) \tag{3.7}$$

$$\Lambda = \frac{P_D(d \mid H_1)}{P_D(d \mid H_0)} = \frac{2S(d-B)-S^2}{2\sigma^2} = 0 \tag{3.8}$$

$$\Lambda = \frac{P_D(d \mid H_1)}{P_D(d \mid H_0)} = \frac{2S(d-B)}{2\sigma^2} = \frac{S^2}{2\sigma^2} \tag{3.9}$$

$$\Lambda = \frac{P_D(d \mid H_1)}{P_D(d \mid H_0)} = \frac{(d-B)}{\sigma} \underset{<}{>} \frac{S}{2\sigma} = \gamma \tag{3.10}$$

If the data under the H_0 hypothesis is Gaussian, subtracting B from d produces a zero-mean random number and then dividing that zero-mean random number by its standard deviation transforms that number into a Gaussian random number with a unit standard deviation. This is also called a normal random variable whose probability can be computed using tables for such distributions. The threshold, γ, can be set to some number of standard deviations to provide a desired false alarm probability based on the tables. For example, setting γ equal to 6 results in a false alarm probability of 10^{-9} for 1 pixel. An SNR higher than 6 is used for the threshold of detection for SST observations [11]. Also convenient is that the expression is equivalent to the Signal to Noise Ratio (SNR) of the pixel from dividing the signal by its noise.

$$\begin{aligned} SNR = \frac{(d - B)}{\sigma} > \gamma \text{ tells us } H_1 \text{ is more likely} \\ \text{or} \\ SNR = \frac{(d - B)}{\sigma} < \gamma \text{ tells us } H_0 \text{ is more likely} \end{aligned} \tag{3.11}$$

Correlation Detection

An extension to the LRT is using Correlation Detection (CD) which can also be thought of as a matched filter [11]. Previously, the LRT detected whether an object was present in each pixel by testing every pixel against the LRT ratio using the local mean and standard deviation of a data set. CD looks at the ratio of probabilities given the statistics of the entire data set within some window. The PDF is like the one used before, but now it represents a frame of data rather than one pixel. This method should be more perceptive than the point detector because it can compare a whole distribution of data.

$$P_D(d) = \prod_{x=1}^{N}\prod_{y=1}^{N} \frac{1}{\sqrt{2\pi}\sigma} e^{-(d(x,y)-m)^2/2\sigma^2} \tag{3.12}$$

The probability of the data being used to compute the PDF at each pixel is multiplied together over the entire widow where N is the total number of pixels in the x or y direction. The mean given the H_1, m_{H_1}, case is now altered by multiplying the signal strength, S, by the Point Spread Function (PSF), h(x,y), of the expected object and the mean given the H_0, m_{H_0}, case is the same as before. The equations below show the representation for the mean with an object present and without an object present.

$$m_{H_1} = S \cdot h(x,y) - B \tag{3.13}$$

$$m_{H_0} = B \tag{3.14}$$

A ratio of the two PDFs is made; again, the goal is to find a threshold, γ, which can be used to determine if a whole window of observed data has an object, H_1, or doesn't have an object present, H_0. The division of the PDF's is seen below.

$$\frac{P_D(d \mid H_1)}{P_D(d \mid H_0)} = \frac{\prod_{1}^{N}\prod_{1}^{N} \frac{1}{\sqrt{2\pi\sigma^2}} e^{-(d(x,y)-Sh(x,y)-B)^2/2\sigma^2}}{\prod_{1}^{N}\prod_{1}^{N} \frac{1}{\sqrt{2\pi\sigma^2}} e^{-(d(x,y)-B)^2/2\sigma^2}} \tag{3.15}$$

This expression will be mathematically manipulated into the form of a correlation rather than a ratio and compared to a threshold. All the algebraic steps are the same as before with the only difference being that S became S multiplied by the PSF and that data in the whole window is being multiplied together. The exponential terms are expanded, eliminated and re-combined simplifying the expression.

$$\Lambda = \frac{P_D(d \mid H_1)}{P_D(d \mid H_0)} = \prod_1^N \prod_1^N e^{2Sh(x,y)(d-B)-S^2h(x,y)^2/2\sigma^2} \tag{3.16}$$

The new expression used for correlation detection LRT is very similar to the expression for the point detector LRT just and as before, the threshold, γ, is set equal to 1 because a result greater than 1 will mean the hypothesis given an object is present, H_1, is more likely and a result less than 1 will mean that the hypothesis given there is no object present, H_0, is more likely. The natural log of the CD LRT is taken resulting in the natural log of the CD ratio on the left and of the threshold on the right. One of the properties of a logarithmic base is that the log of a product becomes sums. Taking the natural log of a product of exponents gets rid of the exponential base and changes the products to sums as seen below.

$$\ln(\Lambda) = \ln\left(\prod_1^N \prod_1^N e^{2Sh(x,y)(d-B)/2\sigma^2} e^{-S^2h(x,y)^2/2\sigma^2} \right) \underset{<}{>} \ln(1) \tag{3.17}$$

$$\sum_{x=1}^N \sum_{y=1}^N \frac{(2Sh(x,y)(d(x,y)-B)}{2\sigma^2} - \frac{S^2h^2(x,y)}{2\sigma^2} \underset{<}{>} 0 \tag{3.18}$$

The expression which relies on the unknown signal, *S*, is moved to the right-hand side and the signal is divided out of the left-hand side of the expression. This eliminates the reliance within the CD test on the signal strength, S, of an observed object.

$$\sum_{x=1}^N \sum_{y=1}^N \frac{(2S \cdot h(x,y) \cdot (d(x,y)-B)}{2\sigma^2} \underset{<}{>} \sum_1^N \sum_1^N \frac{S^2 \cdot h^2(x,y)}{2\sigma^2} \tag{3.19}$$

As before, the resulting expression is analogous to the SNR. The operation in the left-hand side of (3.19) is taking the PSF and data grid, multiplying them together and summing up the product which is correlation. (3.19) is put in terms of a correlation of the data in a window with an expected PSF in (2.20).

$$\Lambda = \sum_{x=1}^{N}\sum_{y=1}^{N}(h(x,y)\cdot(d(x,y)-B) \gtrless \sum_{x=1}^{N}\sum_{y=1}^{N}\frac{S\cdot h^2(x,y)}{2} = \gamma \tag{3.20}$$

To come up with an expression for the CD which follows a normal Gaussian distribution, the CD needs to be divided by its standard deviation. The variance of the LRT is the expected value of the of the LRT squared.

$$E\left[\Lambda^2\right] = E\left[\sum_{x_1=1}^{N}\sum_{y_1=1}^{N}(h(x_1,y_1)(d(x_1,y_1)-B)\sum_{x_2=1}^{N}\sum_{y_2=1}^{N}(h(x_2,y_2)(d(x_2,y_2)-B)\right] \tag{3.21}$$

$$E\left[\Lambda^2\right] = \sum_{x_1=1}^{N}\sum_{y_1=1}^{N}\sum_{x_2=1}^{N}\sum_{y_2=1}^{N}E\left[(d(x_1,y_1)-B)\right]E\left[(d(x_2,y_2)-B)\right]h(x_1,y_1)h(x_2,y_2) \tag{3.22}$$

There are two cases in the above sum, one where the terms in the sum are equal, $x_1=x_2$ and $y_1=y_2$, and one where they are all different. In the latter case, the data and background are statistically independent, and the expectation of the product becomes the product of the expectations. Because the background data, B, has a zero mean, the term is multiplied by zero. The only remaining terms are the second case when $x_1=x_2$ and $y_1=y_2$ in the sums [11].

$$E[\Lambda^2]_{x_1\neq x_2 \& y_1\neq y_2} + E[\Lambda^2]_{x_1=x_2 \& y_1=y_2} = \sum_{x_1=1}^{N}\sum_{y_1=1}^{N}\sum_{x_2=1}^{N}\sum_{y_2=1}^{N}(1-\delta(x_1-x_2,y_1-y_2))E\left[(d(x_1,y_1)-B)\right]E\left[(d(x_2,y_2)-B)\right](h^2(x_2,y_2))\ldots \tag{3.23}$$
$$\sum_{x_1=1}^{N}\sum_{y_1=1}^{N}\sum_{x_2=1}^{N}\sum_{y_2=1}^{N}\delta(x_1-x_2,y_1-y_2)E\left[(d(x_1,y_1)-B)^2\right](h^2(x_1,y_1)$$

$$E[\Lambda^2]_{x_1\neq x_2 \& y_1\neq y_2} + E[\Lambda^2]_{x_1=x_2 \& y_1=y_2} = \sum_{x_1=1}^{N}\sum_{y_1=1}^{N}\sum_{x_2=1}^{N}\sum_{y_2=1}^{N}(1-\delta(x_1-x_2,y_1-y_2))\cancel{\left(E\left[(d(x_1,y_1)-B\right]\right)^{=0}}\cancel{\left(E\left[(d(x_2,y_2)-B\right]\right)^{=0}}(h^2(x_1,y_1)+ \quad (3.24)$$
$$\ldots \sum_{x_1=1}^{N}\sum_{y_1=1}^{N}\sum_{x_2=1}^{N}\sum_{y_2=1}^{N}\delta(x_1-x_2,y_1-y_1)E\left[(d(x_1,y_1)-B)^2\right](h^2(x_1,y_1)$$

The resulting expression contains the expectation of the data minus the background squared which is, by definition, the variance. The standard deviation, σ_Λ, is computed by taking the square root of the computed variance.

$$E\left[\Lambda^2\right] = \sigma^2\sum_{x_1=1}^{N}\sum_{y_1=1}^{N}h^2(x_1,y_1) \quad (3.25)$$

$$\sigma_\Lambda = \sqrt{E\left[\Lambda^2\right]} = \sqrt{\sigma^2\sum_{x_1=1}^{N}\sum_{y_1=1}^{N}h^2(x_1,y_1)} = \sigma\sqrt{\sum_{x_1=1}^{N}\sum_{y_1=1}^{N}h^2(x_1,y_1)} \quad (3.26)$$

The LRT expression for the CD is divided by its standard deviation resulting in a zero-mean unit variance random variable. The expression is now a ratio of the signal divided by the noise; thus, normalized in terms of SNR. The expression can be compared to the threshold which is again set to be some number of standard deviations allowing probability of false alarm to be minimized based on tables. The right-hand side of the expression for the SNR is set to be the threshold, γ.

$$SNR = \frac{\sum_{x=1}^{N}\sum_{y=1}^{N}h(x,y)\cdot(d(x,y)-B)}{\sigma\sqrt{\sum_{x=1}^{N}\sum_{y=1}^{N}h^2(x,y)}} \underset{<}{>} \frac{\sum_{x=1}^{N}\sum_{y=1}^{N}S\cdot h^2(x,y)}{2\sigma\sqrt{\sum_{x=1}^{N}\sum_{y=1}^{N}h^2(x,y)}} = \gamma \quad (3.27)$$

$$SNR = \frac{\sum_{x=1}^{N}\sum_{y=1}^{N} h(x,y)(d(x,y)-B)}{\sigma\sqrt{\sum_{x=1}^{N}\sum_{y=1}^{N} h^2(x,y)}} > \gamma \text{ tells us } H_1 \text{ is more likely}$$

or (3.28)

$$SNR = \frac{\sum_{x=1}^{N}\sum_{y=1}^{N} h(x,y)(d(x,y)-B)}{\sigma\sqrt{\sum_{x=1}^{N}\sum_{y=1}^{N} h^2(x,y)}} < \gamma \text{ tells us } H_0 \text{ is more likely}$$

If the PSF were taken to be a delta function, the SNR expression reduces to the same expression derived for the PD LRT case and the two cased can be directly compared to each other to determine which method is superior; the method resulting in the highest SNR has the highest performance [11].

Multi-Hypothesis Test

Using the model for the CD, the implementation of the Multi-Hypothesis Test (MHT) detector is straightforward. Because every optical system is unique, different system configurations will result in a unique spatial distribution of that system's PSF. The parallax effect will be manifested in more pronounced tilt aberrations which will both move the location of and change the shape of the PSF. The hypothesis corresponding to an observed window of data will be distinguishable when input into the CD LRT with the appropriate PSF used in the correlator. Multiple hypotheses, H_i, are defined by setting the ith PSF, $h_i(x,y)$, expected by a given optical system under the a priori condition that said hypothesis has occurred.

$$SNR_i = \frac{\sum_{x=1}^{N}\sum_{y=1}^{N} h_i(x,y)\cdot(d(x,y)-B)}{\sigma\sqrt{\sum_{x=1}^{N}\sum_{y=1}^{N} h_i^2(x,y)}} \underset{<}{>} \gamma \tag{3.29}$$

If the data being tested does not correspond to the optical system hypothesized, the outputs of the CD LRT will be lower than when hypothesizing the correct optical system [10]. The hypothesized PSF is correlated with the data in a test window using the CD scheme and the hypothesis which results in the highest SNR value is most likely the case being observed. The three hypotheses explored in this text are 1) the null hypothesis that a space object has not been detected in a given frame of data (H_0), 2) the hypothesis that an object has been detected in a given frame of data and that object is a NEO (H_1) and 3) the hypothesis that an object has been detected in a given frame of data and that object is a stellar object (H_2). The above SNR computation would be feasible to determine which of these hypotheses were most valid given an observed data frame if the tilt aberrations were observable using a single telescope. However, the parallax effect is not pronounced with only one telescope pointed straight at a NEO due to the phase appearing to be flat across a limited size aperture. A method will be devised using a system of two telescopes, geometric optics and the non-paraxial PSF generation tool.

MHT Derivation for Two Telescopes

To detect the tilt aberrations caused by parallax, a system of two telescopes making simultaneous observations from different locations is utilized. The separation between the two telescopes is henceforward referred to as the baseline difference; with different baselines, the tilt aberrations effect on the parallax sensing telescope should become more apparent and thus, more detectable with a MHT detection scheme. Recall that for NEO's, there will be detectable tilt aberrations and for stellar objects, there will not be detectable tilt aberrations due to the radius of curvature of each respective observation's emanating electromagnetic field. To derive the LRT, the joint probability density function of the two telescopes will be utilized; because the telescopes are geographically separated systems, it is assumed that their independently collected data is also independently distributed. The joint probability density function of two independent random variables becomes the product of the two marginal probability density functions [17].

$$P(d_1(x,y) \bigcap d_2(x,y)) = P(d_1(x,y)) \cdot P(d_2(x,y)) \tag{3.30}$$

Experimentation will utilize data collected from the SST and Naval Observatory astronomical telescopes. The respective PSFs will be properly registered with the Naval Observatory serving as the reference telescope and the SST as the parallax sensing telescope. Per previous research which utilized SST, the data will be assumed to follow a Gaussian distribution [11]. Seen below is the marginal, Gaussian probability density functions, P_{D_1} and P_{D_2}, for the reference and parallax sensing telescopes respectively.

$$P_{D_1}(d_1(x,y)) = \frac{1}{\sqrt{2\pi\sigma_1^2}} e^{-(d_1(x,y)-m_1)^2/2\sigma_1^2} \quad \& \quad P_{D_2}(d_2(x,y)) = \frac{1}{\sqrt{2\pi\sigma_2^2}} e^{-(d_2(x,y)-m_2)^2/2\sigma_2^2} \tag{3.31}$$

where,

$$m_{H_i} = S \cdot h_i(x,y) + B \tag{3.32}$$

$$m_{H_0} = B \tag{3.33}$$

The LRT, Λ, is formed by taking the ratio of the product of these two distributions given the condition that an observation is present in the data, H_1, in the numerator and the condition that an observation is not present the data, H_0, in the denominator. Because the parallax sensing telescope is pointed straight up rather than directly at an observation, tilt aberrations will affect the distribution of its PSF dependent on whether a stellar object or NEO object is being observed. The test PSFs will be defined as $h_{ref}(x,y)$ for the reference PSF, $h_{star}(x,y)$ for stellar observations and as $h_{NEO}(x,y)$ for NEO's. Geometric optics and the non-paraxial PSF generation tool will be used to compute $h_{star}(x,y)$ and $h_{NEO}(x,y)$; the PSF when observing stars will be identical to the reference telescope's PSF, $h_{ref}(x,y)$ due to the absence of significant tilt aberrations. There are now two hypotheses given an observation in a frame of data which are the hypothesis that an object has been detected in a given frame of data and that object is a NEO, (H_1), and the hypothesis that an object has been detected in a given frame of data and that object is a stellar object, (H_2). The null hypothesis, (H_0), is the hypothesis that no object is observed and the frame or pixel only contains background data. There are two distinct LRT's of which $\Lambda_1(frame)$ computes a value under the H_1 hypothesis and $\Lambda_2(frame)$ computes a value under the $H_2(frame)$

hypothesis. Both LRT's are computed for a given frame and the difference between those two LRT's is be taken to determine whether an observation is most likely a star or a NEO.

$$\Lambda_i = \frac{P(d_1(x,y) \cap P(d_2(x,y)) \mid H_i}{P(d_1(x,y) \cap P(d_2(x,y)) \mid H_0} = \frac{\prod_{x=1}^{N}\prod_{y=1}^{N} \frac{1}{\sqrt{2\pi\sigma_1^2}} e^{-(d_1(x,y)-S\cdot h_{ref}(x,y)-B)^2/2\sigma_1^2} \cdot \frac{1}{\sqrt{2\pi\sigma_2^2}} e^{-(d_2(x,y)-S\cdot h_i(x,y)-B)^2/2\sigma_2^2}}{\prod_{x=1}^{N}\prod_{y=1}^{N} \frac{1}{\sqrt{2\pi\sigma_1^2}} e^{-(d_1(x,y)-B)^2/2\sigma_1^2} \cdot \frac{1}{\sqrt{2\pi\sigma_2^2}} e^{-(d_2(x,y)-B)^2/2\sigma_2^2}} \underset{<}{>} 1 \tag{3.34}$$

$$\Lambda_1 = \frac{P(d_1(x,y) \cap P(d_2(x,y)) \mid H_1}{P(d_1(x,y) \cap P(d_2(x,y)) \mid H_0} = \frac{\prod_{x=1}^{N}\prod_{y=1}^{N} \frac{1}{\sqrt{2\pi\sigma_1^2}} e^{-(d_1(x,y)-S\cdot h_{ref}(x,y)-B)^2/2\sigma_1^2} \cdot \frac{1}{\sqrt{2\pi\sigma_2^2}} e^{-(d_2(x,y)-S\cdot h_{NEO}(x,y)-B)^2/2\sigma_2^2}}{\prod_{x=1}^{N}\prod_{y=1}^{N} \frac{1}{\sqrt{2\pi\sigma_1^2}} e^{-(d_1(x,y)-B)^2/2\sigma_1^2} \cdot \frac{1}{\sqrt{2\pi\sigma_2^2}} e^{-(d_2(x,y)-B)^2/2\sigma_2^2}} \underset{<}{>} 1 \tag{3.35}$$

$$\Lambda_2 = \frac{P(d_1(x,y) \cap P(d_2(x,y)) \mid H_2}{P(d_1(x,y) \cap P(d_2(x,y)) \mid H_0} = \frac{\prod_{x=1}^{N}\prod_{y=1}^{N} \frac{1}{\sqrt{2\pi\sigma_1^2}} e^{-(d_1(x,y)-S\cdot h_{ref}(x,y)-B)^2/2\sigma_1^2} \cdot \frac{1}{\sqrt{2\pi\sigma_2^2}} e^{-(d_2(x,y)-S\cdot h_{stellar}(x,y)-B)^2/2\sigma_2^2}}{\prod_{x=1}^{N}\prod_{y=1}^{N} \frac{1}{\sqrt{2\pi\sigma_1^2}} e^{-(d_1(x,y)-B)^2/2\sigma_1^2} \cdot \frac{1}{\sqrt{2\pi\sigma_2^2}} e^{-(d_2(x,y)-B)^2/2\sigma_2^2}} \underset{<}{>} 1 \tag{3.36}$$

Before the MHT algorithm is simplified, it is important to note that this detection scheme will work for systems of astronomical telescopes with the same or different telescopes. This is useful because the USAF SSN consists of a variety of astronomical telescope assets and the experiment will utilize simultaneous data taken from differing telescope systems. The simulations will be run for both a system of identical telescopes and the experiment will be with a system of different telescopes.

CD MHT with Identical Telescopes

Additional simplifications are made possible by using the same telescope system for the reference and parallax sensing telescopes. First, the LRT for an optical system using the same telescopes for the reference and parallax sensing telescope will be derived. The first step is to take the natural log of both sides of the expression which changes the products to sums and allows for several cancellations of terms.

$$\ln(\Lambda_i) = \ln\left(\frac{\prod_{x=1}^{N}\prod_{y=1}^{N}\frac{1}{\sqrt{2\pi\sigma_1^2}}e^{-(d_1(x,y)-S\cdot h_{ref}(x,y)-B)^2/2\sigma_1^2}\cdot\frac{1}{\sqrt{2\pi\sigma_2^2}}e^{-(d_2(x,y)-S\cdot h_i(x,y)-B)^2/2\sigma_2^2}}{\prod_{x=1}^{N}\prod_{y=1}^{N}\frac{1}{\sqrt{2\pi\sigma_1^2}}e^{-(d_1(x,y)-B)^2/2\sigma_1^2}\cdot\frac{1}{\sqrt{2\pi\sigma_2^2}}e^{-(d_2(x,y)-B)^2/2\sigma_2^2}}\right) \underset{<}{>} \ln(1) \quad (3.37)$$

$$\sum_{x=1}^{N}\sum_{y=1}^{N} -\frac{1}{2\sigma_1^2}(d_1(x,y)-S\cdot h_{ref}(x,y)-B)^2 - \frac{1}{2\sigma_2^2}(d_2(x,y)-S\cdot h_i(x,y)-B)^2 + \frac{1}{2\sigma_1^2}(d_1(x,y)-B)^2 + \frac{1}{2\sigma_2^2}(d_2(x,y)-B)^2 \underset{<}{>} 0 \quad (3.38)$$

If both optical systems are the same, they could have nearly the same standard deviation and signal intensity on the CDD array which would simplify the expression into a more manageable form. This would only be valid when S_1 and S_2 as well as σ_1 and σ_2 can be approximated as equivalent to each other.

$$\sum_{x=1}^{N}\sum_{y=1}^{N}\frac{1}{2\sigma^2}\begin{bmatrix} -(\cancel{d_1^2(x,y)} + S^2\cdot h_{ref}^2(x,y) + \cancel{B_1^2} - \cancel{2\cdot d_1(x,y)\cdot B_1} - 2\cdot d_1(x,y)\cdot S\cdot h_{ref}(x,y) - 2\cdot S\cdot h_{ref}(x,y)\cdot B_1)... \\ ...-(\cancel{d_2^2(x,y)} + S^2\cdot h_i^2(x,y) + \cancel{B_2^2} - \cancel{2\cdot d_2(x,y)\cdot B_2} - 2\cdot d_2(x,y)\cdot S\cdot h_{ref}(x,y) - 2\cdot S\cdot h_{ref}(x,y)\cdot B_2)... \\ ...+(\cancel{d_1(x,y)} - \cancel{2\cdot B_1\cdot d_1(x,y)} - \cancel{B_1^2}) + (\cancel{d_2^2(x,y)} - \cancel{2\cdot B_2\cdot d_2(x,y)} + \cancel{B_2^2}) \end{bmatrix} \underset{<}{>} 0 \quad (3.39)$$

$$\sum_{x=1}^{N}\sum_{y=1}^{N}\frac{1}{2\sigma^2}\left[2\cdot d_1(x,y)\cdot S\cdot h_{ref}(x,y) - 2\cdot S\cdot h_{ref}(x,y)\cdot B_1 - S^2\cdot h_{ref}^2(x,y)\right] + \sum_{x=1}^{N}\sum_{y=1}^{N}\frac{1}{2\sigma^2}\left[2\cdot d_2(x,y)\cdot S\cdot h_{ref}(x,y) - 2\cdot S\cdot h_{ref}(x,y)\cdot B_2 - S^2\cdot h_i^2(x,y))\right] \underset{<}{>} 0 \quad (3.40)$$

As with the CD test, the expression which is reliant on the signal strength and PSF only is moved to the right-hand side of the expression and the intensity, S, can be factored out of the both sides and divided out of the left-hand side.

$$\frac{\sum_{x=1}^{N}\sum_{y=1}^{N}(S\cdot h_{ref}(x,y)\cdot 2(d_1(x,y)-B_1) + \sum_{x=1}^{N}\sum_{y=1}^{N}(S\cdot h_i(x,y)\cdot 2(d_2(x,y)-B_2)}{\cancel{2\sigma^2}} \underset{<}{>} \frac{\sum_{x=1}^{N}\sum_{y=1}^{N}S^2\cdot h_{ref}^2(x,y) + \sum_{x=1}^{N}\sum_{y=1}^{N}S^2\cdot h_i^2(x,y)}{\cancel{2\sigma^2}} \quad (3.41)$$

$$\cancel{2}S\cdot\left[\sum_{x=1}^{N}\sum_{y=1}^{N}(h_{ref}(x,y)\cdot(d_1(x,y)-B_1) + \sum_{x=1}^{N}\sum_{y=1}^{N}(h_i(x,y)\cdot(d_2(x,y)-B_2)\right] \underset{<}{>} S^{\cancel{2}}\cdot\left[\sum_{x=1}^{N}\sum_{y=1}^{N}h_{ref}^2(x,y) + \sum_{x=1}^{N}\sum_{y=1}^{N}h_i^2(x,y)\right] \quad (3.42)$$

This results in an expression for the LRT which is the correlation of the data observed by the reference telescope, $d_1(x,y)$, with the reference telescope PSF, $h_{ref}(x,y)$, added to the correlation of the data observed by the parallax sensing telescope, $d_2(x,y)$, with the PSF of the parallax sensing telescope PSF, $h_i(x,y)$.

$$\Lambda_{i=}\left[\sum_{x=1}^{N}\sum_{y=1}^{N}(h_{ref}(x,y)\cdot(d_1(x,y)-B_1)+\sum_{x=1}^{N}\sum_{y=1}^{N}(h_i(x,y)\cdot(d_2(x,y)-B_2)\right]\gtrless\frac{S\cdot\left[\sum_{x=1}^{N}\sum_{y=1}^{N}h_{ref}{}^2(x,y)+\sum_{x=1}^{N}\sum_{y=1}^{N}h_i{}^2(x,y)\right]}{2}=\gamma \quad (3.43)$$

$$\Lambda_{1=}\left[\sum_{x=1}^{N}\sum_{y=1}^{N}(h_{ref}(x,y)\cdot(d_1(x,y)-B_1)+\sum_{x=1}^{N}\sum_{y=1}^{N}(h_{NEO}(x,y)\cdot(d_2(x,y)-B_2)\right]\gtrless\frac{S\cdot\left[\sum_{x=1}^{N}\sum_{y=1}^{N}h_{ref}{}^2(x,y)+\sum_{x=1}^{N}\sum_{y=1}^{N}h_{NEO}{}^2(x,y)\right]}{2}=\gamma \quad (3.44)$$

$$\Lambda_{2=}\left[\sum_{x=1}^{N}\sum_{y=1}^{N}(h_{ref}(x,y)\cdot(d_1(x,y)-B_1)+\sum_{x=1}^{N}\sum_{y=1}^{N}(h_{star}(x,y)\cdot(d_2(x,y)-B_2)\right]\gtrless\frac{S\cdot\left[\sum_{x=1}^{N}\sum_{y=1}^{N}h_{ref}{}^2(x,y)+\sum_{x=1}^{N}\sum_{y=1}^{N}h_{star}{}^2(x,y)\right]}{2}=\gamma \quad (3.45)$$

Given an observed frame of data, the presence of a target can be distinguished, and the detected object can be categorized as either a NEO or stellar object.

Table 1: Categorization of Observations with LRT's

MHT Conditions	Categorization
$\Lambda_1 > \gamma$ and $\Lambda_1 > \Lambda_2$	Target present is a NEO
$\Lambda_2 > \gamma$ and $\Lambda_2 > \Lambda_1$	Target present is a stellar object
$\Lambda_1 < \gamma$ and $\Lambda_2 < \gamma$	No target is present

The expected value of the Λ squared, $E[\Lambda^2]$, can be computed to find the variance of the sum of the two correlations, σ_Λ^2. Using this variance, Λ, can be made into a SNR relationship by dividing it by the square root of the variance, the standard deviation of the expression.

$$E[\Lambda^2] = E\left[\left(\sum_{x_1=1}^{N}\sum_{y_1=1}^{N}(h_{ref}(x_1,y_1)\cdot(d_1(x_1,y_1)-B_1)+\sum_{x_2=1}^{N}\sum_{y_2=1}^{N}(h_i(x_2,y_2)\cdot(d_2(x_2,y_2)-B_2)\right)^2\right] \quad (3.46)$$

$$E[\Lambda^2] = E\left[\begin{array}{l}\sum_{x_1=1}^{N}\sum_{y_1=1}^{N}(h_{ref}(x_1,y_1)\cdot(d_1(x_1,y_1)-B_1)\sum_{x_2=1}^{N}\sum_{y_2=1}^{N}(h_{ref}(x_2,y_2)\cdot(d_1(x_2,y_2)-B_1)+ \\ ...\sum_{x_3=1}^{N}\sum_{y_3=1}^{N}(h_i(x_3,y_3)\cdot(d_2(x_3,y_3)-B_2)\sum_{x_4=1}^{N}\sum_{y_4=1}^{N}(h_i(x_4,y_4)\cdot(d_2(x_4,y_4)-B_2)+ \\ ...2\sum_{x_5=1}^{N}\sum_{y_5=1}^{N}(h_{ref}(x_5,y_5)\cdot(d_1(x_5,y_5)-B_1)\sum_{x_6=1}^{N}\sum_{y_6=1}^{N}(h_i(x_6,y_6)\cdot(d_2(x_6,y_6)-B_2)\end{array}\right] \quad (3.47)$$

Equation (3.47) is almost the same expression as the one which resulted for the derivation of the CD SNR expression but with the addition of a cross-term between the reference and parallax telescopes. The expectation operator distributes to each of the terms in the brackets and as before.

$$\begin{aligned}E[\Lambda^2] = &\sum_{x_1=1}^{N}\sum_{y_1=1}^{N}\sum_{x_2=1}^{N}\sum_{y_2=1}^{N}h_{ref}(x_1,y_1)\cdot h_{ref}(x_2,y_2)\cdot E\left[(d_1(x_1,y_1)-B_1)\cdot(d_1(x_2,y_2)-B_1)\right]+ \\ &...\sum_{x_3=1}^{N}\sum_{y_3=1}^{N}\sum_{x_4=1}^{N}\sum_{y_4=1}^{N}h_i(x_3,y_3)\cdot h_i(x_4,y_4)\cdot E\left[(d_2(x_3,y_3)-B_2)\cdot(d_2(x_4,y_4)-B_2)\right]+ \\ &...2\sum_{x_5=1}^{N}\sum_{y_5=1}^{N}\sum_{x_6=1}^{N}\sum_{y_6=1}^{N}(h_{ref}(x_5,y_5)\cdot h_i(x_6,y_6)\cdot E\left[(d_1(x_5,y_5)-B_1)(d_2(x_6,y_6)-B_2)\right]\end{aligned} \quad (3.48)$$

Again, there are two cases for each of the above quadruple sums, one where the terms in the sum are equal, $x_i = x_j$ and $y_i = y_j$, and one where they are all different, $x_i \neq x_j$ and $y_i \neq y_j$. Depending on the luminosity of the target, the distribution of the variance of the data depends on which noise source dominates. The noise can either be dominated by random photon arrivals and follow a Poisson distribution or it can be dominated by readout noise and take on a Gaussian distribution. For the SST, the background noise will be dominated by CCD readout noise which is Gaussian [10]. SSN sensors are configured to

operate at set P_{FA} values, and for this reason, the null hypothesis, H_0, is used to find the variance of the LRT so that thresholds can be set to achieve a desired P_{FA}. This is later shown in Equation (3.69).

$$\begin{aligned}
E[\Lambda^2_{H_0}]_{x_1\neq x_2 \& y_1\neq y_2} + \; &= \sum_{x_1=1}^{N}\sum_{y_1=1}^{N}\sum_{x_2=1}^{N}\sum_{y_2=1}^{N}(1-\delta(x_1-x_2,y_1-y_2))\cdot h_{ref}(x_1,y_1)\cdot h_{ref}(x_2,y_2)\cdot \underline{E[d_1(x_1,y_1)-B_1]}^{=0}\cdot \underline{E[d_1(x_2,y_2)-B_1]}^{=0} + \\
...E[\Lambda^2_{H_0}]_{x_1=x_2 \& y_1=y_2} \quad &...\sum_{x_3=1}^{N}\sum_{y_3=1}^{N}\sum_{x_4=1}^{N}\sum_{y_4=1}^{N}(1-\delta(x_1-x_2,y_1-y_2))\cdot h_i(x_3,y_3)\cdot h_i(x_4,y_4)\cdot \underline{E[d_2(x_3,y_3)-B_2]}^{=0}\cdot \underline{E[d_2(x_4,y_4)-B_2]}^{=0} + \\
&...2\sum_{x_5=1}^{N}\sum_{y_5=1}^{N}\sum_{x_6=1}^{N}\sum_{y_6=1}^{N}(1-\delta(x_1-x_2,y_1-y_2))\cdot(h_{ref}(x_5,y_5)\cdot h_i(x_6,y_6)\cdot \underline{E[d_1(x_5,y_5)-B_1]}^{=0}\cdot \underline{E[d_2(x_6,y_6)-B_2]}^{=0} + \\
&...\sum_{x_1=1}^{N}\sum_{y_1=1}^{N}\sum_{x_2=1}^{N}\sum_{y_2=1}^{N}\delta(x_1-x_2,y_1-y_2)\cdot h_{ref}(x_1,y_1)\cdot h_{ref}(x_1,y_1)\cdot E\left[(d_1(x_1,y_1)-B_1)^2\right] + \\
&...\sum_{x_3=1}^{N}\sum_{y_3=1}^{N}\sum_{x_4=1}^{N}\sum_{y_4=1}^{N}\delta(x_3-x_4,y_3-y_4)\cdot h_i(x_3,y_3)\cdot h_i(x_3,y_3)\cdot E\left[(d_2(x_3,y_3)-B_2)^2\right] + \\
&...2\sum_{x_5=1}^{N}\sum_{y_5=1}^{N}\sum_{x_6=1}^{N}\sum_{y_6=1}^{N}\delta(x_5-x_6,y_5-y_6)\cdot(h_{ref}(x_5,y_5)\cdot h_i(x_5,y_5)\cdot \underline{E[(d_1(x_5,y_5)-B_1)]}^{=0}\cdot \underline{E[(d_2(x_5,y_5)-B_2]}^{=0}
\end{aligned} \tag{3.49}$$

Every pixel in the data frame is statistically independent from all the others when the terms in the summation are not the same, $x_i \neq x_j$ and $y_i \neq y_j$. The quantity $d_i(x_i,y_i)-B_i$ is a zero-mean Gaussian random number; thus, the expected value of this quantity, $E[d_i(x_i,y_i)-B_i]$, is zero and all such terms are eliminated. Also noting that the expected value of this quantity squared, $E\left[\left(d_i(x_i,y_i)-B_i\right)^2\right]$, is the variance of the frame, the expression is further reduced. If the reference and parallax sensing telescopes are the same or very close, the standard deviation of the LRT factors out of the expression as seen in (3.52). Otherwise, the expression for the SNR would utilize (3.51) for the variance.

$$\sigma^2_\Lambda = E[\Lambda^2]_{x_1\neq x_2 \& y_1\neq y_2} + E[\Lambda^2]_{x_1=x_2 \& y_1=y_2} = \sigma_1^2\cdot\sum_{x_1=1}^{N}\sum_{y_1=1}^{N}h^2_{ref}(x_1,y_1) + \sigma_2^2\cdot\sum_{x_3=1}^{N}\sum_{y_3=1}^{N}h_i^2(x_3,y_3) \tag{3.50}$$

$$\sigma_\Lambda = \sqrt{\sigma_1^2\cdot\sum_{x_1=1}^{N}\sum_{y_1=1}^{N}h^2_{ref}(x_1,y_1) + \sigma_2^2\cdot\sum_{x_3=1}^{N}\sum_{y_3=1}^{N}h_i^2(x_3,y_3)} \tag{3.51}$$

$$\sigma_\Lambda = \sigma\sqrt{\cdot\sum_{x_1=1}^{N}\sum_{y_1=1}^{N}h^2_{ref}(x_1,y_1) + \sum_{x_3=1}^{N}\sum_{y_3=1}^{N}h_i^2(x_3,y_3)} \tag{3.52}$$

(3.43)-(3.45) are divided by the (3.51) or (3.52) to come up with an algorithm analogous to SNR for an optical system consisting of two identical telescopes. By dividing the LRT by its standard deviation, it becomes a unit-normal Gaussian random number. This new correlation based MHT detection method can determine if an observation is a NEO or a stellar object given that an object has been detected. As seen below, the content of the data in each observed frame will be categorized based on which SNR computation produces the highest number.

$$SNR_i = \frac{\left[\sum_{x=1}^{N}\sum_{y=1}^{N}(h_{ref}(x,y)\cdot(d_1(x,y)-B_1)+\sum_{x=1}^{N}\sum_{y=1}^{N}(h_i(x,y)\cdot(d_2(x,y)-B_2)\right]}{\sigma\sqrt{\cdot\sum_{x_1=1}^{N}\sum_{y_1=1}^{N}h_{ref}^2(x_1,y_1)+\sum_{x_3=1}^{N}\sum_{y_3=1}^{N}h_i^2(x_3,y_3)}} \underset{<}{>} \frac{\frac{S}{2}\cdot\left[\sum_{x=1}^{N}\sum_{y=1}^{N}h_{ref}{}^2(x,y)+\sum_{x=1}^{N}\sum_{y=1}^{N}h_i{}^2(x,y)\right]}{\sigma\sqrt{\cdot\sum_{x_1=1}^{N}\sum_{y_1=1}^{N}h_{ref}^2(x_1,y_1)+\sum_{x_3=1}^{N}\sum_{y_3=1}^{N}h_i^2(x_3,y_3)}} = \gamma \tag{3.53}$$

$$SNR_{NEO} = \frac{\left[\sum_{x=1}^{N}\sum_{y=1}^{N}(h_{ref}(x,y)\cdot(d_1(x,y)-B_1)+\sum_{x=1}^{N}\sum_{y=1}^{N}(h_{NEO}(x,y)\cdot(d_2(x,y)-B_2)\right]}{\sigma\sqrt{\sum_{x_1=1}^{N}\sum_{y_1=1}^{N}h_{ref}^2(x_1,y_1)+\sum_{x_3=1}^{N}\sum_{y_3=1}^{N}h_{NEO}^2(x_3,y_3)}} \underset{<}{>} \frac{\frac{S}{2}\cdot\left[\sum_{x=1}^{N}\sum_{y=1}^{N}h_{ref}{}^2(x,y)+\sum_{x=1}^{N}\sum_{y=1}^{N}h_{NEO}{}^2(x,y)\right]}{\sigma\sqrt{\sum_{x_1=1}^{N}\sum_{y_1=1}^{N}h_{ref}^2(x_1,y_1)+\sum_{x_3=1}^{N}\sum_{y_3=1}^{N}h_{NEO}^2(x_3,y_3)}} = \gamma \tag{3.54}$$

$$SNR_{star} = \frac{\left[\sum_{x=1}^{N}\sum_{y=1}^{N}(h_{ref}(x,y)\cdot(d_1(x,y)-B_1)+\sum_{x=1}^{N}\sum_{y=1}^{N}(h_{star}(x,y)\cdot(d_2(x,y)-B_2)\right]}{\sigma\sqrt{\cdot\sum_{x_1=1}^{N}\sum_{y_1=1}^{N}h_{ref}^2(x_1,y_1)+\sum_{x_3=1}^{N}\sum_{y_3=1}^{N}h_{star}^2(x_3,y_3)}} \underset{<}{>} \frac{\frac{S}{2}\cdot\left[\sum_{x=1}^{N}\sum_{y=1}^{N}h_{ref}{}^2(x,y)+\sum_{x=1}^{N}\sum_{y=1}^{N}h_{star}{}^2(x,y)\right]}{\sigma\sqrt{\cdot\sum_{x_1=1}^{N}\sum_{y_1=1}^{N}h_{ref}^2(x_1,y_1)+\sum_{x_3=1}^{N}\sum_{y_3=1}^{N}h_{star}^2(x_3,y_3)}} = \gamma \tag{3.55}$$

Having a CD MHT detector that does not depend on the target's irradiance is an advantage, because SNR thresholds, γ, can be selected to achieve a desired false alarm probability, P_{FA}. This is convenient because current SSN sensors are configured to achieve desired P_{FA} values. Thus, the proposed CD MHT detection algorithm is ideal for a new SSN system consisting of identical telescopes. This thesis will look at objects in Geosynchronous orbit, but (3.53) may be used to detect any object which appears on the CCD as a point source and not a streak requiring that the telescope track the object of interest or that the CCD exposure time is short enough.

CD MHT with Different Telescopes

Although the CD MHT detector using parallax is best for a system of identical sensors, it will also work when fusing data from a network of varied sensors. Currently, the USAF's SSN is composed of only different optical sensors and due to the unique data processing approaches, CCD designs and aperture dimensions, the intensity of the signal detected from an observed space object, S, and the standard deviation of the data read out by the CCD detector will be different. In the derivation for the new algorithm, the standard deviation and object intensity were factored out to remove dependence on object signal strength from the algorithm in (3.15). The algorithm is easily re-written for a system of different optical sensors (3.25).

$$\Lambda_i = \left[S_1 \cdot \sum_{x=1}^{N}\sum_{y=1}^{N} (h_{ref}(x,y) \cdot \frac{(d_1(x,y) - B_1)}{\sigma_1} + S_2 \cdot \sum_{x=1}^{N}\sum_{y=1}^{N} (h_i(x,y) \cdot \frac{(d_2(x,y) - B_2)}{\sigma_2} \right] \underset{<}{>} \frac{\left[\frac{S_1^2}{\sigma_1} \cdot \sum_{x=1}^{N}\sum_{y=1}^{N} {h_{ref}}^2(x,y) + \frac{S_2^2}{\sigma_2} \cdot \sum_{x=1}^{N}\sum_{y=1}^{N} {h_i}^2(x,y) \right]}{2} = \gamma \quad (3.56)$$

$$\Lambda_1 = \left[S_1 \cdot \sum_{x=1}^{N}\sum_{y=1}^{N} (h_{ref}(x,y) \cdot \frac{(d_1(x,y) - B_1)}{\sigma_1} + S_2 \cdot \sum_{x=1}^{N}\sum_{y=1}^{N} (h_{NEO}(x,y) \cdot \frac{(d_2(x,y) - B_2)}{\sigma_2} \right] \underset{<}{>} \frac{\left[\frac{S_1^2}{\sigma_1} \cdot \sum_{x=1}^{N}\sum_{y=1}^{N} {h_{ref}}^2(x,y) + \frac{S_2^2}{\sigma_2} \cdot \sum_{x=1}^{N}\sum_{y=1}^{N} {h_{NEO}}^2(x,y) \right]}{2} = \gamma \quad (3.57)$$

$$\Lambda_2 = \left[S_1 \cdot \sum_{x=1}^{N}\sum_{y=1}^{N} (h_{ref}(x,y) \cdot \frac{(d_1(x,y) - B_1)}{\sigma_1} + S_2 \cdot \sum_{x=1}^{N}\sum_{y=1}^{N} (h_{star}(x,y) \cdot \frac{(d_2(x,y) - B_2)}{\sigma_2} \right] \underset{<}{>} \frac{\left[\frac{S_1^2}{\sigma_1} \cdot \sum_{x=1}^{N}\sum_{y=1}^{N} {h_{ref}}^2(x,y) + \frac{S_2^2}{\sigma_2} \cdot \sum_{x=1}^{N}\sum_{y=1}^{N} {h_{star}}^2(x,y) \right]}{2} = \gamma \quad (3.58)$$

(3.56)-(3.58) have dependence on the object intensity in the left-hand side of the expression; one way to mitigate this is to compute the observed object's irradiance from each of the two data sets and divide both sides by either S_1 or S_2 so that there is only a ratio of the intensities; in Equations (3.59) and (3.60), the former was chosen.

$$\frac{\left[S_1 \cdot \sum_{x=1}^{N}\sum_{y=1}^{N} (h_{ref}(x,y) \cdot \frac{(d_1(x,y) - B_1)}{\sigma_1} + S_2 \cdot \sum_{x=1}^{N}\sum_{y=1}^{N} (h_i(x,y) \cdot \frac{(d_2(x,y) - B_2)}{\sigma_2} \right]}{S_1} \underset{<}{>} \frac{\left[\frac{S_1^2}{\sigma_1} \cdot \sum_{x=1}^{N}\sum_{y=1}^{N} {h_{ref}}^2(x,y) + \frac{S_2^2}{\sigma_2} \cdot \sum_{x=1}^{N}\sum_{y=1}^{N} {h_i}^2(x,y) \right]}{S_1 \cdot 2} \quad (3.59)$$

$$\left[\sum_{x=1}^{N}\sum_{y=1}^{N} (h_{ref}(x,y) \cdot \frac{(d_1(x,y) - B_1)}{\sigma_1} + \frac{S_2}{S_1} \cdot \sum_{x=1}^{N}\sum_{y=1}^{N} (h_i(x,y) \cdot \frac{(d_2(x,y) - B_2)}{\sigma_2} \right] \underset{<}{>} \frac{1}{2} \left[\frac{S_1}{\sigma_1} \cdot \sum_{x=1}^{N}\sum_{y=1}^{N} {h_{ref}}^2(x,y) + \frac{S_2}{\sigma_2} \frac{S_2}{S_1} \cdot \sum_{x=1}^{N}\sum_{y=1}^{N} {h_i}^2(x,y) \right] \quad (3.60)$$

The SNR expression also changes when a system of two different optical sensors is being used due to the dependence on the object intensity and data frame standard deviation.

$$E[\Lambda_{H_0}^2] = \sum_{x_1=1}^{N}\sum_{y_1=1}^{N}\sum_{x_2=1}^{N}\sum_{y_2=1}^{N} h_{ref}(x_1,y_1)\cdot h_{ref}(x_2,y_2)\cdot S_1^2 \frac{E\left[(d_1(x_1,y_1)-B_1)\cdot(d_1(x_2,y_2)-B_1)\right]}{\sigma_1^2} + \\ \ldots\sum_{x_3=1}^{N}\sum_{y_3=1}^{N}\sum_{x_4=1}^{N}\sum_{y_4=1}^{N} h_i(x_3,y_3)\cdot h_i(x_4,y_4)\cdot S_2^2 \frac{E\left[(d_2(x_3,y_3)-B_2)\cdot(d_2(x_4,y_4)-B_2)\right]}{\sigma_1^2} + \\ \ldots 2\sum_{x_5=1}^{N}\sum_{y_5=1}^{N}\sum_{x_6=1}^{N}\sum_{y_6=1}^{N} (h_{ref}(x_5,y_5)\cdot h_i(x_6,y_6)\cdot S_1\cdot S_2 \frac{E\left[(d_1(x_5,y_5)-B_1)(d_2(x_6,y_6)-B_2)\right]}{\sigma_1\sigma_2} \tag{3.61}$$

Again, there are two cases for each of the above quadruple sums, one where the terms in the sum are equal, $x_i = x_j$ and $y_i = y_j$, and one where they are all different, $x_i \neq x_j$ and $y_i \neq y_j$. Using the same argument as before, the expectation of the $d_i(x_i,y_i) - B_i$ terms goes to zero because the pixels are independently distributed with the indexes aren't equivalent in the sum. Frames of data from two different telescopes are always independent data sets and this term, likewise, $d_i(x_i,y_i) - B_i$ has an expectation of zero.

$$E[\Lambda_{H_0}^2]_{x_1\neq x_2 \,\&\, y_1\neq y_2} + \ldots E[\Lambda_{H_0}^2]_{x_1=x_2 \,\&\, y_1=y_2} = \\ \sum_{x_1=1}^{N}\sum_{y_1=1}^{N}\sum_{x_2=1}^{N}\sum_{y_2=1}^{N}(1-\delta(x_1-x_2,y_1-y_2))\cdot h_{ref}(x_1,y_1)\cdot h_{ref}(x_2,y_2)\cdot\frac{S_1^2}{\sigma_1^2}\cdot \cancelto{=0}{E[d_1(x_1,y_1)-B_1]}\cdot \cancelto{=0}{E[d_1(x_2,y_2)-B_1]} + \\ \ldots\sum_{x_3=1}^{N}\sum_{y_3=1}^{N}\sum_{x_4=1}^{N}\sum_{y_4=1}^{N}(1-\delta(x_1-x_2,y_1-y_2))\cdot h_i(x_3,y_3)\cdot h_i(x_4,y_4)\cdot\frac{S_2^2}{\sigma_2^2}\cdot \cancelto{=0}{E[d_2(x_3,y_3)-B_2]}\cdot \cancelto{=0}{E[d_2(x_4,y_4)-B_2]} + \\ \ldots 2\sum_{x_5=1}^{N}\sum_{y_5=1}^{N}\sum_{x_6=1}^{N}\sum_{y_6=1}^{N}(1-\delta(x_1-x_2,y_1-y_2))\cdot(h_{ref}(x_5,y_5)\cdot h_i(x_6,y_6)\cdot\frac{S_1\cdot S_2}{\sigma_1\sigma_2}\cdot \cancelto{=0}{E[d_1(x_5,y_5)-B_1]}\cdot \cancelto{=0}{E[d_2(x_6,y_6)-B_2]} + \\ \ldots\sum_{x_1=1}^{N}\sum_{y_1=1}^{N}\sum_{x_2=1}^{N}\sum_{y_2=1}^{N}\delta(x_1-x_2,y_1-y_2)\cdot h_{ref}(x_1,y_1)\cdot h_{ref}(x_1,y_1)\cdot\frac{S_1^2}{\sigma_1^2}\cdot E\left[(d_1(x_1,y_1)-B_1)^2\right] + \\ \ldots\sum_{x_3=1}^{N}\sum_{y_3=1}^{N}\sum_{x_4=1}^{N}\sum_{y_4=1}^{N}\delta(x_3-x_4,y_3-y_4)\cdot h_i(x_3,y_3)\cdot h_i(x_3,y_3)\cdot\frac{S_2^2}{\sigma_2^2}\cdot E\left[(d_2(x_3,y_3)-B_2)^2\right] + \\ \ldots 2\sum_{x_5=1}^{N}\sum_{y_5=1}^{N}\sum_{x_6=1}^{N}\sum_{y_6=1}^{N}\delta(x_5-x_6,y_5-y_6)\cdot(h_{ref}(x_5,y_5)\cdot h_i(x_5,y_5)\cdot\frac{S_1\cdot S_2}{\sigma_1\sigma_2}\cdot \cancelto{=0}{E[(d_1(x_5,y_5)-B_1)]}\cdot \cancelto{=0}{E[(d_2(x_5,y_5)-B_2]} \tag{3.62}$$

It is interesting that the reduced expression for the variance depends on the object's intensity, S, rather than the variance of the respective data frames which suggests that the noise of the system is driven by the sensor with the highest intensity.

$$\sigma_\Lambda^2 = E[\Lambda^2]_{x_1\neq x_2 \,\&\, y_1\neq y_2} + E[\Lambda^2]_{x_1=x_2 \,\&\, y_1=y_2} = \frac{S_1^2}{\cancel{\sigma_1^2}}\cdot\cancel{\sigma_1^2}\cdot\sum_{x_1=1}^{N}\sum_{y_1=1}^{N}h_{ref}^2(x_1,y_1) + \frac{S_2^2}{\cancel{\sigma_2^2}}\cdot\cancel{\sigma_2^2}\cdot\sum_{x_3=1}^{N}\sum_{y_3=1}^{N}h_i^2(x_3,y_3) \tag{3.63}$$

$$\sigma_\Lambda = \sqrt{S_1^2\cdot\sum_{x_1=1}^{N}\sum_{y_1=1}^{N}h_{ref}^2(x_1,y_1) + S_2^2\cdot\sum_{x_3=1}^{N}\sum_{y_3=1}^{N}h_i^2(x_3,y_3)} \tag{3.64}$$

Equations (3.65)-(3.67) are difficult to reduce further and γ cannot be chosen based on statistical tables to achieve desired P_{FA}. Even so, the algorithm can still be used to distinguish if an observed is a NEO or stellar object. This configuration also entails the necessity of additional computations to determine the signal intensity of an observation.

$$SNR_i = \frac{\left[\sum_{x=1}^{N}\sum_{y=1}^{N}(h_{ref}(x,y)\cdot S_1\cdot(d_1(x,y)-B_1)+\sum_{x=1}^{N}\sum_{y=1}^{N}(h_i(x,y)\cdot S_2\cdot(d_2(x,y)-B_2)\right]}{\sqrt{S_1^2\cdot\sum_{x_1=1}^{N}\sum_{y_1=1}^{N}h_{ref}^2(x_1,y_1)+S_2^2\cdot\sum_{x_3=1}^{N}\sum_{y_3=1}^{N}h_i^2(x_3,y_3)}} \underset{<}{>} \frac{\frac{1}{2}\cdot\left[S_1^2\cdot\sum_{x=1}^{N}\sum_{y=1}^{N}h_{ref}{}^2(x,y)+S_2^2\cdot\sum_{x=1}^{N}\sum_{y=1}^{N}h_i{}^2(x,y)\right]}{\sqrt{S_1^2\cdot\sum_{x_1=1}^{N}\sum_{y_1=1}^{N}h_{ref}^2(x_1,y_1)+S_2^2\cdot\sum_{x_3=1}^{N}\sum_{y_3=1}^{N}h_i^2(x_3,y_3)}} = \gamma \tag{3.65}$$

$$SNR_{NEO} = \frac{\left[\sum_{x=1}^{N}\sum_{y=1}^{N}(h_{ref}(x,y)\cdot S_1\cdot(d_1(x,y)-B_1)+\sum_{x=1}^{N}\sum_{y=1}^{N}(h_{NEO}(x,y)\cdot S_2\cdot(d_2(x,y)-B_2)\right]}{\sqrt{S_1^2\cdot\sum_{x_1=1}^{N}\sum_{y_1=1}^{N}h_{ref}^2(x_1,y_1)+S_2^2\cdot\sum_{x_3=1}^{N}\sum_{y_3=1}^{N}h_{NEO}^2(x_3,y_3)}} \underset{<}{>} \frac{\frac{1}{2}\cdot\left[S_1^2\cdot\sum_{x=1}^{N}\sum_{y=1}^{N}h_{ref}{}^2(x,y)+S_2^2\cdot\sum_{x=1}^{N}\sum_{y=1}^{N}h_{NEO}{}^2(x,y)\right]}{\sqrt{S_1^2\cdot\sum_{x_1=1}^{N}\sum_{y_1=1}^{N}h_{ref}^2(x_1,y_1)+S_2^2\cdot\sum_{x_3=1}^{N}\sum_{y_3=1}^{N}h_{NEO}^2(x_3,y_3)}} = \gamma \tag{3.66}$$

$$SNR_{stellar} = \frac{\left[\sum_{x=1}^{N}\sum_{y=1}^{N}(h_{ref}(x,y)\cdot S_1\cdot(d_1(x,y)-B_1)+\sum_{x=1}^{N}\sum_{y=1}^{N}(h_{stellar}(x,y)\cdot S_2\cdot(d_2(x,y)-B_2)\right]}{\sqrt{S_1^2\cdot\sum_{x_1=1}^{N}\sum_{y_1=1}^{N}h_{ref}^2(x_1,y_1)+S_2^2\cdot\sum_{x_3=1}^{N}\sum_{y_3=1}^{N}h_{stellar}^2(x_3,y_3)}} \underset{<}{>} \frac{\frac{1}{2}\cdot\left[S_1^2\cdot\sum_{x=1}^{N}\sum_{y=1}^{N}h_{ref}{}^2(x,y)+S_2^2\cdot\sum_{x=1}^{N}\sum_{y=1}^{N}h_{stellar}{}^2(x,y)\right]}{\sqrt{S_1^2\cdot\sum_{x_1=1}^{N}\sum_{y_1=1}^{N}h_{ref}^2(x_1,y_1)+S_2^2\cdot\sum_{x_3=1}^{N}\sum_{y_3=1}^{N}h_{stellar}^2(x_3,y_3)}} = \gamma \tag{3.67}$$

Performance Metrics

The objective of the CD MHT algorithm is to detect if an object is present in a given frame of data and to correctly distinguish whether that detection is that of a satellite or a star. The three hypotheses are 1) the null hypothesis that a space object has not been detected in a given frame of data (H_0), 2) the hypothesis that an object has been detected in a given frame of data and that object is a NEO (H_1) and 3) the hypothesis that an object has been detected in a given frame of data and that object is a stellar object (H_2). Each of these hypotheses are defined using the statistical distribution which the data is expected to take in each of the three scenarios. The two LRT's, $\Lambda_1(frame)$ and $\Lambda_2(frame)$, are computed by taking the ratio of H_1 and H_2 with H_0 respectively. Performance of the CD MHT

algorithm is quantified by probabilities which arise from the statistical distribution of the data sets. Using probability, the performance of the algorithm can be quantified. There are five probabilities of interest which include the probability of detection, P_D, the probability of false alarm, P_{FA}, the probability of satellite detection, $P_{D_{NEO}}$, the probability of incorrectly detecting a star when a satellite is in the data, $P_{ID_{star}}$, and the probability missing a satellite detection, P_{Miss}. The probability of a detection is that either $\Lambda_1(frame)$ or $\Lambda_2(frame)$ is above the threshold when a target is present. The probability of false alarm is the probability that either $\Lambda_1(frame)$ or $\Lambda_2(frame)$ is above the threshold when no target is present. The probability of satellite detection is the probability that $\Lambda_1(frame)$ is above the threshold and $\Lambda_1(frame)$ is above $\Lambda_2(frame)$ when a satellite observation is present. The probability of incorrectly detecting a star is the probability that $\Lambda_2(frame)$ is above the threshold and $\Lambda_2(frame)$ is above $\Lambda_1(frame)$ when a satellite is in the data. The probability of satellite miss is the probability that $\Lambda_2(frame)$ or $\Lambda_1(frame)$ are below the threshold when an observation is present.

Table 2: Performance Metrics Given Satellite Present

Performance Metrics	Data in Frame	Categorization
$P_D = P\left(\Lambda_1 \bigcup \Lambda_2 > \tau\right) \mid H_1$	Satellite Present	Object Present
$P_{FA} = P\left(\Lambda_1 \bigcup \Lambda_2 > \tau\right) \mid H_0$	Satellite not Present	False Detection of Target
$P_{D_{NEO}} = P\left(\Lambda_1 > \tau \bigcap \Lambda_1 > \Lambda_2\right) \mid H_1$	Satellite Present	Correct Detection of NEO
$P_{ID_{star}} = P(\Lambda_2 > \tau \bigcap \Lambda_2 > \Lambda_1) \mid H_1$	Satellite Present	Incorrect Detection of Star
$P_{Miss} = P\left(\Lambda_1 \bigcap \Lambda_2 < \tau\right) \mid H_1$	Satellite Present	Missed Detection of NEO

The same metrics apply given that a stellar object is in the data being tested. The probability of detection, of false alarm and of a missed detection are the same as before, but the probability of correctly and incorrectly detecting a satellite object or star changes. The probability of stellar object detection, $P_{D_{star}}$, is the probability that $\Lambda_2(frame)$ is above the threshold and $\Lambda_2(frame)$ is above $\Lambda_1(frame)$ when a satellite observation is present . The probability of incorrectly detecting a satellite, $P_{ID_{NEO}}$, is the probability that $\Lambda_1(frame)$ is above the threshold and $\Lambda_1(frame)$ is above $\Lambda_2(frame)$ given a stellar observation is present in the data.

Table 3: Performance Metrics Given Stellar Object Present

Performance Metrics	Data in Frame	Categorization
$P_D = P\left(\Lambda_2 \bigcup \Lambda_1 > \tau\right) \mid H_2$	Star Present	Object Present
$P_{FA} = P\left(\Lambda_1 \bigcup \Lambda_2 > \tau\right) \mid H_0$	Star not Present	False Detection of Target
$P_{D_{star}} = P\left(\Lambda_2 > \tau \bigcap \Lambda_2 > \Lambda_1\right) \mid H_2$	Star Present	Correct Detection of Star
$P_{ID_{NEO}} = P(\Lambda_1 > \tau \bigcap \Lambda_1 > \Lambda_2) \mid H_2$	Star Present	Incorrect Detection of Star
$P_{Miss} = P\left(\Lambda_2 \bigcap \Lambda_1 < \tau\right) \mid H_2$	Star Present	Missed Detection of Star

Due to the presence of noise in the data frames being run through the CD MHT algorithm, the value of $\Lambda_1(frame)$ and $\Lambda_2(frame)$ will differ with every run. Because the LRT is made up of a sum of many pixels, each of which is a random realization, the central limit theorem (CLT) dictates that the LRT follows a Gaussian distribution. The range of values which the LRT can take on makes up all possible thresholds. These thresholds depend on whether the data being tested has background or an observation present. There is a unique probability of detection for every distinct threshold value and a plot of these probabilities versus threshold values is called the cumulative distribution plot CDF plot. In the binary

hypothesis case, the probability of a detection given a certain threshold, τ, can be computed by taking the integral from the threshold to infinity. This is also the right tail of the CDF and can be found by subtracting the CDF from 1.

$$P_D(\tau) = \int_{\tau}^{\infty} \frac{1}{\sqrt{2\pi\sigma^2}} e^{-(x-m)^2/2\sigma^2} dx$$
$$P_D(\tau) = \int_{\tau}^{\infty} \frac{1}{\sqrt{2\pi\sigma^2}} e^{-(x-m)^2/2\sigma^2} dx = 1 - \int_{-\infty}^{\tau} \frac{1}{\sqrt{2\pi\sigma^2}} e^{-(x-m)^2/2\sigma^2} dx \quad (3.68)$$

Likewise, the probability of false alarm can be computed with the only difference being that the data under the null hypothesis is a zero-mean random number.

$$P_{FA}(\tau) = \int_{\tau}^{\infty} \frac{1}{\sqrt{2\pi\sigma^2}} e^{-(x)^2/2\sigma^2} dx$$
$$P_{FA}(\tau) = \int_{\tau}^{\infty} \frac{1}{\sqrt{2\pi\sigma^2}} e^{-(x)^2/2\sigma^2} dx = 1 - \int_{-\infty}^{\tau} \frac{1}{\sqrt{2\pi\sigma^2}} e^{-(x)^2/2\sigma^2} dx \quad (3.69)$$

A Monte Carlo method is utilized to determine the mean, m, variance, σ^2, and standard deviation, σ, of the LRT so that probabilities can be computed using the Gaussian CDF. All the possible thresholds are also determined by taking the minimum and maximum of a data set containing many realized LRT values given many random data frame inputs under the hypotheses that an object is present or absent. With the introduction of multiple hypotheses, the computation of probability of detection becomes more challenging. The probability needs to consider that the LRT is larger than some threshold and larger than the LRT with the other detection hypothesis. Each LRT takes the form of a Gaussian random number, X_1 and X_2, defined respectively by its mean, m_1 and m_2, and standard deviation, σ_1 and σ_2. If the LRT given the hypothesis that a satellite is present minus the LRT given the hypothesis that a star is present is greater than unity, a satellite observation has taken

place. The probability that a satellite observation has taken place is found using the new random variable Z_1 which is the difference between the Gaussian random numbers X_1 and X_2 (3.41). Z_1 is also a Gaussian random number because any linear combination of Gaussian random numbers produces another Gaussian random number; the mean of Z_1 is the differences between the mean of X_1 and X_2 [17]. (3.72) and (3.73) show how to compute the variance of Z_1 and the correlation coefficient between X_1 and X_2.

$$Z_1 = X_1 - X_2 \tag{3.70}$$

$$\bar{Z}_1 = E[Z_1] = m_{z_1} = m_1 - m_2 \tag{3.71}$$

$$\sigma_{Z_1}^2 = E\left[(Z_1 - \bar{Z}_1)^2\right] = \sigma_1^2 + \sigma_2^2 - 2\sigma_1\sigma_2\rho_{12} \tag{3.72}$$

$$\rho_{12} = \frac{E\left[\left(X_1 - \bar{X}_1\right)\left(X_2 - \bar{X}_2\right)\right]}{\sigma_1\sigma_2} \tag{3.73}$$

The probability that $X_1 > X_2$ is the same as the probability that $Z_1 > 0$. This probability can be computed using the Gaussian CDF given the appropriate inputs.

$$P_{\Lambda_1>\Lambda_2} = P(X_1 - X_2 > 0) = P(Z_1 > 0) \tag{3.74}$$

$$\begin{aligned} P(Z_1 > 0) &= \int_0^\infty \frac{1}{\sqrt{2\pi\sigma_{z_1}^2}} e^{-(x-m_{z_1})^2/2\sigma_{z_1}^2} dx \\ &= \int_0^\infty \frac{1}{\sqrt{2\pi\sigma_{z_1}^2}} e^{-(x-m_{z_1})^2/2\sigma_{z_1}^2} dx = 1 - \int_{-\infty}^0 \frac{1}{\sqrt{2\pi\sigma_{z_1}^2}} e^{-(x-m_{z_1})^2/2\sigma_{z_1}^2} dx \end{aligned} \tag{3.75}$$

The probability of detecting a satellite when the satellite is present in the data is found by multiplying the probability that $X_1 > X_2$ by the probability that an object has been detected, P_D. If the two events are disjoint, the intersection of the two events is the product.

$$\begin{aligned} P_{D_{NEO}} &= P\left(\Lambda_1 > \tau \bigcap \Lambda_1 > \Lambda_2\right) | H_1 \\ &= P(Z_1 > 0) \cdot P_D \end{aligned} \tag{3.76}$$

Likewise, the probability that a star observation has taken place is found using the new random variable Z_2 which is the difference between the random numbers X_2 and X_1. Z_2 is also a Gaussian random number and following the same logic as before; the mean of Z_2 is the differences between the mean of X_2 and X_1. (3.79) shows how to compute the variance of Z_2 and the correlation coefficient, ρ_{12}, is computed with (3.73).

$$Z_2 = X_2 - X_1 \tag{3.77}$$

$$\bar{Z}_2 = E[Z_2] = m_{z_2} = m_2 - m_1 \tag{3.78}$$

$$\sigma_{Z_2}^2 = E\left[(Z_2 - \bar{Z}_2)^2\right] = \sigma_1^2 + \sigma_2^2 - 2\sigma_1\sigma_2\rho_{12} \tag{3.79}$$

Next is the converse, the probability that $X_2 > X_1$ is the same as the probability that $Z_2 > 0$. This probability can be computed using the Gaussian CDF given the appropriate inputs seen above.

$$P_{\Lambda_2 > \Lambda_1} = P(X_2 - X_1 > 0) = P(Z_2 > 0) \tag{3.80}$$

$$\begin{aligned} P(Z_2 > 0) &= \int_0^\infty \frac{1}{\sqrt{2\pi\sigma_{z_2}^2}} e^{-(x-m_{z_2})^2/2\sigma_{z_2}^2} dx = 1 - CDF \\ &= \int_0^\infty \frac{1}{\sqrt{2\pi\sigma_{z_2}^2}} e^{-(x-m_{z_2})^2/2\sigma_{z_2}^2} dx = 1 - \int_{-\infty}^0 \frac{1}{\sqrt{2\pi\sigma_{z_2}^2}} e^{-(x-m_{z_2})^2/2\sigma_{z_2}^2} dx \end{aligned} \tag{3.81}$$

As before, the probability of detecting a star when the star is present in the data is found by multiplying the probability that $X_2 > X_1$ by the probability that an object has been detected, P_D.

$$\begin{aligned} P_{D_{star}} &= P\left(\Lambda_2 > \tau \bigcap \Lambda_2 > \Lambda_1\right) | H_2 \\ &= P(Z_2 > 0) \cdot P_D \end{aligned} \tag{3.82}$$

The computation of P_{FA} is also more complex given the multi-hypothesis case. A false alarm occurs when background data is present in the frame being tested but the CD MHT algorithm detects that a satellite or stellar object is present. Either of the LRTs need to be above the threshold in the presence of background for a detection to be made erroneously.

$$\begin{aligned} P_{FA} &= P\left(\Lambda_1 \bigcup \Lambda_2 > \tau\right) | H_0 \\ &= P\left(\Lambda_1 > \tau\right) + P\left(\Lambda_2 > \tau\right) - P(\Lambda_1 \bigcap \Lambda_2 > \tau) \end{aligned} \tag{3.83}$$

The probability that the two different LRTs are above the threshold is computed using the same methodology as with computing probability of detection as seen in (3.68).

$$\begin{aligned} P_{\Lambda_1 > \tau}(\tau) &= \int_{\tau}^{\infty} \frac{1}{\sqrt{2\pi\sigma_1^2}} e^{-(x-m_1)^2/2\sigma_1^2} dx = 1 - \int_{-\infty}^{\tau} \frac{1}{\sqrt{2\pi\sigma_1^2}} e^{-(x-m_1)^2/2\sigma_1^2} dx \\ P_{\Lambda_2 > \tau}(\tau) &= \int_{\tau}^{\infty} \frac{1}{\sqrt{2\pi\sigma_2^2}} e^{-(x-m_2)^2/2\sigma_2^2} dx = 1 - \int_{-\infty}^{\tau} \frac{1}{\sqrt{2\pi\sigma_2^2}} e^{-(x-m_2)^2/2\sigma_2^2} dx \end{aligned} \tag{3.84}$$

Computing the joint probability that both LRTs are above the threshold involves the bi-variate CDF and the joint probability involves integrating the density function of the bi-variate Gaussian distribution given the appropriate inputs as seen in (3.85).

$$\begin{aligned} P_{\Lambda_1 \& \Lambda_2 > \tau}(\tau) &= \int_{\tau}^{\infty}\int_{\tau}^{\infty} \frac{1}{2\pi\sigma_1\sigma_2\sqrt{1-\rho_{12}^2}} e^{-\frac{1}{2(1-\rho_{12}^2)}\left[\frac{(x-m_1)^2}{\sigma_1^2} + \frac{(y-m_2)^2}{\sigma_2^2} - \frac{2\rho_{12}(x-m_1)(y-m_2)}{\sigma_1\sigma_2}\right]} dxdy \\ &= 1 - \int_{-\infty}^{\tau}\int_{-\infty}^{\tau} \frac{1}{2\pi\sigma_1\sigma_2\sqrt{1-\rho_{12}^2}} e^{-\frac{1}{2(1-\rho_{12}^2)}\left[\frac{(x-m_1)^2}{\sigma_1^2} + \frac{(y-m_2)^2}{\sigma_2^2} - \frac{2\rho_{12}(x-m_1)(y-m_2)}{\sigma_1\sigma_2}\right]} dxdy \end{aligned} \tag{3.85}$$

The bivariate CDF can be computed using the mean matrix, $\underline{m}$, which is a matrix containing the mean of the two LRT's and the covariance matrix, $\underline{\Sigma}$, which is a matrix containing the variances on the diagonal and the covariances on the off-diagonal.

$$\underline{\Sigma} = \begin{bmatrix} \sigma_1^2 & E\left[\left(X_1 - E[X_1]\right)\cdot\left(X_2 - E[X_2]\right)\right] \\ E\left[\left(X_2 - E[X_2]\right)\cdot\left(X_1 - E[X_1]\right)\right] & \sigma_2^2 \end{bmatrix} \tag{3.86}$$

$$\underline{\mathrm{m}} = \begin{bmatrix} m_1 \\ m_2 \end{bmatrix} \tag{3.87}$$

Each of the probabilities can be plotted together given the entire range of possible thresholds to show if the algorithm is effective at distinguishing between stellar and NEO observation detections. As the baseline distance between the parallax and reference telescopes increases, the probability of correctly detecting a satellite given that a satellite is present in the data will be higher than the probability of incorrectly detecting that a star is present or the probability of missing the detection of an object the data all together. Generally, the performance of a detection algorithm will be quantified using a receiver operating characteristics (ROC) curve. The ROC curve is a plot of the probability of detection versus the probability of false alarm. Such a curve is very useful when trying to compare the performance of different detection schemes. When the ROC curve for different detection schemes is plotted together, the algorithm which produces the higher probability of detection value given the same probability of false alarm has superior performance [19]. ROC curves will show the dependence of the CD MHT algorithm performance on the amount of separation between the reference and parallax sensing telescopes. Each iteration will have a different baseline and produce unique ROC curves. The ROC curve is also useful for quickly determining what the probability of detection will be given a probability of false alarm.

IV. MATLAB Simulation

In this chapter, the optical system with identical telescopes separated by varying baselines is simulated in MATLAB. Using the theory from Chapter 2, random data frames are generated by creating the paraxial PSF for the reference telescope and the non-paraxial PSF for the parallax sensing telescope for both stellar and GEO targets given the random effects of the atmosphere and the random effects photon arrivals. The CD MHT algorithm defined in Chapter 3 is tested with these simulated data frames as inputs producing an LRT value in the H_1 and H_2 case. Using a Monte Carlo approach by running thousands of randomly generated data frames through the CD MHT algorithm to produce many LRT realizations; these realizations were used to characterize the statistics of the CD MHT algorithm's performance with different target SNR values.

Simulation Setup

The optical system used in this simulation is a F10 telescope with an aperture of 0.288 meters and a focal length of 2.8 meters. Parabolic mirror telescopes utilize an internal reflector to focus observations on the CCD array so an obscuration of .095 meters was added to the aperture to make the simulation better emulate optical systems used for SSA. The aperture plane was made to be double the width of the aperture transmittance function to avoid aliasing from the wrap around effect when taking the Digital Fourier Transform. The aperture transmittance function of this system is depicted in Figure 10; it was defined as zero everywhere where there is an obstruction and outside the extent of the mirror and one across the un-obstructed primary mirror.

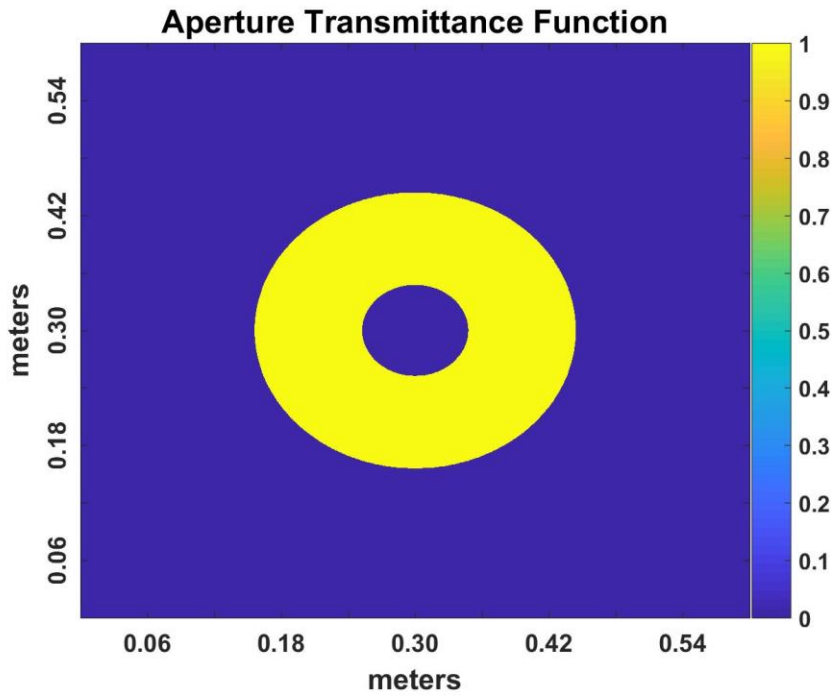

Figure 10: Aperture Transmittance Function for F10 Telescope in Simulation

The phase from a distant object or background radiation travels through space before reaching the aperture from whence only the portions of the electromagnetic field intersecting the un-obstructed portions continue onwards. This is emulated in MATLAB by multiplying the phase function from the object by the aperture transmittance function. A quadratic phase factor from the mirror is added to the optical field which cancels with the Fresnel phase term when observing the propagated field at the focal plane of the optic. In this way, a Fourier transform of the aperture geometry will produce the system's impulse response at the focal plane of the telescope's mirror. As the optical field traveled from a far-off space object, it took the form of a plane wave, and the image viewed at the focal plane is the impulse response for this optical system. The impulse response was found by implementing Equation (2.7) into the simulation with the MATLAB FT2 command. Per

Equation (2.13), the PSF seen in Figure 11 was normalized such that the area under it is equal to 1. The sampling in the CCD plane was chosen so that each pixel is the size required for Nyquist sampling.

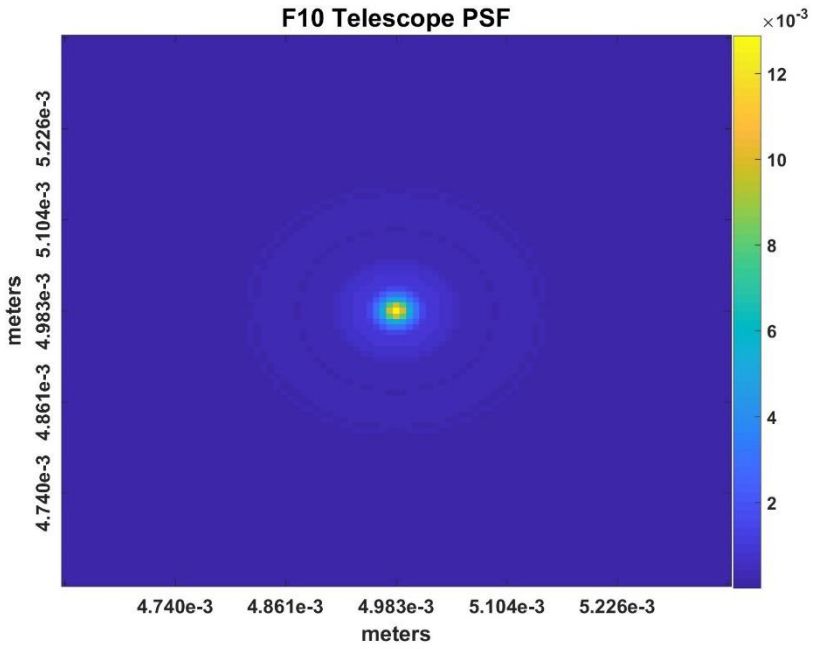

Figure 11: F10 Telescope PSF from 2D Fourier Transform

Average OTF

The long exposure performance of the optical system was found to be the OTF of the perfect optical system multiplied by OTF of the Atmosphere as seen in the average optical transfer function section of Chapter 2. MATLAB was utilized to implement Equation (2.68) which is the transfer function for the atmosphere derived using Kolmogorov's structure function. Figure 12 shows the structure function for the atmosphere given a seeing parameter of 15 cm and the optical system seen in Figure 10.

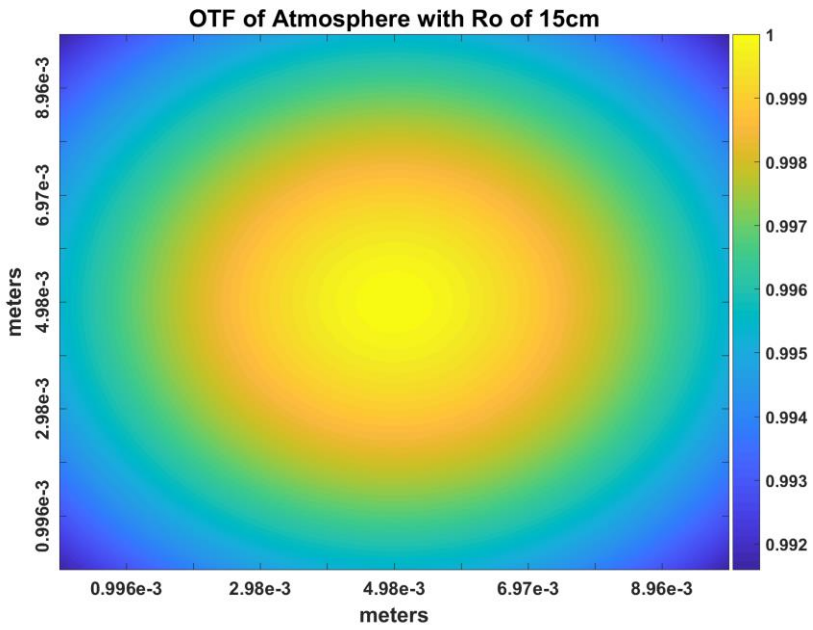

Figure 12: OTF of the Atmosphere with 15 cm r_o and 28.8 cm Aperture Diameter

Figure 13 shows the OTF of the F10 Telescope with an aperture diameter of 28.8 cm using the phase at the aperture of the reference telescope. This was computed by taking the Fourier Transform of the un-aberrated telescope PSF because the OTF and PSF are Fourier Transform pairs as stated in Equation (2.22).

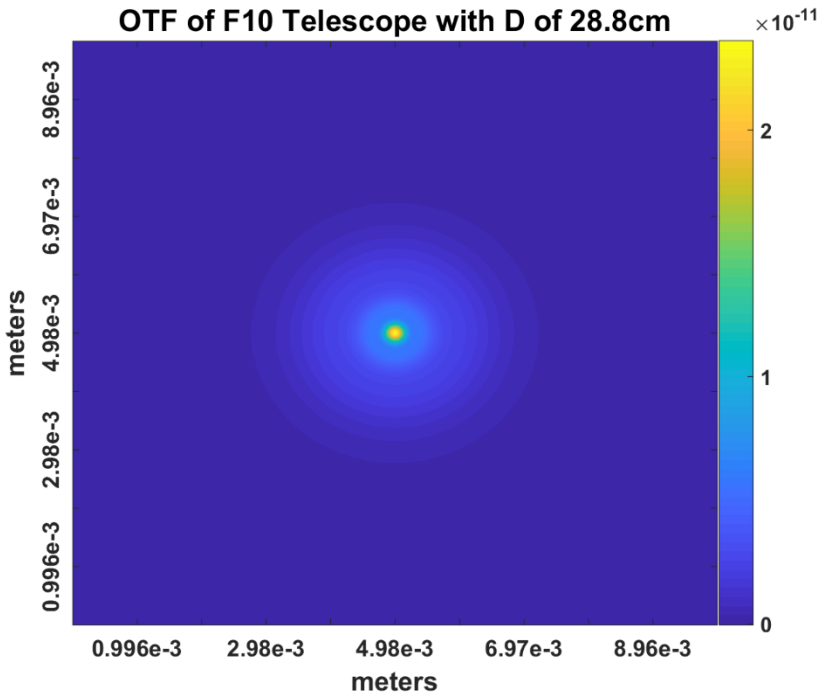

Figure 13: OTF of F10 Telescope with 28.8 cm Diameter

The Average Transfer Function resulting from a long exposure image of some distant object is found by multiplying the OTF of the perfect optical system by the transfer function of the atmosphere. The aberrated PSF or system PSF is computed by taking the inverse Fourier transform of this product. Figure 14 is the long exposure PSF of the optical system found by multiplying the atmospheric OTF by the un-aberrated telescope OTF. Figure 15 is the PSF of the of the entire optical system; it shows what a distant star or space object would look like when being viewed with this optical system using long integration times in the absence of other noise factors. A long integration time is produced by opening the camera shutter for longer periods of time. The same effect could be realized by taking some number of short exposure images and averaging the resulting PSFs.

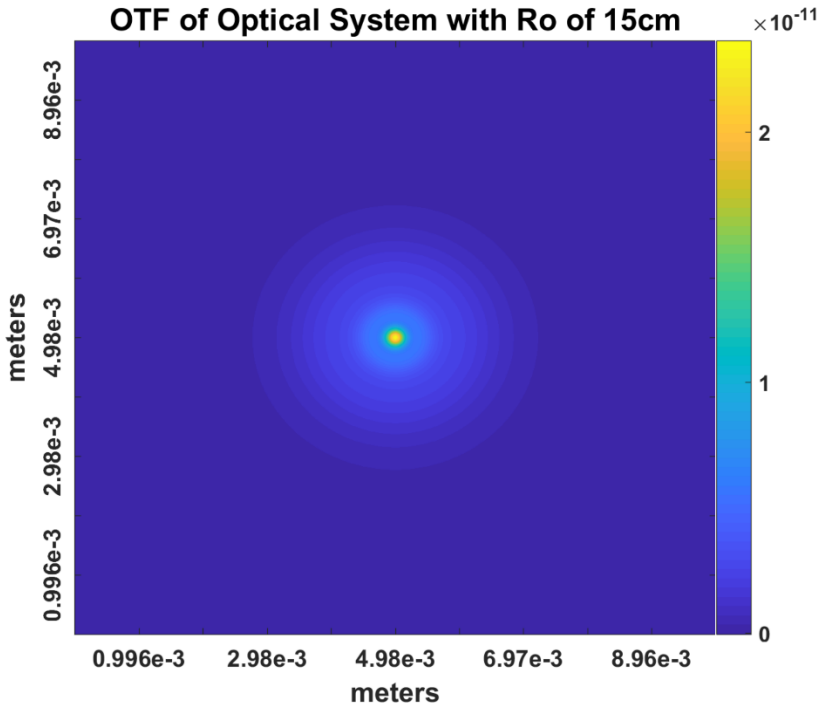

Figure 14: Total OTF of Atmosphere and Telescope with 15 cm r_0 and D of 28.8 cm

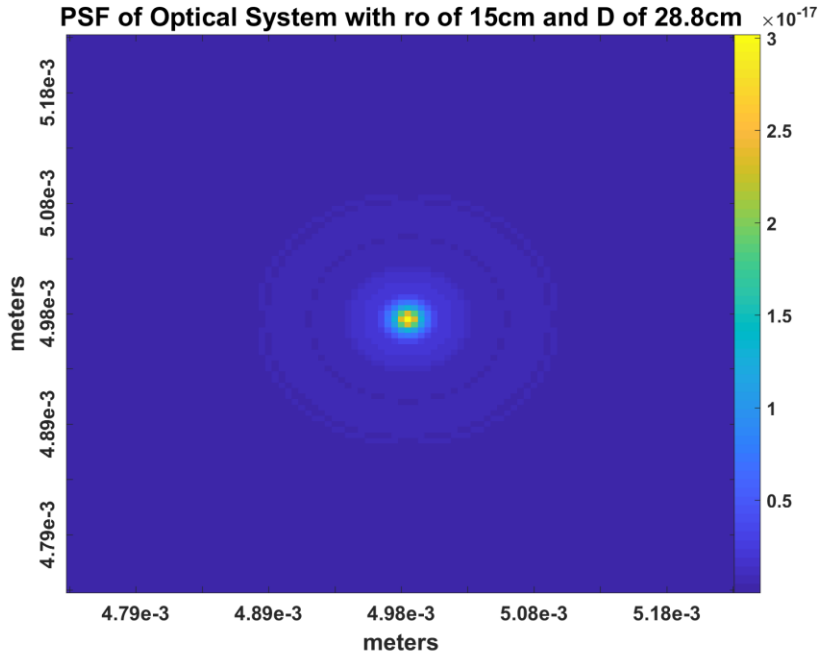

Figure 15: PSF of Total Optical System with 15 cm r_0 and D of 28.8 cm

Off-Axis PSF

The effects of parallax will be manifested in the movement and spatial distribution of the observed PSF through the reference and parallax sensing telescopes. A phase front is generated in MATLAB which encompasses both telescopes aperture planes. The phase is taken as a spherically symmetric electromagnetic field emanating from a distant point source. The two telescopes are arranged in the same plane a specified distance apart from each other as seen in Figure 4. These distances are referred to as telescope baselines. The selected F10 telescope with an aperture of 0.288 meters and a focal length of 2.8 meters was chosen to meet the limiting conditions that most of the energy in the PSF be within an area of the F number squared Nyquist pixels. As seen in Equation (2.38), meeting this condition ensures the accuracy of the off-axis propagation tool because the hybrid propagator correctly samples the PSF to prevent extra aliasing. The telescope modeled in simulation has an F# of approximately 10 so the PSF should be contained within a region of 100 Nyquist pixels squared. It is convenient that the PSF was normalized because the amount of total energy in a chosen region of the CCD plane is proportional to the total energy contained in the entire CCD. By doing a double sum of the PSF confined to the regions of 50 Nyquist pixels, as seen in Figure 16, and the double sum of the PSF confined in the region of 100 Nyquist pixels, the percent of total energy in these two regions is 84.8% and 98.6% respectively. This system beats the sampling requirement by almost a factor of ten.

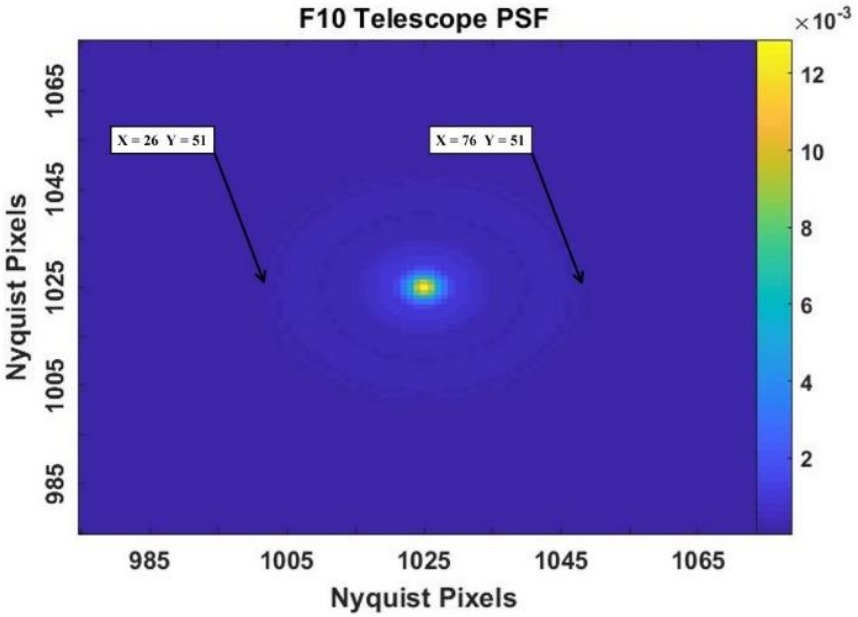

Figure 16: Area Containing F10 Telescope PSF in Nyquist Pixels

In this simulation, the baseline is only varied in the horizontal direction to show that the tilt aberrations are directly related to the separation of the two telescopes. Only varying the separations along one axis more clearly demonstrates how the spatial distribution of the non-paraxial PSF changes as it's center location is specified to be farther from the optical focus of the telescope. Additionally, a simple coordinate transformation can put any two-telescope system into this geometric orientation. The baselines were incremented from zero to 10 km in steps of 20 m, 200 m and 2000 m to produce five data sets between 0 m and 100 m, 0 m and 1000 m and 0 m and 10000 m respectively. A GEO object is placed at 36,000 km centered on the optical axis of the reference telescope. The phase curvature of the lens as defined in Chapter 2 was added to the electromagnetic phase from the GEO point source to model the complete phase in the aperture plane of each of the two telescopes and then multiplied by the aperture transmittance function to form the pupil function seen

in Equations (2.20) and (2.21). For the non-paraxial parallax sensing telescope, the PSF was computed by discretizing the hybrid propagator defined in the non-paraxial PSF generation section and noting that the entire array needs to be shifted to account for the center of that grid being located where geometric optics predicted the PSF to be centered. The PSF center location was specified based on geometric optics from the amount of horizontal baseline separation between the reference telescope and the parallax sensing telescope. The PSF separation is caused by the aberrations in the phase front which are present in the parallax sensing telescope's phase but not present in the reference telescope's phase. Table 4 shows the PSF center locations as predicted by geometric optics and the additional PSF shift from the tilt aberrations otherwise neglected by taking the Fourier Transform of the aperture. The extra shift was observed in the PSF generated using the hybrid propagator tool and clearly demonstrates the effects of parallax on the PSF in the parallax sensing telescope. Between 1 km and 10 km, the PSF moved an extra 1 Nyquist pixel to 7 Nyquist pixels.

Table 4: F10 Telescope System with 288mm Aperture Diameter and 2.8m Focal Length

Telescope Baseline (m)	PSF Center Location (grids)	PSF Center Location (um)	PSF Shift from Phase (grids)	PSF Shift from Phase (um)	Total PSF Shift (grids)	Total PSF Shift (um)
20	0	0	0	0	0	0
40	1	4.861	0	0	1	4.861
60	1	4.861	0	0	1	4.861
80	2	9.270	0	0	2	9.270
100	2	9.720	0	0	2	9.720
200	3	14.58	0	0	3	14.58
400	6	29.16	0	0	6	29.16
600	10	48.60	0	0	10	48.60
800	13	63.18	0	0	13	63.18
1000	16	77.67	1	4.861	17	82.64
2000	32	155.5	1	4.861	33	160.4
4000	64	311.0	2	9.722	68	330.6
6000	96	466.7	3	14.58	99	481.3
8000	128	622.1	5	24.31	133	646.5
10000	160	777.6	7	34.03	167	811.8

The Reference PSF and non-paraxial PSFs produced with baselines of 0 m to 1000 m in iterations of 200 m are shown in Figure 17. The geometric shift of the off-axis PSF is annotated in the figures in Nyquist pixels.

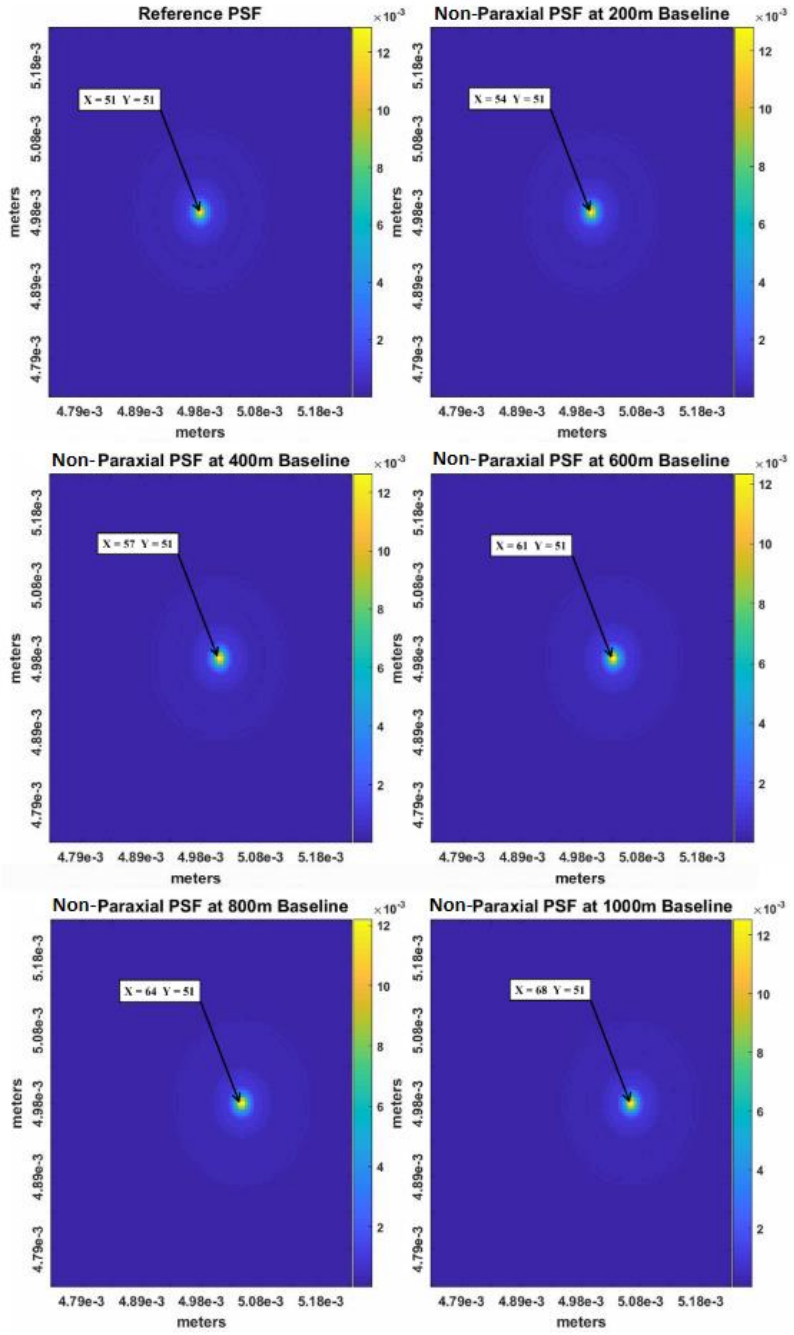

Figure 17: Non-Paraxial PSF From Baselines of 0 meters to 1000 meters with NEO

Figure 18 shows zoomed in images of the same six PSFs demonstrating the change in the spatial distribution of the PSFs which is due to the extra terms normally neglected by the Fresnel approximation at the focal point but accounted for by the non-paraxial propagator.

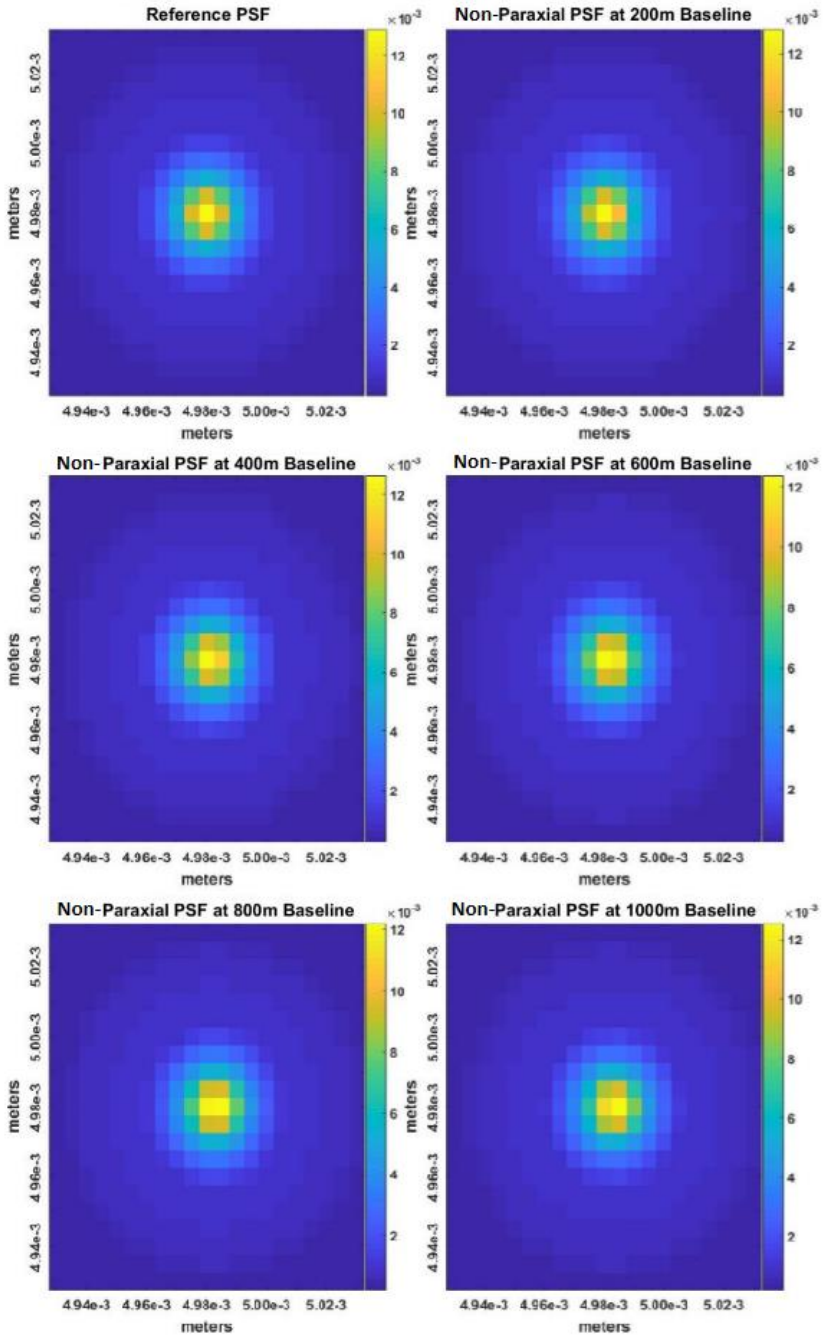

Figure 18: Enlarged Non-Paraxial PSF From Baselines of 0 meters to 1000 meters

Starting with the non-paraxial PSF with a telescope separation of 400 m, the PSF starts to skew to the right in the horizontal direction. The mass of the PSF continues to lean to the right until its center of mass finally shifts by one additional pixel as seen in the enlarged non-paraxial PSF at a 1000 m telescope baseline. Also of note is that every off-axis PSF has a unique spatial distribution which, when applied as an input to the CD MHT algorithm, would be clearly identified. So, even in the absence of the geometric center change, the different PSFs are still distinguishable which clearly demonstrates the utility of the non-paraxial propagation tool for detection purposes. Figure 19 and Table 5 shows the six PSF's phase as decomposed into orthonormal Zernike polynomials. From the figure, the effects of propagating a PSF to an off-axis location as predicted by geometric optics can be precisely measured by Zernike polynomial weighting factors. The effects on the phase of the PSF as observed by a parallax sensing telescope are entirely described by Piston and Horizontal Tilt. The steady rightward shift of the PSF as seen in Figure 18 is a manifestation of the horizontal tilt aberration. Piston is the mean value of the optical wave-front across the plane of interest; when the PSF is skewed due to tilt, the mean value of the phase will also change.

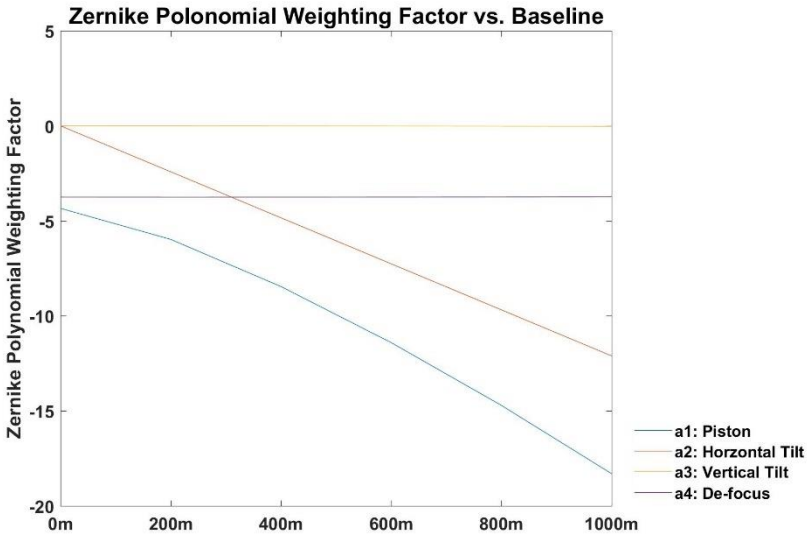

Figure 19: Zernike Polynomial Decomposition of Off-Axis PSFs at Varying Baselines

Table 5: Decomposition of PSF Phase at Different Baselines into Zernike Polynomials

	0m	200m	400m	600m	800m	1000m
a_1: Piston	-4.34	-5.98	-8.46	-11.4	-14.7	-18.3
a_2: Horizontal Tilt	-0.00	-2.41	-4.83	-7.26	-9.68	-12.1
a_3: Vertical Tilt	-0.00	-0.00	-0.00808	-0.0139	0.0208	-0.0284
a_4: De-focus	-3.75	-3.75	-3.75	-3.75	-3.74	-3.74

Next, a star is placed 4.5 lightyears away centered on the optical axis of the reference telescope; this distance is the distance to Alpha Centauri which is the next closest star to the earth. The phase curvature of the lens was added to the electromagnetic phase from the stellar point source to model the complete phase in the aperture plane of each of the two telescopes and then multiplied by the aperture transmittance function to form the pupil function seen in Equations (2.20) and (2.21). Figure 20 shows that as the baseline changes, the PSF location does not change in this configuration. This is due to the phase from the star at the plane of both the reference and parallax sensing telescopes being flat enough that there are no aberrations due to tilt and the PSF location stays centered in both

telescopes. Figure 21 shows the Zernike polynomial weighting factors at each baseline; for every baseline separation, the tilt, piston and defocus are constant. This verifies that tilt is not changing the spatial distribution of the PSFs given that a stellar object is being observed.

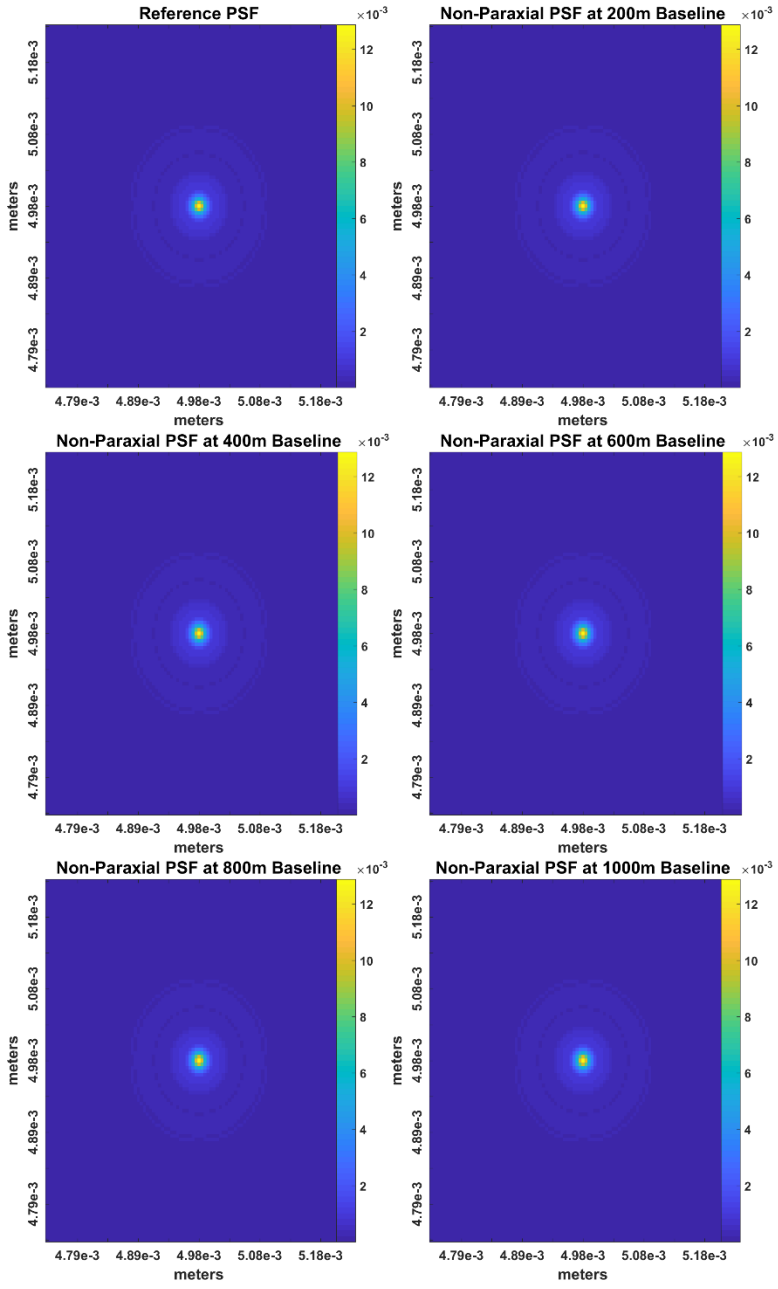

Figure 20: Non-Paraxial PSF From Baselines of 0 meters to 1000 meters with Star

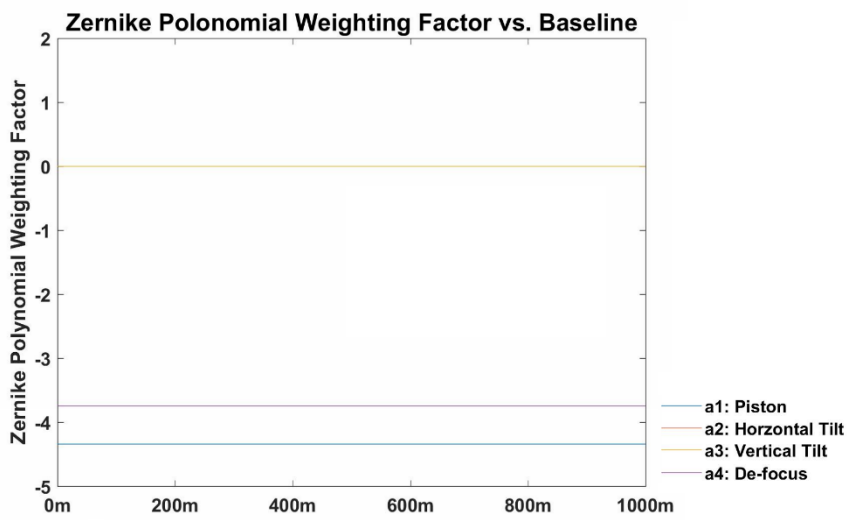

Figure 21: Zernike Polynomial Decomposition of Off-Axis PSFs at Varying Baselines

From this simulation, it has been verified that the parallax experimental setup laid out in the non-paraxial PSF section of Chapter 2 produces off-axis PSFs with unique spatial distributions provided that an observation is close enough for parallax to induce tilt aberrations. Thus, the hybrid propagator is an effective tool for properly constructing the phase profile of off-axis PSFs. Shortly, it will be demonstrated that the CD MHT algorithm developed in Chapter 3 is effective at identifying these unique PSFs which easily allows for the proper categorization of SSA observations as either a NEO or a stellar object.

Simulating Background Noise and Frames of Data

MATLAB was utilized to simulate the PSF of a distant star assuming that the observation will be made from the collection of many photons incident on the detector with a finite integration time. The derivations in the photon counting noise section of Chapter 2 show clearly that the distribution when observing photons incident at a detector is Poisson. The PSF is found by computing the OTF of the optical system and taking the Inverse Fourier

Transform of that quantity. The average OTF section of Chapter 3 was utilized to create the PSF which is then convolved with an observed image to produce what will be seen by the CCD. Space observations' luminosity is selected using the stellar magnitude scale which is a logarithmic quantity where a smaller number represents a brighter object. The relative brightness of objects can be compared to a magnitude one object which has the luminosity equivalent to the star known as Vega. Because either a stellar or GEO observation is so far away, the image will appear to be a point source to the telescope aperture. To simulate this, the center pixel of the plane containing that object is scaled by the number of photons expected to emanate from that object. The number of photons is computed using the magnitude of luminosity relative to Vega. Background luminosity is selected to achieve desired pixel SNR levels so that the performance of the algorithm can be tested across a wide range of relative luminosity. Every pixel in the observation frame was set to be the expected number of photons from the background which would produce data frames with the desired pixel SNR quantity. Figure 22 is an observation and background with the observation being a point source and the background set to achieve a desired SNR in the data frame.

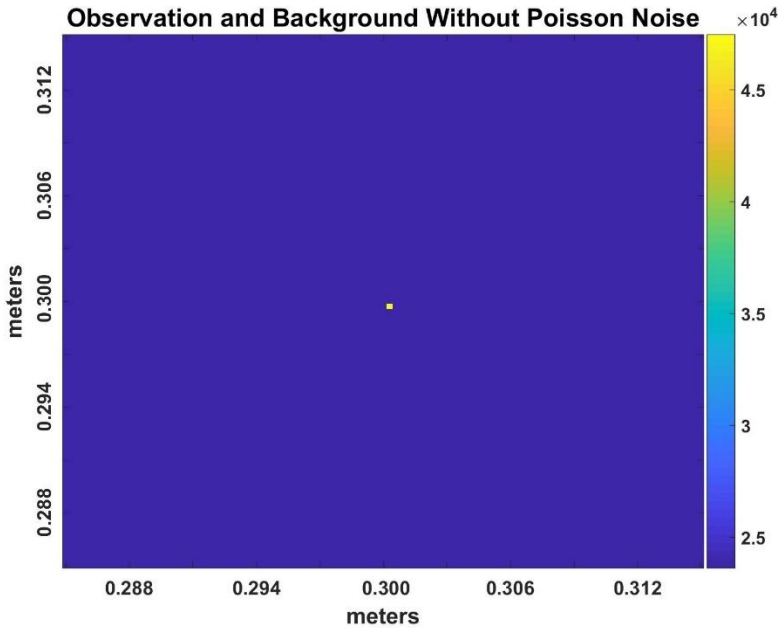

Figure 22: Observation and Background Luminosity without Poisson Noise

The observation in Figure 22 is convolved with the total system PSF to produce the image expected at the CCD array which is seen in Figure 23.

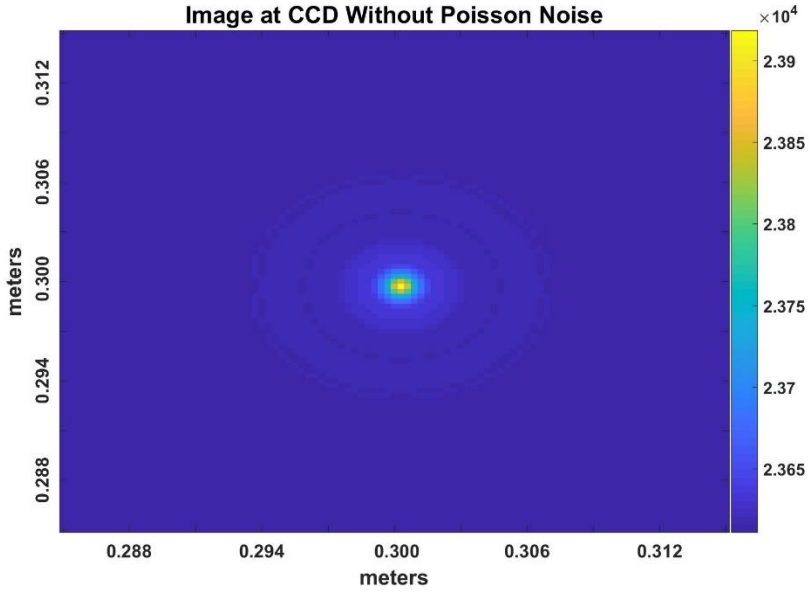

Figure 23: Image at CCD Array

Because photon arrivals take on a Poisson distribution, data frames are randomized using the poissrnd command in MATLAB. Figure 24 shows a GEO observation in the presence of Poisson background noise at various SNR values.

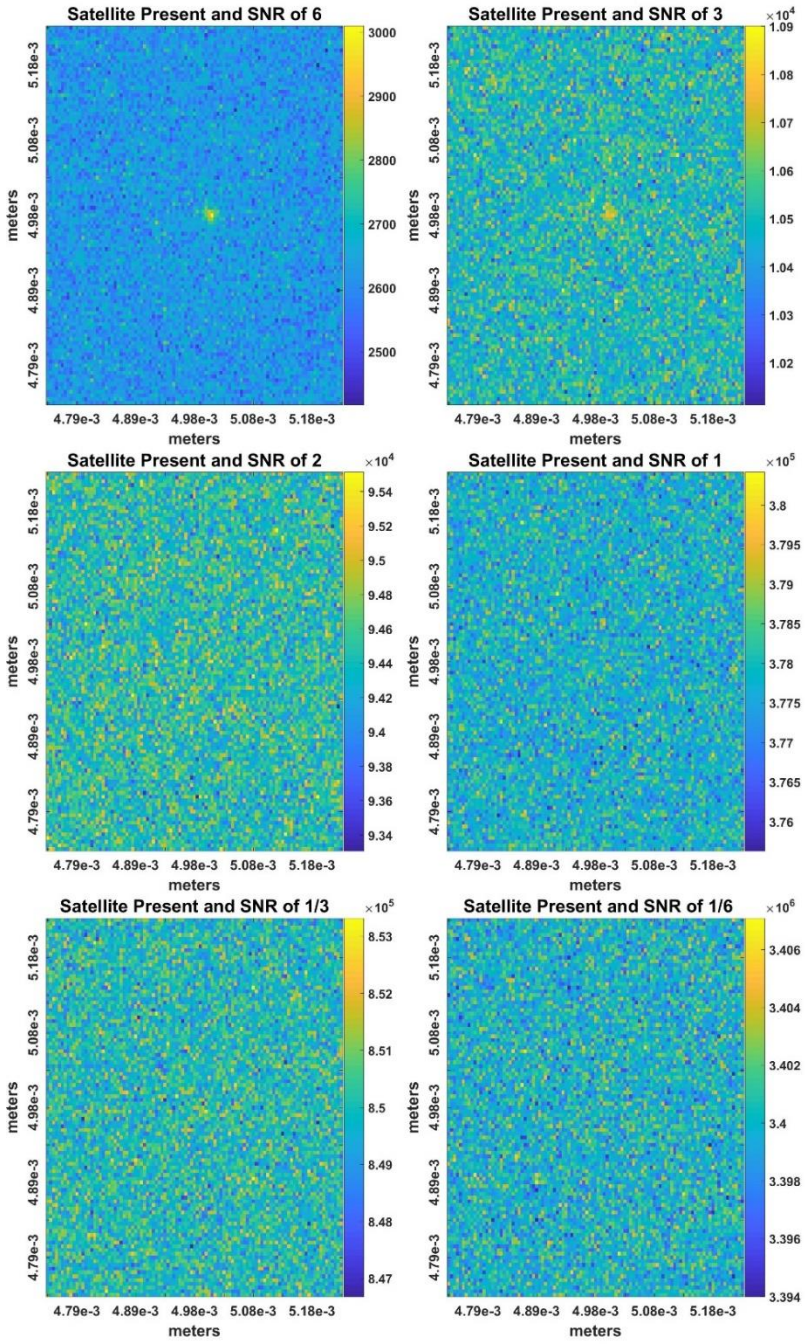

Figure 24: Parallax Data Frames Containing GEO Observations and Background Noise

Figure 25 shows a stellar observation in the presence of Poisson background noise at various SNR values. The difference between the stellar and the GEO observations is that the GEO observation maintains the spatial effects of parallax from the parallax PSF.

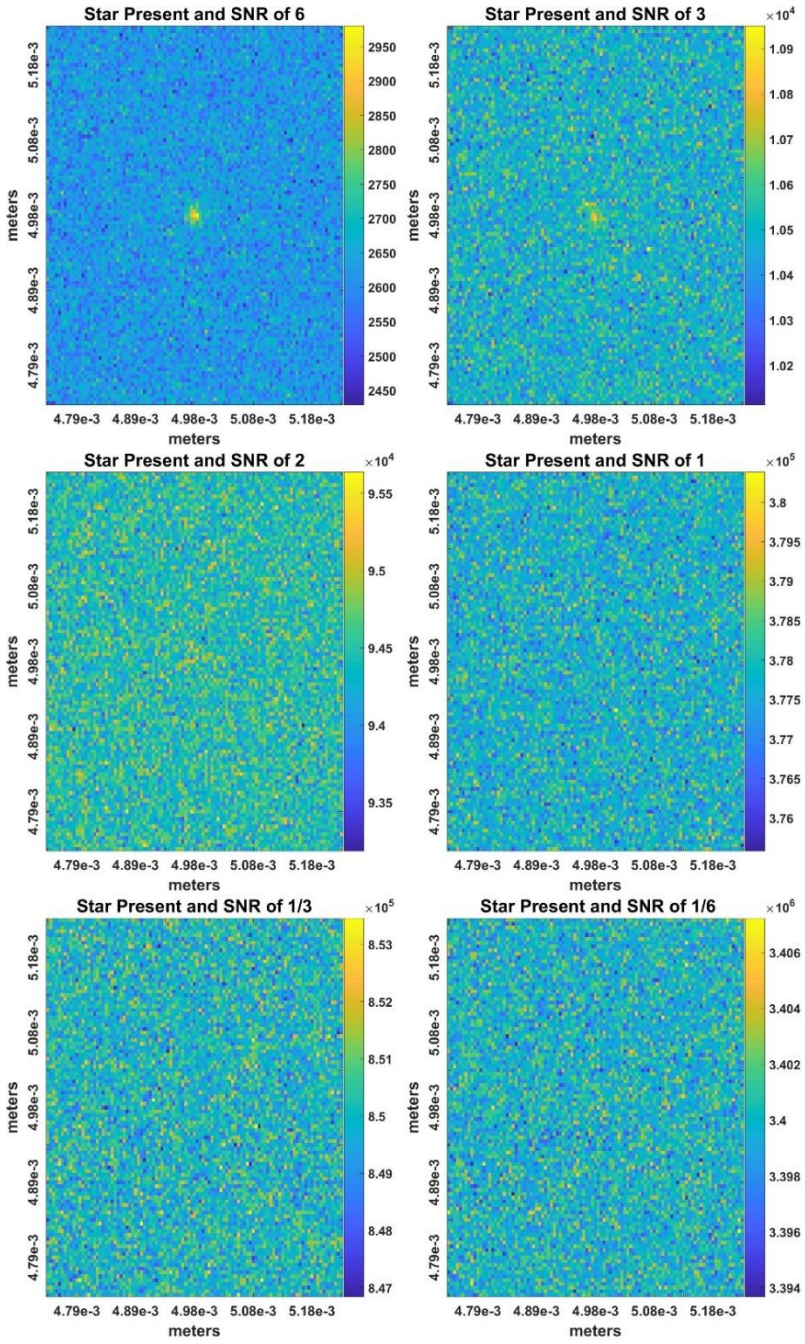

Figure 25: Parallax Data Frames Containing Stellar Observations and Background Noise

Correlator Detector Multi-Hypothesis Test with System of Identical Telescopes

As seen in Figures 24 and 25, it quickly becomes difficult to distinguish the PSF shape among the Poisson background noise. The purpose of this section is to demonstrate that even in the presence of such noise, the CD MHT algorithm developed in Chapter 3 can determine if a detection has occurred and what type of observation has been detected from single frames of data. For the simulation, Equation (3.53) is used for hypothesizing a NEO and Equation (3.54) is used for hypothesizing a stellar observation because dividing by the standard deviation under the null hypothesis produces a background with a unit normal distribution. With this selection, the false alarm probability, P_{FA}, can easily computed using probability tables. This is convenient because USAF SSN sensors calibrate based on desired false alarm rates; otherwise, Equations (3.44) and (3.45) are just as valid for detection and categorization purposes. The performance of the simulation is quantified using the central limit theorem which dictates that a sum of many randomly distributed random variables tends towards a Gaussian distribution. During correlation between the hypothesized PSF for the reference and parallax sensing telescope with inputted data frames, many Poisson distributed pixels are being summed together causing the LRT to behave like a Gaussian Random Variable, RV. This Gaussian RV can be completely described across a range of thresholds by computing the mean and variance of the LRT's Gaussian distribution. To do this, three thousand Monte Carlo Trials are run to find the sample mean and variance of the distribution. This was done by creating three thousand unique data frames and computing a vector of three thousand realizations of the LRT. The sample mean and sample variance is computed from the resulting vector of Gaussian RV's and MATLAB is used to construct the performance metrics of the LRT. The probability of

false alarm, P_{FA}, the probability of detection, P_D, and the probability of missing a detection, P_{Miss}, are created from these large samples of realized LRTs given test data frames containing targets corresponding to the three unique hypotheses. Each random data frame is created by specifying the altitude of the target, it's luminescence and the luminescence of the background. A data cube of many LRT realizations for each type of target and at five different parallax telescope baselines is constructed to robustly describe the behavior of the derived algorithm. Baseline iterations will need to be calibrated depending on the optical equipment used and desired target altitude. In this simulation, baselines were selected in increments of 60 meters from 0 meters to 300 meters because a 60 meter baseline corresponds to a 1 Nyquist pixel shift, from Geometric Optics, of the PSF center location in the parallax sensing telescope. This is specific to the selected altitude of the GEO observation, diameter of the aperture, focal length of the optic, and grid size of the sampled data. Figure 26 shows the performance of the algorithm with the parallax sensing telescope placed 0 meters, 60 meters, 120 meters, 180 meters, 240 meters and 300 meters from the reference telescope. Data frames were generated with a target in GEO at 36,000 km from the plane of the telescope apertures. The optical axis of the reference telescope is lined up with the target and the parallax sensing telescope is oriented such that it's optical axis is parallel to the reference telescope's optical axis. From the figure, the probability of detecting a NEO in the data, $P_{D\ NEO}$, is over the probability of false alarm, P_{FA}, for all thresholds and the ROC curve shows that even at extremely small P_{FA} values on the order of 10^{-15}, detection of the target is assured. At a baseline separation of 0 meters, the PSF looks exactly like a stellar PSF because the parallax sensing telescope is co-located with the reference telescope. The result that there is a 50/50 chance of either correctly detecting

a NEO or incorrectly detecting a star given the target is a NEO is logical and serves as a good reference point.

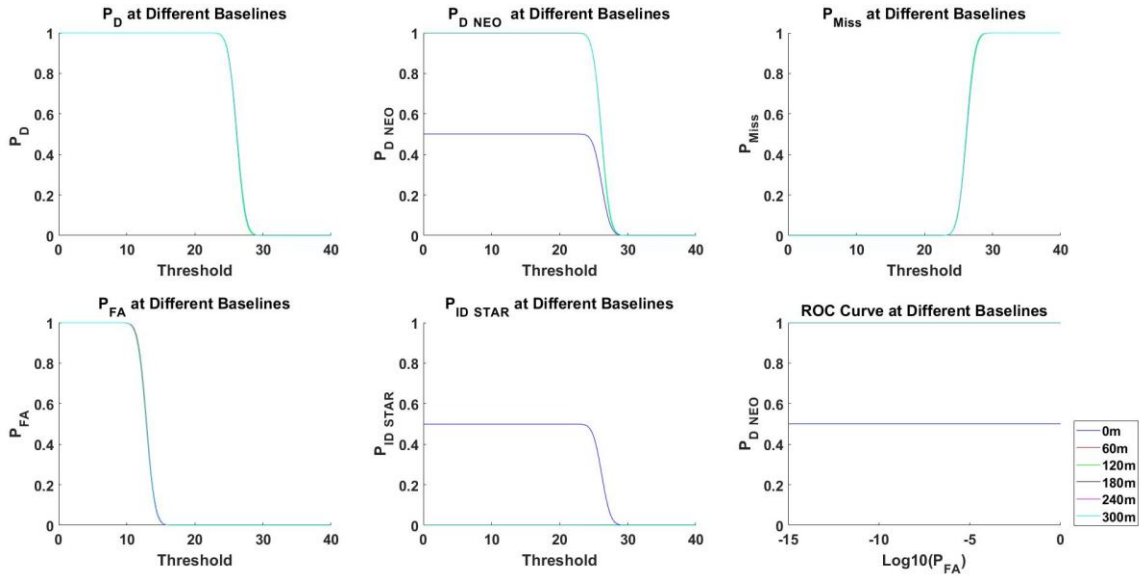

Figure 26: Algorithm Performance with Satellite Present in Data Frame and SNR of 6

The algorithm is next tested using data frames with a pixel SNR of 3 as seen in Figure 27. Given the additional noise in the data, $P_{D\ NEO}$ has dropped from nearly 100% to about 95% and $P_{ID\ STAR}$ has risen from around 0% to 5% over the vast range of possible LRT thresholds given a 60 meter parallax telescope baseline. The ROC curve shows that the performance of the algorithm using a 60 meter baseline has diminished as compared to the other non-zero baselines for P_{FA}'s ranging from 10^{-7} to 1. With a pixel SNR of 3, $P_{D\ NEO}$ is above 95% for the 60 meter baseline optical system and nearly 100% at the other non-zero baseline systems given a P_{FA} of 10^{-9}. As seen in Figure 24, the PSF is hardly visually distinguishable in this case even though it's brightest pixel is three times more luminescent than the average background pixels. $P_{D\ NEO}$ does not always range from 0% to 100% because there is also the opportunity to incorrectly detect a star.

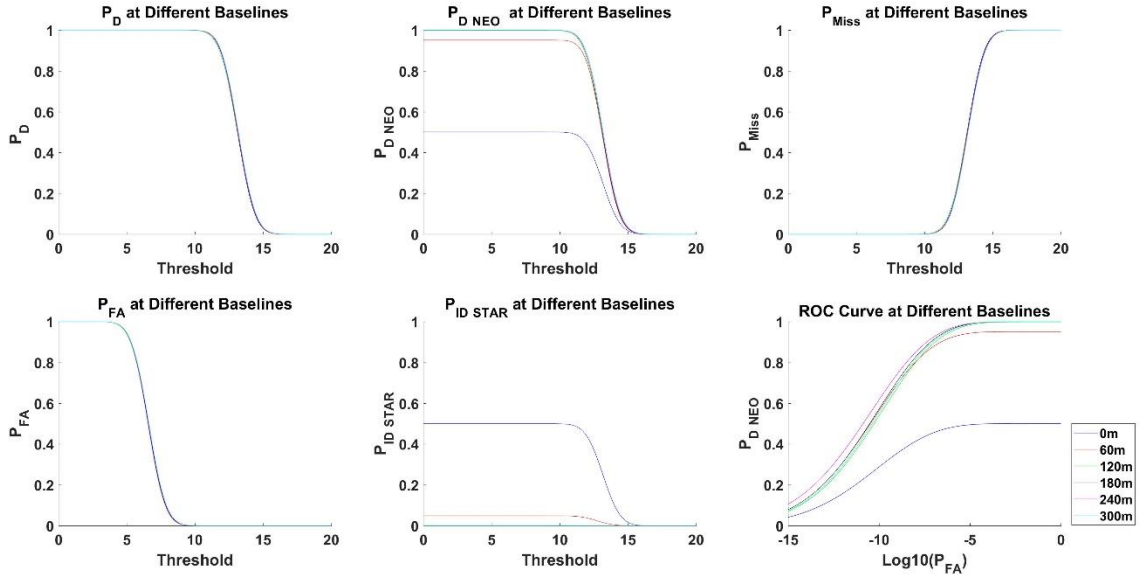

Figure 27: Algorithm Performance with Satellite Present in Data Frame and SNR of 3

From Figure 24, the shape of the PSF is not distinguishable by the human eye given an SNR of 2 in the data frame. As seen in Figure 28, the CD MHT algorithm is still performing well. Optical system arrangements with the parallax sensing telescope baseline separations from 180 meters to 300 meters still have a $P_{D\ NEO}$ of nearly 100% at a P_{FA} of 10^{-9} and the systems with a 60 or 120 meter baseline are at about 85% and 95% for a P_{FA} of 10^{-9}. The ROC curve shows that for P_{FA} values as small as 10^{-3}, $P_{D\ NEO}$ is still nearly 100% given enough baseline separation. For baselines of higher than 180 meters, $P_{ID\ STAR}$ is nearly 0% and at a 120 meter baseline, $P_{ID\ STAR}$ is still below 3%. Even at a small PSF shift of two Nyquist pixels, the algorithm is very perceptive. It is also worth noting that the ROC curve for each successive baseline is over the lower baselines for SNR 2 indicating that as noise increases, larger baseline optical arrangements perform better than systems with smaller baselines.

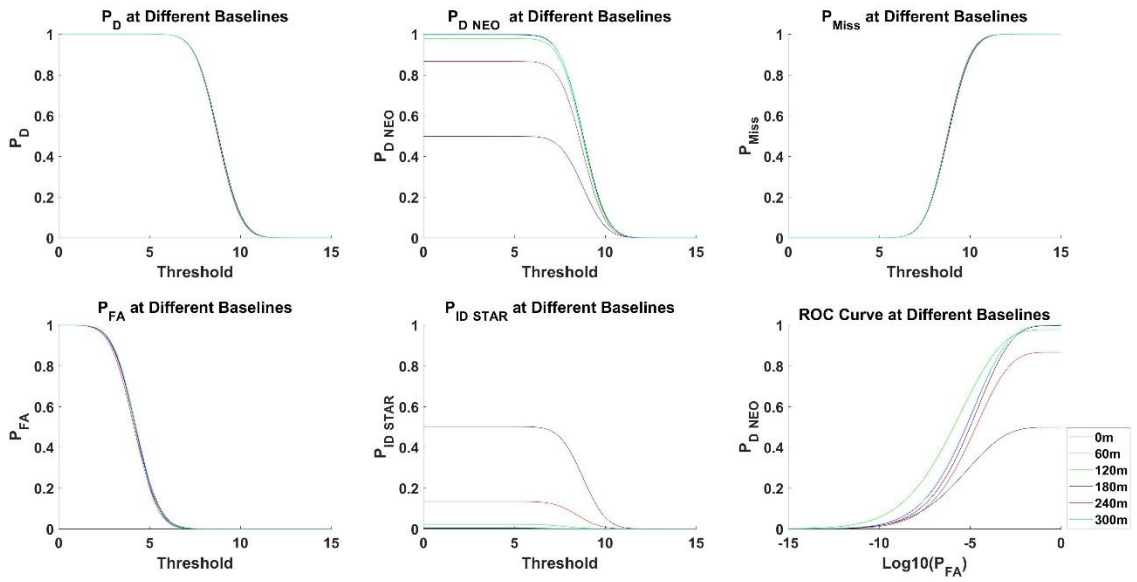

Figure 28: Algorithm Performance with Satellite Present in Data Frame and SNR of 2

At a SNR of 1, the magnitude of luminosity of a background pixel is equivalent to the magnitude of the target. Figure 29 shows that in the presence of more noise, the CD MHT algorithm's performance is more dependent on baseline separation. The larger the baseline, the more dissimilar the non-paraxial PSF is to the reference PSF and the easier it is for the CD MHT algorithm to differentiate the observations. On the ROC curve plot, the three highest baselines performances are very close to each other and for systems with baselines of 180 meters to 300 meters, $P_{D\ NEO}$ only differs by 1-5% with the highest $P_{D\ NEO}$ among them maxing out at 95%. No matter how much extra baseline, $P_{D\ NEO}$ doesn't get as high as 100% even for very large P_{FA} values. Additional separation between the reference and parallax sensing telescope doesn't buy extra performance at some level because at this SNR value, it is more probable that the algorithm will incorrectly determine that an observation is a star when it is a GEO observation. These results show that a NEO can be properly identified by the CD MHT algorithm even for low magnitude luminosity targets.

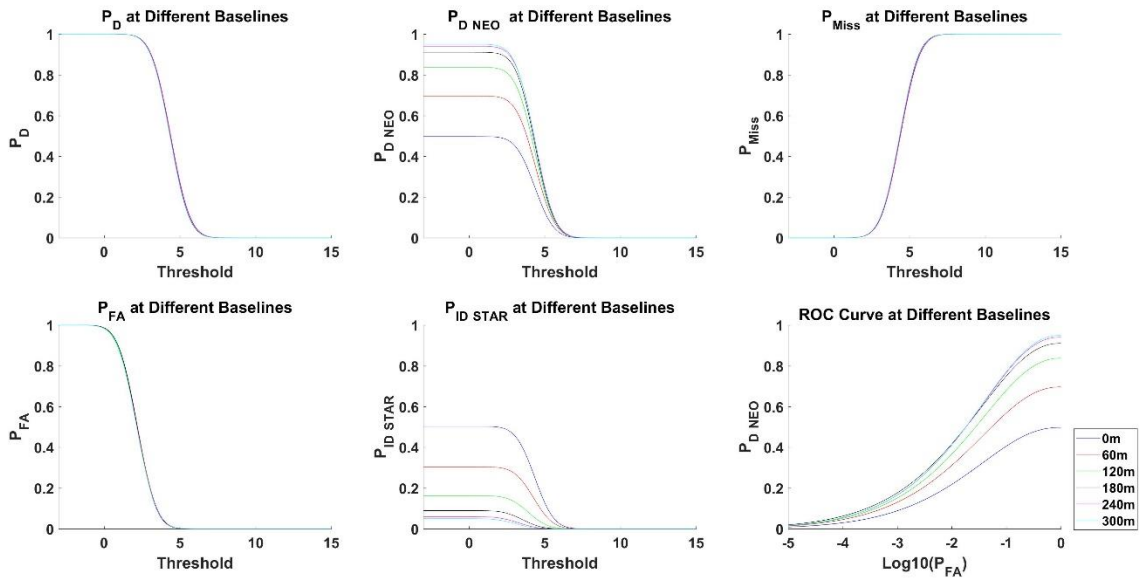

Figure 29: Algorithm Performance with Satellite Present in Data Frame and SNR of 1

In Figure 30, the average background pixel magnitude is twice that of the target. $P_{D\ NEO}$ has decreased to 80% and $P_{ID\ STAR}$ has increased to 20% for the largest baseline. The performance curves for the different baseline optical systems are being bounded by a smaller range of likelihoods as the chance of selecting the wrong hypothesis becomes more likely. For every optical system, there is some limiting factor to how well the algorithm can pull the shape of the non-paraxial PSF out of the background noise and differentiate that shape from other hypothesized targets. By SNRs of 1/3, as seen in Figure 31, $P_{D\ NEO}$ maxes out at 70% and the successive baseline's performance curves are squeezed even closer together as $P_{ID\ STAR}$ increases. At every threshold value, $P_{ID\ STAR}$ and $P_{D\ NEO}$ sums to P_D which ranges between 0 and unity. Figure 32 demonstrates that at pixel SNR values of 1/6, $P_{D\ NEO}$ of all baseline configurations are squeezed even closer together with a baseline separation of 300 meters only providing a 10% increase over a 0 meter baseline separation where the reference and parallax PSF's look identical.

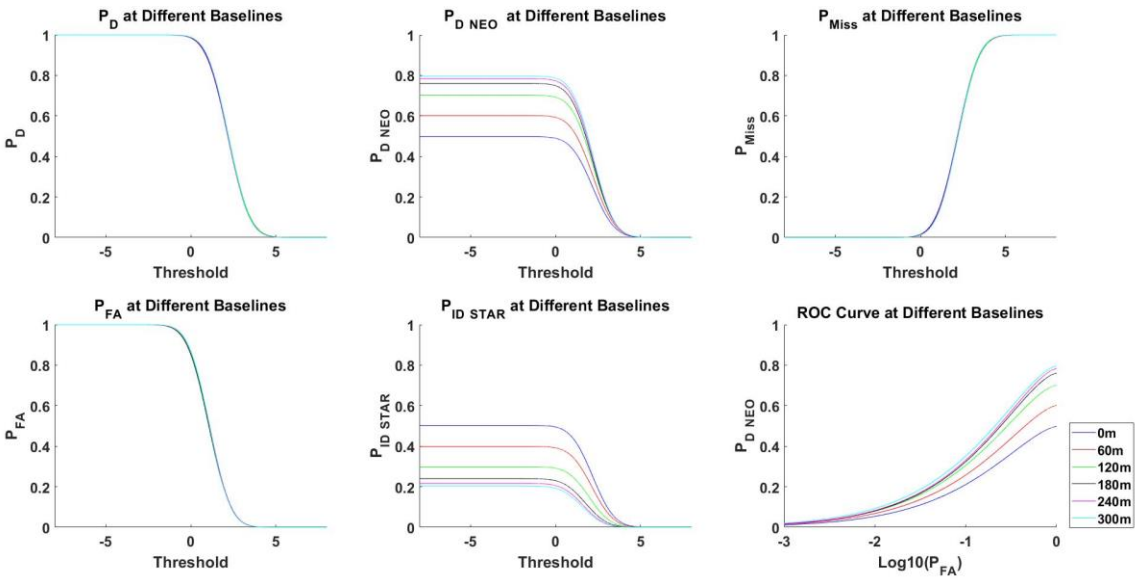

Figure 30: Algorithm Performance with Satellite Present in Data Frame and SNR of 1/2

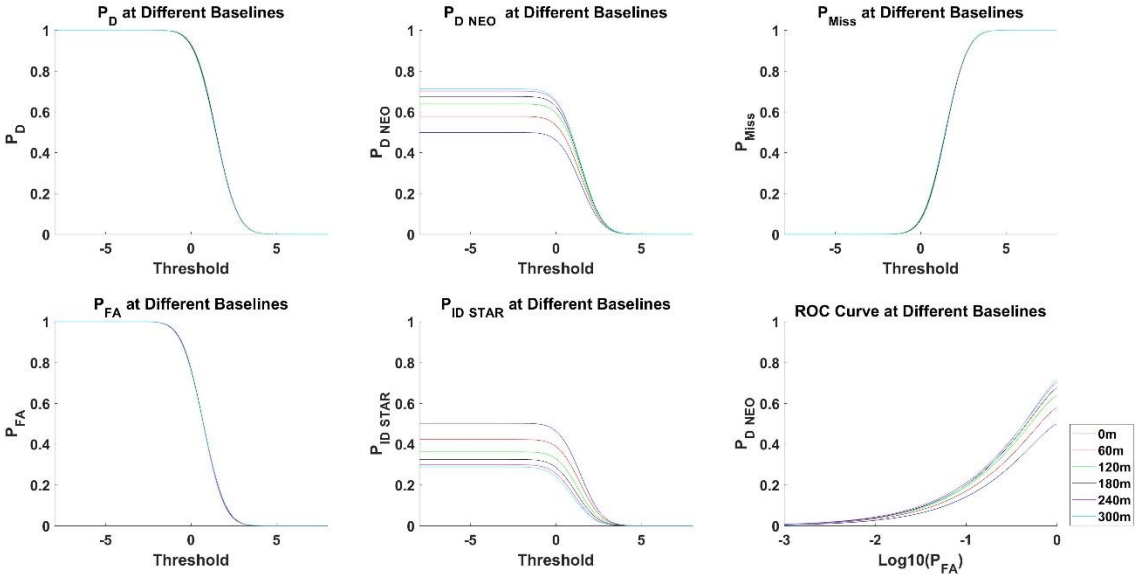

Figure 31: Algorithm Performance with Satellite Present in Data Frame and SNR of 1/3

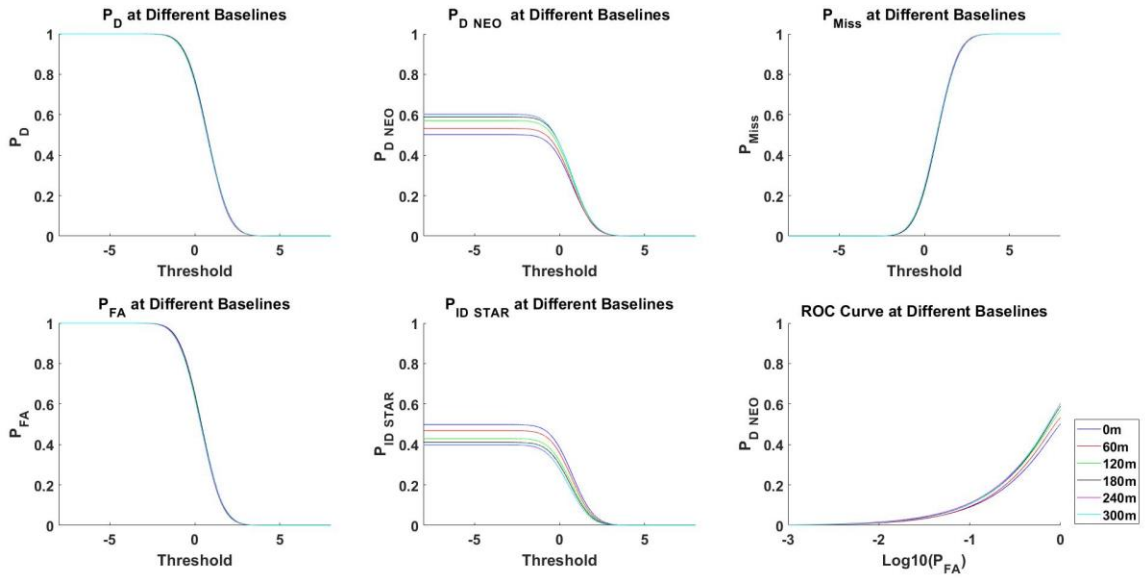

Figure 32: Algorithm Performance with Satellite Present in Data Frame and SNR of 1/6

For lower SNR values, the logarithmic ROC curve is less meaningful because $P_{D\ NEO}$ does not level out at low P_{FA} values; Figure 33 shows the ROC curves where PFA is varied linearly. Another useful observation is that as the target luminosity decreases, a larger baseline separation buys less performance.

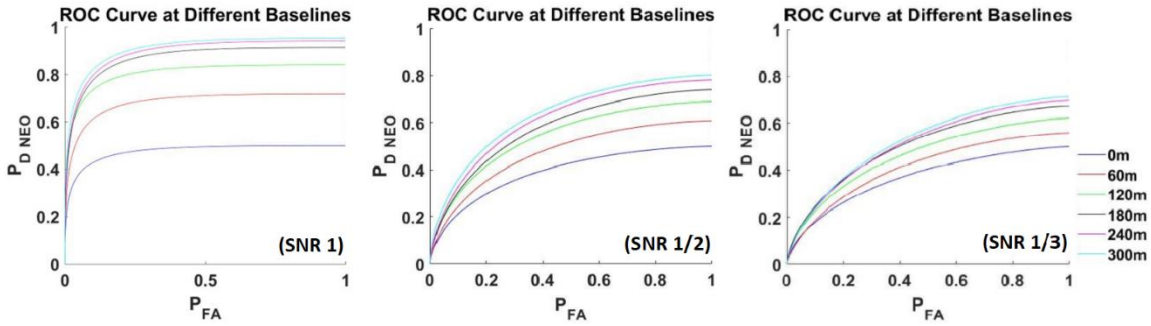

Figure 33: Linear ROC Curves at Different Baselines for SNR's of 1, 1/2 and 1/3

In this simulation, the range of baselines was chosen so that each baseline increase corresponded to a 1 Nyquist pixel shift of the non-paraxial PSF center location. From the off-axis PSF section, the brightest part of the PSF has a radius of five to six Nyquist pixels and even at the largest simulated baseline of 300 meters, the non-paraxial PSF given a GEO target is overlapping with where the non-paraxial PSF given a stellar target would be. The power of the CD MHT algorithm is that it can extract the spatial distribution of a PSF from noisy data by correlating the data in a test frame with pre-determined hypotheses. The algorithm is effective at distinguishing between stellar and NEO targets even in noise dominated data frames with relatively small non-paraxial PSF shifts.

V. Experiment

In this chapter, a dataset of synchronous observations of two targets by the SST and Naval Observatory telescopes as the targets are eclipsed by the earth are used as inputs to the CD MHT algorithm from Chapter 3. Geometric optics is used to properly register the PSF's required by the CD MHT algorithm given the separation between the two telescopes. Following registration, the synchronous data frames are then run through the CD MHT algorithm to produce LRT realizations for each data frame under the H_1 hypothesis. The LRT outputs are normalized by the standard deviation of the data, due to noise, to produce values in terms of SNR. These SNR values are used to determine the statistical probability of detection and correct categorization of the target as a NEO, $P_{D\ NEO}$, using the performance metrics also derived in Chapter 3. The PD algorithm used by SSN ground based optical sensors today is also used to compute LRT realizations for every data frame. These LRT values are also normalized by the standard deviation of the of the data to determine the statistical probability of detection using heritage algorithms, P_D. These performance of the heritage PD and new CD MHT algorithms are compared to demonstrate the utility of the new detection algorithm.

Experimental Setup and System PSF Registration

The purpose of the experiment is to test the new CD MHT detection algorithm to see if it correctly determines that an observation is a NEO based on the presence of parallax as hypothesized in the H_1 case. The data collection took place simultaneously from the SST and Naval Observatory with both the ANIK-F1 and ANIK-F1R satellites in view as the two satellites are eclipsed by the earth. As the two satellites fall into the shadow of the

earth, their luminosity decreases until the satellites are dimmer than the background noise. The experimental setup is different than the ideal setup proposed in the non-paraxial PSF section of Chapter 2 because both telescopes were configured to track ANIK F1 using their gimbal systems. The parallax effects due to tilt are present in the aperture of the parallax sensing telescope when the telescope's optical axis is not set to be aligned with the target. If the reference telescope is set to track the target while the parallax sensing telescope is set to maintain its optical axis parallel to that of the reference telescope's, the parallax effect in the parallax sensing telescope is maximized. Because astronomical telescope systems in use today aren't configured to track in such a manner, it was necessary to make due by observing two targets by two telescopes simultaneously. Henceforward, ANIK F1 will be referred to as the primary target and ANIK F1R will be referred to as the secondary target. Figure 34 demonstrates an exaggerated drawing of the system being tested. In the figure, the primary target's phase-front is centered on both telescopes because they are aligned to track it causing the PSFs to be centered at the focal point on the CCD. The phase-front from the secondary target is not centered on the either aperture because neither telescope is set to track it which causes the PSF to be non-paraxial or not at the focus of the mirrors on either CCD array. Parallax is observable in the frames of SST and Naval Observatory telescope data because the PSF from the secondary target is in a different position relative to that of the primary target on each respective CCD. The pixel size of the CCD used in the Naval Observatory optical setup is not known so a first principles approach is used to determine the angular size of the pixels in the observed frames of data. The primary and secondary targets are both Geostationary NEOs and their position in the data does not change during the experiment.

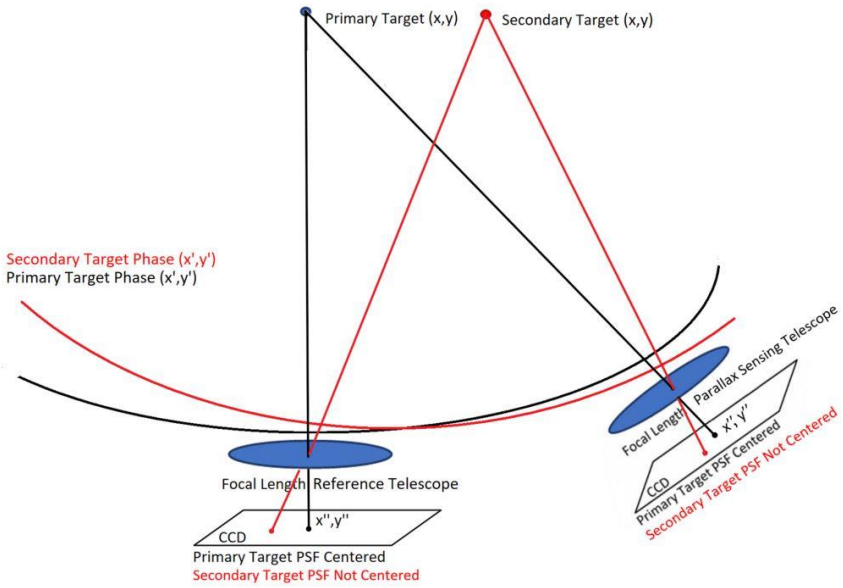

Figure 34: Two Telescopes Tracking Primary Target and Secondary Target in FOV

As the earth rotates, stars appear in the data frames of both telescopes; because the rotation speed of the earth is fixed, the apparent movement of the PSF's due to stars in the data is also fixed and the time between successive data frames is known for each telescope. The apparent movement velocity of a star relative to an observation point on earth in degrees per unit time is 360 degrees in 23 hours 56 minutes and 4.1 seconds. Converted to degrees per seconds, the movement velocity is 360 degrees per $8.6264 \text{x} 10^4$ seconds as seen in Equation (3.88). For the SST telescope, there is a new data frame every 1 second so each successive frame of data is $4.2 \text{x} 10^{-3}$ degrees forward of the prior frame.

$$\frac{360\,\text{deg}}{8.6164x10^4\,\text{sec}}\,x\,\frac{1\text{sec}}{1\text{ frame}} = \frac{4.2x10^{-3}\,\text{deg}}{1\text{ frame}} \tag{3.88}$$

A star's PSF in the SST data was observed to move 9 pixels between successive frames. The angular size of the pixels in the SST's CCD as computed by taking the known angular change between successive frames and dividing that by the number of pixels of motion

between successive frames resulting in a quantity in units of degrees per pixel. As seen in Equation (3.89) the SST's CCD pixels were found to have an angular size of 4.6423×10^{-4} degrees per pixel.

$$\frac{4.2x10^{-3}\,\text{deg}}{1\,\text{frame}}\,x\,\frac{1\,\text{frame}}{9\,\text{pixels}} = 4.6423x10^{-4}\,\frac{\text{deg}}{\text{pixel}} \tag{3.89}$$

The same process was repeated with the data frames collected from Naval Observatory with the only difference being that the Naval Observatory has a longer integration time causing the stars to streak through the data rather than showing up as a PSF. Successive Naval Observatory data frames are 7 seconds apart. As seen in Equation (3.90), the angular separation between successive frames is 31.3×10^{-3} degrees per frame.

$$\frac{360\,\text{deg}}{8.6164x10^{4}\,\text{sec}}\,x\,\frac{7\,\text{sec}}{1\,\text{frame}} = \frac{31.3x10^{-3}\,\text{deg}}{1\,\text{frame}} \tag{3.90}$$

The length of the streak stays constant between successive data frames but it's initial and final pixel coordinates are different and the number of pixels of motion between frames is computed by differencing either the initial or final coordinates of the steak in successive frames. The number of pixels of motion between successive frames was found to be 186 pixels and the angular size of each pixel was found to be 1.6847×10^{-4} degrees per pixel as seen in Equation (3.91).

$$\frac{31.3x10^{-3}\,\text{deg}}{1\,\text{frame}}\,x\,\frac{1\,\text{frame}}{186\,\text{pixels}} = 1.6847x10^{-4}\,\frac{\text{deg}}{\text{pixel}} \tag{3.91}$$

The motion of the stars also allowed for the proper orientation of the data frames because stars move in a Westward motion on the East-West axis. If the CCD's horizontal axes were North-South and vertical axis were East-West, the star motion would be on the vertical axis. The amount of parallax in the aperture of the reference and parallax sensing telescopes

depends on the latitude, longitude and altitude of the secondary target as compared to that of the primary target which is aligned with both telescope's optical axes as viewed from both telescope sites. Table 6 shows the coordinates of the primary target, secondary target, reference telescope site and parallax sensing telescope site.

Table 6: Locations of Both Targets and Both Telescopes

	Latitude (deg)	Longitude (deg)	Altitude (Km)
ANIK F1	-0.03	-107.29	35,778.76
ANIK F1-R	0.01	-107.30	35,784.53
SST	32.943896	-106.41966	6,384
Naval Observatory	35.184447	-111.73982	6,384

As the crow flies, the Naval Observatory is 550.32 Km from the SST which can be broken down into 232.5753 Km in the East-West axis and 498.7593 Km in the North-South axis. The distance between the two satellites was found to be 30.27 Km by calculating the tangential distance between the coordinates on a sphere with a radius of approximately 36,000 Km. The distance between the two telescopes is an order of magnitude more than the distance between the two satellites and the parallax effect will be proportional to the East-West and North-South distance difference between the two observation sites. Because star motion appears to be westward and the star motion in the CCD is in vertical the direction, it is expected that the difference in secondary target PSF location between the two telescopes in the vertical direction of the CCD will be approximately twice that of the horizontal direction. The actual secondary target PSF shift due to parallax in degrees is found for each telescope system by determining the position in pixels for both telescopes, converting those positions to degrees and then finding the difference between the two. Figure 35 shows a non-saturated data frame from the SST telescope and Figure 36 shows a non-saturated data frame from the Naval Observatory telescope. The PSFs from the two

telescopes look different because of differences in the optical setup of the respective telescopes to include aperture diameter, focal length, CCD pixel size and integration time.

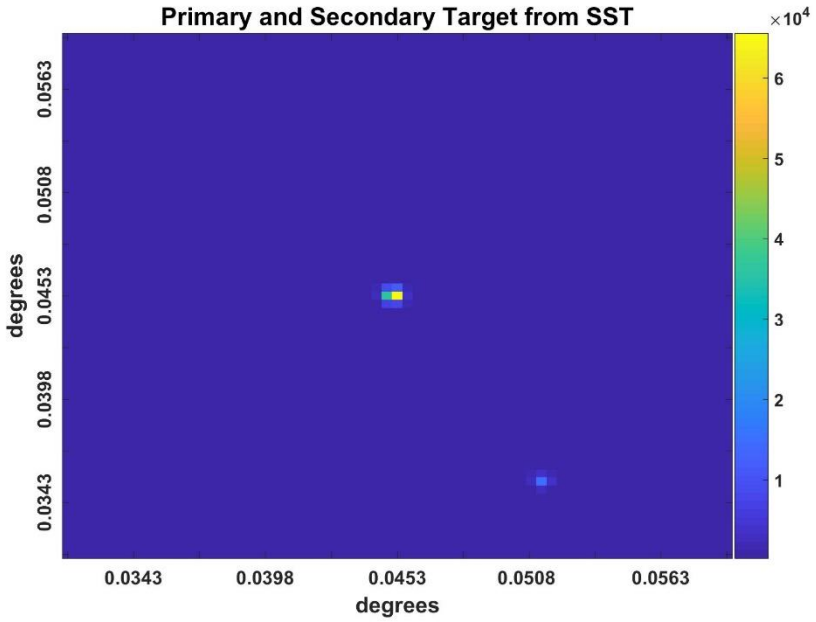

Figure 35: Observation from SST Telescope of ANIK-F1 and ANIK-F1R

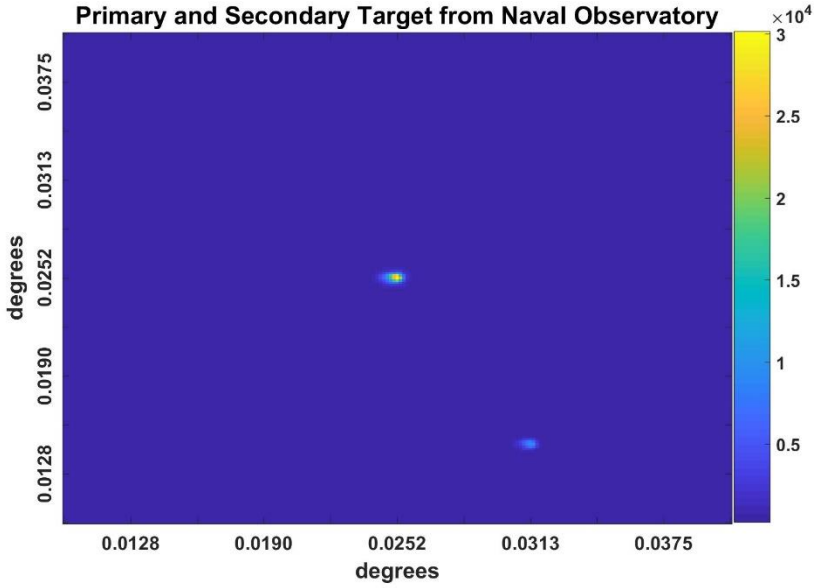

Figure 36: Observation from Naval Observatory Telescope of ANIK-F1 and ANIK-F1R

In both data frames, ANIK-F1 is the primary target and ANIK-F1R is the secondary target; ANIK-F1 is brighter than ANIK-F1R. It's hard to tell that the secondary target's PSF is in a different location from the data frames. Table 7 shows the location of the secondary target's PSF in pixels and degrees as seen on the CCD for both telescopes as compared to the location of the primary target's PSF on the CCD. It also shows the difference between the secondary target's relative position in the CCD as seen by the SST location as compared to the position of the secondary target's position in the CCD as seen by the Naval Observatory location. The difference in where the secondary target's PSF shows up is because of parallax and as expected, the amount of PSF shift in the vertical axis is over twice that as seen in the horizontal axis. This is due to the observation locations being roughly twice as far in the East-West direction as compared to the North-South direction.

Table 7: Registration of Parallax Effect due to Different Observation Locations

Telescope Location	y-axis PSF Separation (pixels)	y-axis PSF Separation (deg)	x-axis PSF Separation (pixels)	x-axis PSF Separation (deg)
SST	23	0.0107	14	0.00650
Naval Observatory	68	0.0115	40	0.00670
Difference (SST)	1.68	7.7867×10^{-4}	0.516	2.3958×10^{-4}
Difference (Navy)	4.622	7.7867×10^{-4}	1.422	2.3958×10^{-4}

The difference in Table 7 is shown in units of SST CCD pixels and in units of Naval Observatory CCD pixels; it is how many pixels the secondary target's PSF needs to be shifted to put it where it would be in the other telescope's CCD relative primary target's PSF. The Naval Observatory has smaller pixels and it would more accurately quantify the PSF shift due to parallax; however, the SST has a faster integration time and thus, more data frames to run the CD MHT algorithm against. As seen in the simulation section, single pixel shifts are adequate to distinguish a NEO target from a stellar target so, the quantity

of data frames makes the SST telescope the best choice for the Parallax sensing telescope in the experiment due to the dimming target luminosity throughout during the data collect.

Correlator Detector Multi-Hypothesis Test with System of Different Telescopes

The Naval Observatory Telescope is set to be the reference telescope and the SST is set to be the parallax sensing telescope. For each hypothesis, there is a unique set of test PSFs against which the collected data is correlated with. The LRT as seen in Equation (3.60) was chosen to implement the CD MHT algorithm because the satellites being observed become dimmer during the data collect. Using the ratio of luminosities when the signal is high is a good way to determine the ratio without the effects of noise; otherwise, Equation (3.65) would be a good selection. To compute the ratio of the image intensity as seen in the parallax sensing telescope to that as seen in the reference telescope, the total photo-counts in each aperture were summed and then divided after removing the background photon contribution. The data read in by the reference telescope is correlated with the reference telescope's expected PSF and the data read in by the parallax sensing telescope is correlated with PSF's corresponding to the NEO and stellar object hypotheses which are H_1 and H_2 respectively. The PSFs used in the algorithm are created from the collected data by selecting un-saturated data frames which better represent the spatial distribution of expected observations. The background of the frame of data is computed using a median filter [11] and then subtracted from all pixels in that frame of data. Any negative pixels are set to zero and the test PSF is created by normalizing this fame of data using Equation (2.13). The h_{ref}, h_{neo} and h_{star} test PSFs required to test for H_1 and H_2 using Equation (3.60) are created using this technique. The reference telescope's test PSF, h_{ref}, does not depend

on the presence of parallax, it seen in Figure 38. Proper registration of the remaining test PSFs is determined by the orientation of the observation location of the reference and parallax sensing telescopes as defined in Table 6 and Table 7.

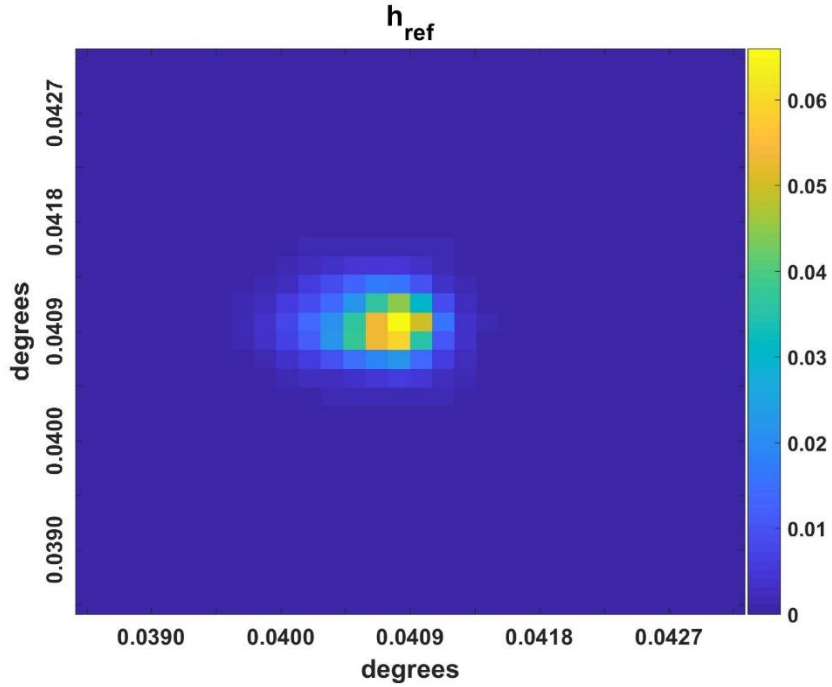

Figure 37: Test PSF for Reference Telescope

Throughout the experiment, the location of the geostationary NEO target, ANIK-F1R, does not change, but due to parallax, the location of ANIK-F1R as observed on the CCD of the reference and parallax sensing telescopes is different. The parallax sensing telescope's observations of ANIK-F1R are registered to be centered in the SST telescopes CCD and stellar observations are shifted to where they would be located as viewed by the reference telescope. Alternatively, the location of a stellar observation, which has un-detectable parallax present in the parallax sensing telescope's aperture, could be registered at the CCD's center to achieve the same result by shifting the ANIK-F1R observations to where

they would be as viewed by the parallax sensing telescope's CCD. The remaining test PSFs, h_{neo} and h_{star}, are shown in Figures 38 and 39 respectively. The PSFs look very different from h_{ref} because the reference and parallax sensing optical configurations differ.

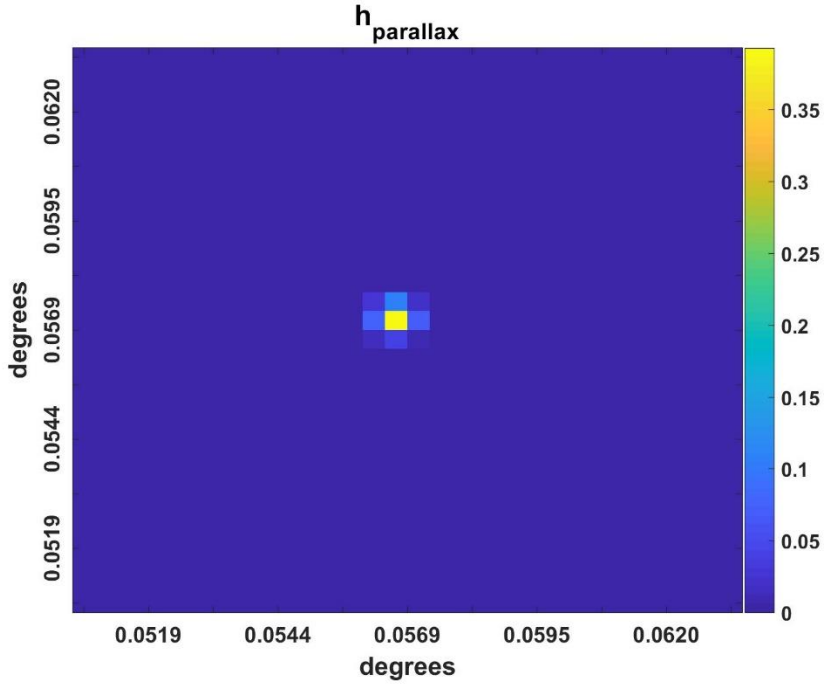

Figure 38: Test PSF for Parallax Sensing Telescope Hypothesizing H_1 is true

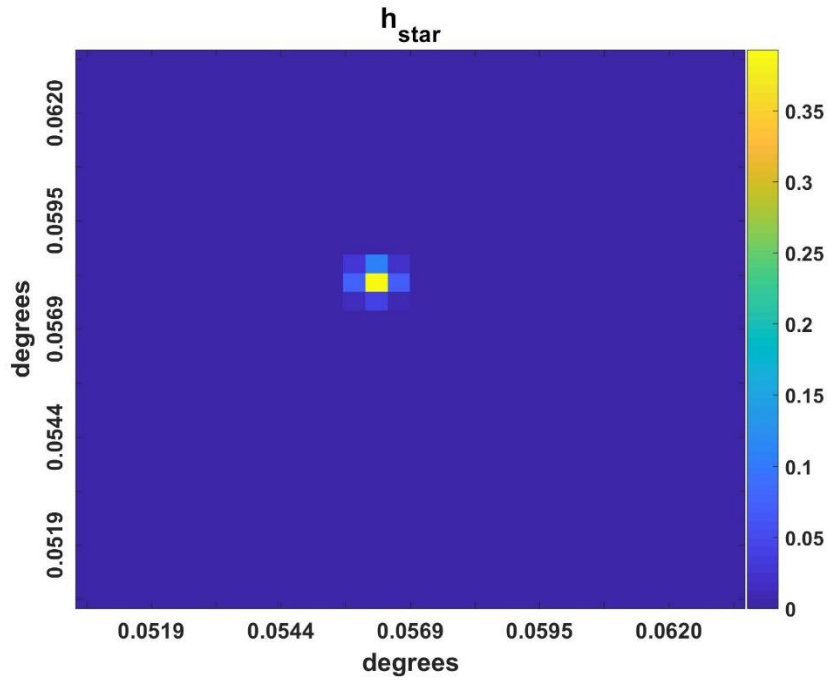

Figure 39: Test PSF for Parallax Sensing Telescope Hypothesizing H_2 is true

SST data frames are generated at a rate of 1 per second and Naval Observatory data frames are generated at a rate of 1 per 7 seconds because the integration times differ between the two telescopes. The CD MHT algorithm takes in raw data from simultaneous observations of the target collected by the two telescopes; to achieve this, every frame of the SST data is fed into the test and new frame of Naval Observatory data is updated once the seventh SST data frame has been registered. Data frames were chosen to be 30 by 30 windows around the observed target. Equation (3.60) is easily implemented with the test PSFs by correlating the data read in by the Naval Observatory telescope's CCD with its test PSF, h_{ref}, and correlating the data read in by the SST's CCD with the test PSF corresponding to either the H_1 or H_2 hypothesis, h_{neo} or h_{star}. The second correlation is multiplied by the ratio of target intensities and then the two correlations are added together. In this manor, the two

LRT's, $\Lambda_1(frame)$ and $\Lambda_2(frame)$, are computed by using Equation (3.60) to produce the two random variables. The LRT given H_1 is hypothesized is divided by the local standard deviation making it a unit-normal Gaussian random variable and the effects of noise on this SNR are reduced using a moving average over 10 frames [11]. The Point Detector (PD) algorithm, as defined by Zingarelli [11], was also used to determine what the SNR would be for SSN sensors used by the USAF given the same data. Both the SNR from the CD MHT LRT and the PD algorithm are plotted in Figure 40; this value is the number of standard deviations the signal is over the background. From the figure, it is clear the CD MHT algorithm produces a higher SNR at lower target luminosities as compared to the PD algorithm. Figure 40 also shows that stars passing through the data, as seen in frames 424 and 735, have a lower SNR value when using the CD MHT algorithm as compared to the when using the traditional PD detection algorithm.

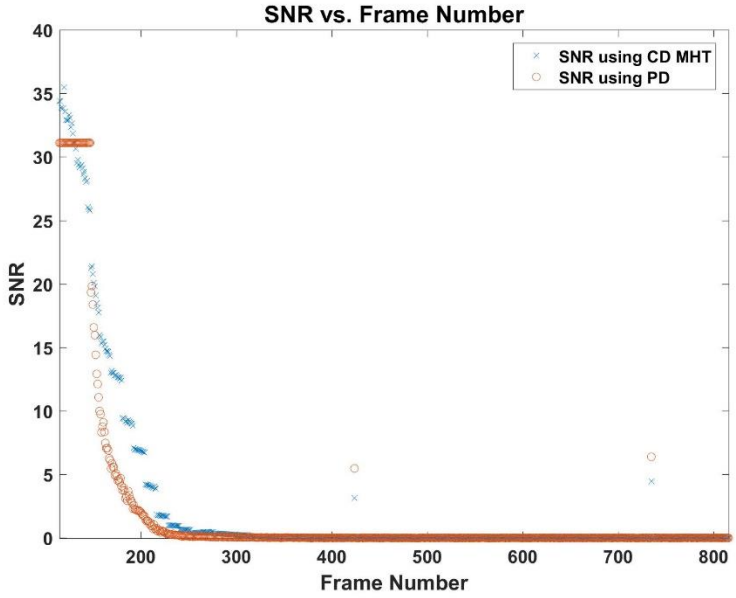

Figure 40: SNR using CD MHT and SNR using PD vs. SST Frame Number

The CD MHT algorithm performs better than the PD algorithm due to the correlator's ability to compare an observed target's PSF spatial distribution to the shape that is hypothesized. Another gain of the CD MHT algorithm is that it is also able to distinguish whether a detection is a NEO or a stellar object by using multiple hypotheses. In this case, there are two hypotheses being tested by the CD MHT; the hypothesis that a NEO is present in the observed data, H1, and the hypothesis that a star is present in the observed data, H2. When run though the CD MHT, a LRT is produced for each of the two hypotheses. The two LRT's, $\Lambda_1(frame)$ and $\Lambda_2(frame)$, are differenced as seen in Equation (3.70) producing the new random variable, Z_1, which is then normalized and averaged the same way that the LRT was producing a unit-normal Gaussian random variable. The SNR of the Gaussian random variable, Z_1, is seen in Figure 41. The figure shows that the CD MHT algorithm, as seen in Equation (3.60), correctly categorized the detections as a NEO.

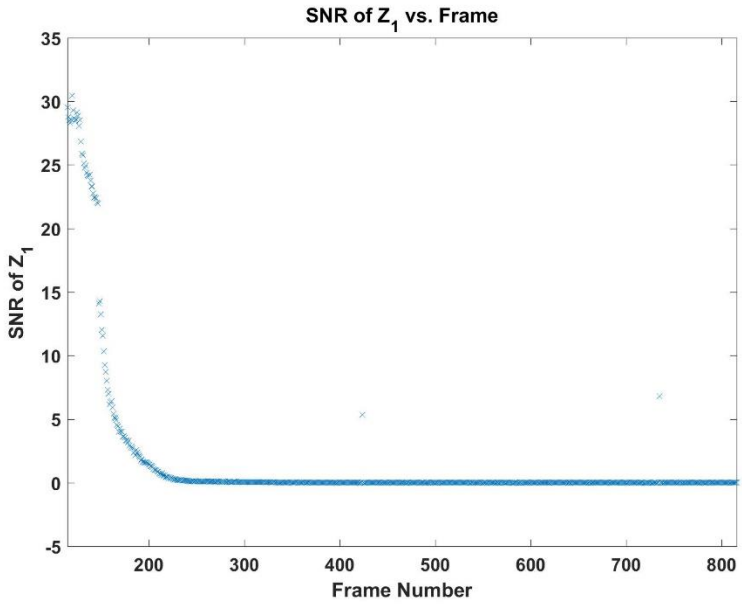

Figure 41: SNR of Z1 vs. SST Frame Number

Using the SNR to generate a probability curve is much more powerful than just using the SNR values to show that correct detections have been made because it represents the likelihood of making the correct choice given a desired P_{FA}. The SNR values are used to find the probability of correctly detecting a NEO, $P_{D\,NEO}$, when it is present in the observed data. $P(Z_1 > 0)$ is computed by using the CDF MATLAB command with a threshold of zero with inputs of the SNR value of each frame found using the Gaussian random variable Z_1 which is seen in Figure 41. P_D is computed by using the CDF MATLAB command with a threshold of six standard deviations given inputs of the SNR value at each frame using the Gaussian random variable $\Lambda_1(\mathit{frame})$ as outputted by the CD MHT algorithm which is seen in Figure 42. $P_{D\,NEO}$ is found for each SST frame by multiplying $P(Z_1 > 0)$ by P_D as seen in Equation (3.76). A threshold for detection of 6 standard deviations was selected to produce a P_{FA} of 10^{-9} which is desired by USAF SSN applications. The probability of detecting a target, P_D, using the standard PD algorithm was also computed using the CDF MATLAB command with a threshold of six standard deviation with inputs of the SNR value at each frame found using the Gaussian random variable computed using the PD algorithm. Figure 42 is the plot of $P_{D\,NEO}$ found using the CD MHT algorithm and P_D found using the PD algorithm for this selected $P_{FA.}$ In the figure, the CD MHT algorithm has a superior performance as compared to the PD algorithm used by USAF SSN sensors currently with the additional bonus that the CD MHT algorithm also determines the type of observation being detected. The probability of detecting a star when a NEO is hypothesized using the CD MHT algorithm is also much smaller than the probability of detecting a star in the data using the PD algorithm.

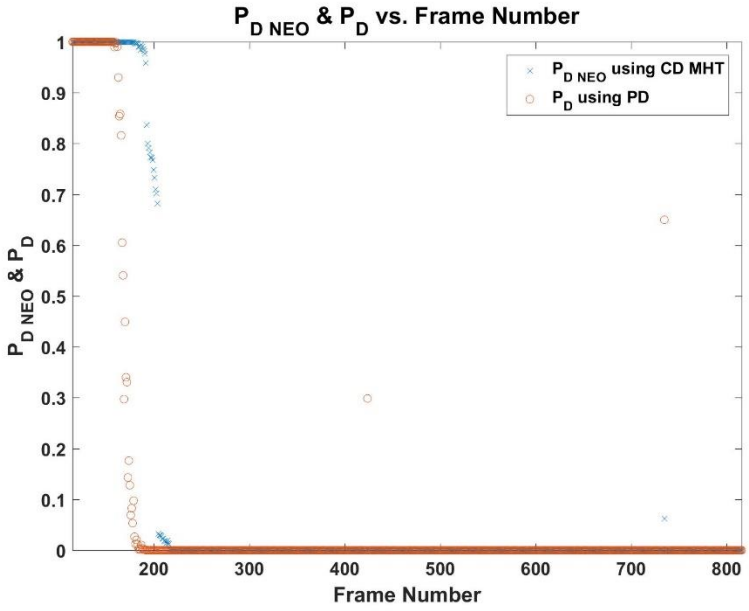

Figure 42: $P_{D\ NEO}$ using CD MHT and P_D using PD vs. SST Frame Number

The data from the SST is used directly to test the ability of the CD MHT algorithm to detect a NEO; however, observations of stellar objects were not obtained because the telescopes were set to track the geostationary ANIK-F1 NEO and any observed stars streak through the data frames and the CD MHT algorithm was not designed to test against streaks. These results demonstrate that heritage USAF SSN resources can implement this new detection process to determine if an observation is a NEO in a single frame of data. The SPOT facility at Lockheed Martin, Santa Cruz would be the ideal arrangement to test the performance of this algorithm because that facility has telescopes on railroad tracks allowing for an adjustable baseline, the telescopes are identical which would allow for the CD MHT algorithm to be independent of signal luminosity, and there are different CCD and telescope configurations which would allow the experiment to be optimized by maximizing PSF shift caused by parallax.

VI. Conclusions and Recommendations

Conclusions

The simulation and experiment showed that a system of either identical or different telescopes collecting simultaneous frames of data and separated by some physical baseline are effective at detecting parallax and the nature of a detected target can be categorized as either a stellar or NEO observation in a single frame of data. The simulation showed that increasing the baseline difference between the reference and parallax sensing telescopes increases the performance of the CD MHT algorithm when the luminosity of the target is closer to that of the background. When the target is much brighter than the background, as seen in the SNR 6 simulation, all system baselines correctly detect and categorize the target with assuredness. At a SNR 2, the algorithm has a probability of correctly detecting and categorizing the target as a NEO, $P_{D\,NEO}$, of 85% to 95%, depending on baseline, by setting the false alarm probability, P_{FA}, to 10^{-9}. For low luminosity targets, the utility of a larger baseline is somewhat diminished. The simulation also shows the usefulness of more accurate field propagation techniques dispelling the anecdote that the additional aberrations neglected by the Fresnel approximation aren't useful. The propagation technique evaluated in this thesis was demonstrated to more accurately model optical systems allowing for novel improvements in SSA sensors; even in the absence of a geometric PSF shift, the algorithm can distinguish unique PSF shapes. The experiment showed that real USAF SSN assets can be utilized in their present state to detect the parallax effect in observations and correctly identify a target in single data frames. Moreover, the probability of detecting a NEO target and correctly categorizing that detection, $P_{D\,NEO}$, is higher than the probability

of target detection, P_D, using heritage techniques. This is a big improvement over heritage PD algorithms which also require target detection in 3-5 successive frames to register a detection. The CD MHT algorithm could also be used to determine the altitude of a given observation by using more hypothesized PSF's or the speed of an observation by using successive frames and effects of horizontal or vertical tilt. With the altitude, speed, right ascension and declination, all orbital parameters of the satellite can be computed. Overall, these results show that implementation of the CD MHT algorithm proposed by the AF would be in line with AF leadership goals to network existing architecture for increased performance. This body of work shows that the USAF SSN ground based optical sensors can share data in a way which improves performance without adding to cost.

Recommendations

A major limitation of the experiment is that it was done on a non-ideal optical setup; data from a more ideal optical system such as Lockheed Martin's SPOT facility would allow for the optimization and complete statistical characterization of the algorithm with real data. Provided the resources, the USAF could develop a system of rapidly deployable, low cost ground based optical sensors with an Ad-Hoc communication scheme for networking and data-sharing. The system could be deployed to any region based on need and provide live data to the JSpOC JMS based on the operational needs of the USAF. Already operating USAF SSN sensors could be better leveraged by sharing their data to utilize more perceptive detection schemes such as the CD MHT algorithm. Future students or research organizations could further this body of work by extending the use of the CD MHT algorithm to characterize the altitude and speed of space observations or by developing systems of interconnected telescopes to produce fused data sets.

VII. Bibliography

[1] Joseph A. Haimerl; Gregory P. Fonder, “Space Fence System Overview.” Lockheed Martin, Tokyo, Japan.

[2] “RDT&E Budget Item Justification: PB 2017 Air Force,” 2016. [Online]. Available: http://www.dtic.mil/descriptivesum/Y2017/AirForce/stamped/U_0604425F_5_PB_2017.pdf. [Accessed: 14-Aug-2017].

[3] ADM C. D. Haney, “Center for a New American Security,” 2016. [Online]. Available: http://www.stratcom.mil/Media/Speeches/?Search=Center+for+a+New+American+Security. [Accessed: 21-Aug-2017].

[4] M. Gruss, “U.S. Plans $6 Billion Investment in Space Situational Awareness,” 2015. [Online]. Available: http://spacenews.com/planned-u-s-investment-in-space-awareness-is-6-billion-gao-says/. [Accessed: 02-Mar-2017].

[5] “Geosynchronous Space Situational Awareness Program (GSSAP),” 2016. [Online]. Available: http://www.dote.osd.mil/pub/reports/FY2016/pdf/af/2016gssap.pdf. [Accessed: 21-Aug-2017].

[6] M. Gruss, “U.S. Air Force Space Tracking Software Delayed 19 Months,” *Space News*, 2016. [Online]. Available: http://spacenews.com/u-s-air-force-space-tracking-software-delayed-19-months/. [Accessed: 02-Mar-2017].

[7] GEN J. E. Hyten, “General John Hyten - 2015 Space Symposium,” 2015. [Online]. Available: http://www.afspc.af.mil/About-Us/Leadership-Speeches/Speeches/Display/Article/731707/general-john-hyten-2015-space-symposium/. [Accessed: 15-Aug-2017].

[8] GEN D. Goldfein, “Air Force Update,” in *Air, Space & Cyber Conference*, 2017.

[9] H. E. M. Viggh, G. H. Stokes, F. C. Shelly, M. S. Blythe, and J. S. Stuart, “Applying Electro-Optical Space Surveillance Technology to Asteroid Search and Detection: The Linear Program Results,” in *Space Control Conference*, 1998.

[10] J. Chris Zingarelli, E. Pearce, R. Lambour, T. Blake, C. J. R. Peterson, and S. Cain, “Improving the Space Surveillance Telescope’S Performance Using Multi-Hypothesis Testing,” *Astronomy Journal*, vol. 147, no. 5, p. 111, 2014.

[11] J. C. Zingarelli, “Enhancing Ground Based Telescope Performance With Image Processing,” Air Force Institute of Technology (AU), 2013.

[12] J. W. Goodman, “Introduction to Fourier Optics, Third Edition,” *Optical Engineering*. p. 491, 2004.

[13] Stephen C. Cain and T. Watts, “Nonparaxial Fourier Propagation Tool for Aberration Analysis and Point Spread Function Calculation,” *Opt. Eng.*, vol. 55, no. 8, 2016.

[14] T. Watts, “Field-Based Phase Retrieval Using Under-Sampled Data,” MS thesis, Graduate School of Engineering and Management, Air Force Institute of Technology (AU), 2015.

[15] “Astronomical seeing.” [Online]. Wikipedia.Org. Wikimedia Foundation, Inc. Available: https://en.wikipedia.org/wiki/Astronomical_seeing. [Accessed: 03-Mar-2017].

[16] N. A. Roddier, “Atmospheric wavefront simulation using Zernike polynomials,” *Opt. Eng.*, vol. 29, no. 10, p. 1174, 1990.

[17] J W Goodman, *Statistical optics*, vol. 22. 1986.

[18] I. H. Hahn, “Tilt (optics),” 2010. [Online]. Wikipedia.Org. Wikimedia Foundation, Inc. Available: https://en.wikipedia.org/wiki/Tilt_(optics). [Accessed: 20-Nov-2017].

[19] R. D. Richmond and S. C. Cain, *Direct-Detection LADAR Systes*. Bellingham: SPIE Press, 2010.

REPORT DOCUMENTATION PAGE

Form Approved
OMB No. 0704-0188

1. REPORT DATE *(DD-MM-YYYY)*	**2. REPORT TYPE**	**3. DATES COVERED** *(From - To)*
22-03-2018	Master's Thesis	Aug 2016 – Mar 2018

4. TITLE AND SUBTITLE
Near Earth Space Object Detection Utilizing Parallax as Multi-Hypothesis Test Criterion

5a. CONTRACT NUMBER

5b. GRANT NUMBER

5c. PROGRAM ELEMENT NUMBER

6. AUTHOR(S)
Tompkins, Joseph C, Capt

5d. PROJECT NUMBER

5e. TASK NUMBER

5f. WORK UNIT NUMBER

7. PERFORMING ORGANIZATION NAME(S) AND ADDRESS(ES)

Air Force Institute of Technology
Graduate School of Engineering and Management (AFIT/EN)
2950 Hobson Way, Building 640
WPAFB OH 45433-8865

8. PERFORMING ORGANIZATION REPORT NUMBER

AFIT-ENG-MS-18-M-064

9. SPONSORING / MONITORING AGENCY NAME(S) AND ADDRESS(ES)

Intentionally Left Blank

10. SPONSOR/MONITOR'S ACRONYM(S)

11. SPONSOR/MONITOR'S REPORT NUMBER(S)

12. DISTRIBUTION / AVAILABILITY STATEMENT

DISTRIBUTION STATEMENT A: APPROVED FOR PUBLIC RELEASE; DISTRIBUTION UNLIMITED.

13. SUPPLEMENTARY NOTES
This material is declared a work of the U.S. Government and is not subject to copyright protection in the United States.

14. ABSTRACT

This thesis explores a reliable, ground-based technique to quickly determine the altitude of a RSO from a single or limited set of observations; implementation of such sensors into the SSN would mitigate GEO SSA performance gaps. The research entails a method to distinguish between the point spread function (PSF) observed by a star and the PSF observed from an RSO using Multi-Hypothesis Testing with parallax as a test criterion. Parallax is the effect that an observed object will appear to shift when viewed from different positions. This effect is explored by generating PSFs from telescope observations of space objects at different baselines. The research has shown the PSF of an RSO can be distinguished from that of a star using single, simultaneous observations from reference and parallax sensing telescopes. This thesis validates these techniques with both simulations and with experimental data from the SST and Naval Observatory sensors.

15. SUBJECT TERMS
Correlator Detector (CD), Multi-Hypothesis Test (MHT), Parallax, Near Earth Object (NEO) Detection, Space Situational Awareness (SSA)

16. SECURITY CLASSIFICATION OF:			**17. LIMITATION OF ABSTRACT**	**18. NUMBER OF PAGES**	**19a. NAME OF RESPONSIBLE PERSON**
a. REPORT	**b. ABSTRACT**	**c. THIS PAGE**			Dr. Stephen C. Cain, AFIT/ENG
U	U	U	UU	131	**19b. TELEPHONE NUMBER** *(include area code)* 937-255-3636x4716